



HAL
open science

Diffusion processes in biological membranes studied by molecular dynamics simulations and analytical models

Slawomir Stachura

► **To cite this version:**

Slawomir Stachura. Diffusion processes in biological membranes studied by molecular dynamics simulations and analytical models. Chemical Physics [physics.chem-ph]. Université Pierre et Marie Curie - Paris VI, 2014. English. NNT : 2014PA066239 . tel-01127089

HAL Id: tel-01127089

<https://theses.hal.science/tel-01127089>

Submitted on 6 Mar 2015

HAL is a multi-disciplinary open access archive for the deposit and dissemination of scientific research documents, whether they are published or not. The documents may come from teaching and research institutions in France or abroad, or from public or private research centers.

L'archive ouverte pluridisciplinaire **HAL**, est destinée au dépôt et à la diffusion de documents scientifiques de niveau recherche, publiés ou non, émanant des établissements d'enseignement et de recherche français ou étrangers, des laboratoires publics ou privés.



Université Pierre et Marie Curie

Chimie physique et chimie analytique de Paris Centre

Processus de diffusion dans des membranes biologiques étudiés par simulation moléculaire et modèles analytiques

par Sławomir Stachura

Pour obtenir le grade de Docteur

Dirigée par Gerald Kneller

Presentée et soutenue publiquement le 08.07.2014

Devant un jury composé de :

Ralf Metzler, Professeur à l'Université de Potsdam, Allemagne (Rapporteur)

Mark Johnson, Professeur à l'Université de Nottingham, Angleterre & ILL Grenoble (Rapporteur)

Marie Jardat, Professeur à l'Université de Pierre et Marie Curie (Examinatrice)

Gerald Kneller, Professeur à l'Université d'Orléans (Directeur de thèse)



Except where otherwise noted, this work is licensed under <http://creativecommons.org/licenses/by-nc-nd/3.0/>



Diffusion processes in biological membranes studied by molecular dynamics simulations and analytical models

A Dissertation Submitted
to obtain the Doctoral Degree of
Pierre and Marie Curie University

Sławomir Stachura

8 July 2014

Moim Bliskim

Acknowledgements

A PhD thesis might appear as a solitary undertaking, but in reality there are many people who contributed in various ways to the research in this work and created opportunities for me to gain invaluable experience and knowledge.

First and foremost, I would like to thank Gerald Kneller for being my supervisor and mentor. I appreciate all his help, ideas and constructive critiques, which taught me professionalism and encouraged me to immerse myself in scientific work. During our conversations we often talked beyond academic matters and also these discussions were important life lessons, which I enjoyed greatly. Furthermore, I am grateful to Konrad Hinsen for his valuable tips for my thesis, and especially for showing me that one can be an excellent physicist and at the same an outstanding programmer. For this thesis I would also like to thank Guillaume Chevrot and Tran Viet-Dung for all their help. I also appreciate many discussions with Daniel Abergel, Mark Johnson, Eric Pellegrini and other scientists whom I met over these years. I would also like to express my gratitude to Marta Pasenkiewicz-Gierula and members of her group, Krzysztof Baczyński and Michał Markiewicz, for their useful advices concerning molecular dynamics simulations of biological membranes. Finally, I would also like to acknowledge financial support by the Agence Nationale de la Recherche.

Last but not least, I would like to thank my family and friends for all their love and support. For my parents who provided me with encouragement and unconditionally supported me in all my pursuits. Thank you!

Abstract

Various recent experimental and simulation studies show that the lateral diffusion of molecules in biological membranes exhibits anomalies, in the sense that the molecular mean square displacements increase sub-linearly instead of linearly with time. Mathematically, such diffusion processes can be modeled by generalized diffusion equations which involve an additional fractional time derivative compared to the corresponding normal counterpart.

The aim of this thesis is to gain some more physical insight into the lateral diffusion processes in biological membranes. For this purpose, molecular dynamics simulations of a lipid POPC bilayer are analyzed by employing concepts from the statistical physics of liquids. The long-time tail of the center-of-mass velocity autocorrelation function, which reflects the diffusional regime of the molecules under consideration, is related to their low-frequency dynamics and to the dynamical structure around each molecule. The latter is studied in terms of the time dependent van Hove pair correlation function for their centers-of-mass. It is in particular demonstrated that the first shell of neighbors of a diffusing lipid molecule decays very slowly with $t^{-\beta}$, with $0 < \beta < 1$. This finding is in agreement with the observation that lipid molecules tend to form collective flow patterns, which has been recently reported by other authors.

In order to evaluate the impact of the molecular dynamics force field on the nature of the observed diffusion process, the POPC bilayer was simulated with the OPLS all atom force field and with the coarse-grained MARTINI force field. In the latter, four heavy atoms are combined into one “bead”. In both cases lateral sub-diffusion with similar exponents is observed, but the diffusional motion obtained with the coarse grained force field is about three times faster and appears also to be faster than in experiments. This result is reflected in the low-frequency dynamics of the POPC molecules and in the dynamical structure of their local environment.

Keywords : subdiffusion, simulations, molecular dynamics, lipids, membranes

Résumé

De nombreuses études récentes, expérimentales et in-silico, montrent que la diffusion latérale des molécules dans des membranes biologiques présentent des anomalies, dans le sens que les déplacements carré moyen moléculaires évoluent de façon sublinéaire au lieu de linéaire avec le temps. Mathématiquement, ce type de diffusion peut être modélisé par des équations de diffusion généralisées, dans lesquelles une dérivée fractionnaire du temps s'ajoute à l'équation de diffusion normale correspondante.

Le but de cette thèse est d'obtenir un aperçu plus physique des processus de diffusion dans des membranes biologiques. A cet effet, des simulations de dynamique moléculaire d'une bicouche lipidique POPC sont analysées en utilisant les concepts de la physique statistique des liquides. La queue aux temps longs de la fonction d'autocorrélation de vitesses des centres de masse, qui reflète le régime de diffusion des molécules en question, est mise en relation avec leur dynamique aux basses fréquences et avec la structure dynamique autour de chaque molécule. La dernière est caractérisée par la fonction de corrélation de paires dynamique de van Hove pour leurs centres de masse. Il est en particulier montré que la première couche de voisins d'une molécule lipidique qui diffuse ne se désintègre que très lentement avec $t^{-\beta}$, où $0 < \beta < 1$. Ce résultat est en accord avec l'observation faite par d'autres auteurs, que les molécules dans une bicouche lipidique ont la tendance de se déplacer d'une manière concertée.

Afin d'évaluer l'impact du champ de force sur la nature des processus de diffusion observés, la bicouche lipidique POPC a été simulée avec le champ de force tout atome OPLS et avec le champ de force à gros grains MARTINI. Dans le second, quatre atomes lourds forment un seul "grain". Dans les deux cas, on observe une sous-diffusion latérale, avec des exposants similaires, mais la diffusion des lipides obtenue avec le champ de force à gros grains est d'environ trois fois plus rapide et elle apparaît aussi plus rapide que dans des expériences correspondantes. Ce résultat est confirmé par la dynamique des molécules POPC à basse fréquence et par la structure dynamique de leur environnement local.

Mots clés : sous-diffusion, simulations, dynamique moleculaire, lipides, membrane

Résumé Substantiel

I. INTRODUCTION

Une membrane biologique est une enveloppe continue qui joue le rôle de barrière physique délimitant la cellule: elle sépare le milieu intracellulaire (tout ce qui compose la cellule) du milieu extracellulaire (l'environnement de la cellule). Il existe également des membranes biologiques intracellulaires, qui délimitent les organites (par exemple les membranes mitochondriale, nucléaire, lysosomiale, etc.) [Berg *et al.* [2005]]. Toutes les membranes sont composées principalement de lipides, dont les plus abondants sont les phospholipides (Fig. 1). Ces lipides forment des mono- ou bicouches fermées. Une membrane biologique contient également de nombreuses autres molécules, comme des protéines membranaires ou des glucides [Alberts *et al.* [2005]]. Leur présence permet le transport bi-directionnel de petites molécules à travers la membrane, ce qui intervient dans l'adhésion des cellules et dans des nombreux processus enzymatiques. Tous ces processus sont fortement influencés par la diffusion latérale (dans le plan de la bicouche) des lipides, qui peut être caractérisée par l'évolution dans le temps du déplacement carré moyen (DCM) d'une molécule, qui, dans le régime asymptotique $t \rightarrow \infty$, prend la forme

$$W(t) = \langle (\mathbf{x}(t) - \mathbf{x}(0))^2 \rangle \stackrel{t \rightarrow \infty}{\sim} 2D_\alpha t^\alpha, \quad 0 < \alpha < 2. \quad (1)$$

Ici \mathbf{x} signifie la position de la molécule, D_α est la constante fractionnaire de diffusion et le paramètre α décrit le type de diffusion. Pour $\alpha = 1$, nous avons une diffusion

dite normale, ce qui caractérise les liquides simples (par exemple l'eau). Le régime $0 < \alpha < 1$ est typique pour les systèmes "crowded". On l'appelle la sous-diffusion. Pour $1 < \alpha < 2$, nous avons la super-diffusion, ce qui signifie que les mouvements des molécules sont accélérés. Les expériences et les simulations par dynamique moléculaire montrent des résultats contradictoires pour la diffusion latérale des lipides. Les expériences de diffusion

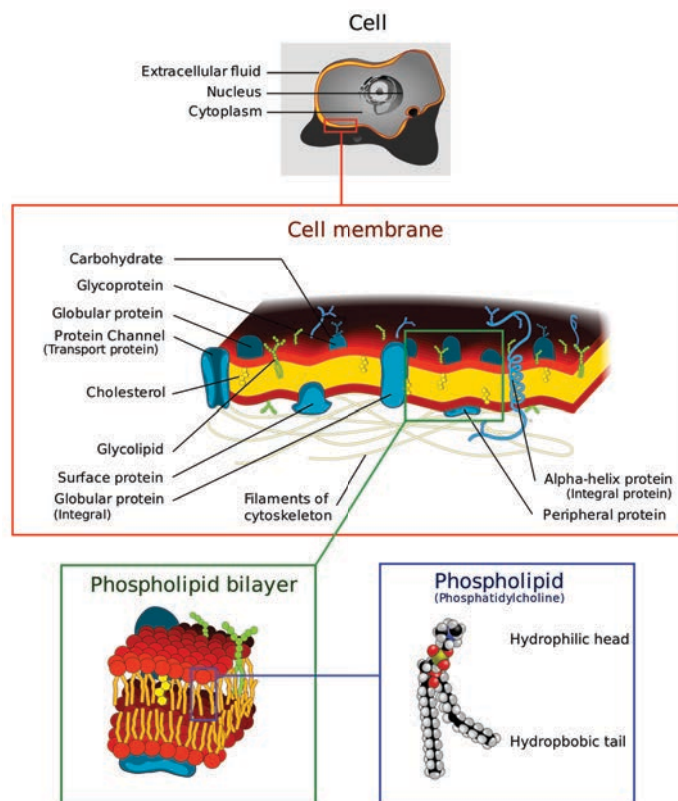


Figure 1: La complexité d'une membrane biologique ¹.

de neutrons révèlent, en générale, que la diffusion des lipides est normale [Armstrong *et al.* [2011]]. En même temps, sur une échelle de temps beaucoup plus grande, on observe une sous-diffusion par la spectroscopie de fluorescence [Schwille *et al.* [1999b]]. De même, certaines simulations par dynamique moléculaire montrent un mouvement sous-diffusif des

¹Source : http://commons.wikimedia.org/wiki/File:Cell_membrane_detailed_diagram_4.svg

lipides [Arnold *et al.* [2004]; Jeon *et al.* [2012]; Kneller *et al.* [2011]; Stachura & Kneller [2013]], pendant que d'autres études soulignent que la sous-diffusion est transitoire et que pour des temps plus longs la diffusion devient normale [Flenner *et al.* [2009]; Goose & Sansom [2013]; Niemelä *et al.* [2010]]. La sous-diffusion peut être comprise par un "effet de cage" qui s'exprime dans la fonction d'autocorrélation des vitesses $C_{vv} = \langle \mathbf{v}(0) \cdot \mathbf{v}(t) \rangle$, où \mathbf{v} signifie la vitesse de la molécule, par une valeur négative à des temps longs [Kneller [2011]]. Dans cette thèse, cette "cage", formée par les voisins les plus proches autour de chaque lipide, est étudiée par la fonction de corrélation de paire vue comme fonction du temps [Rahman [1963]; Van Hove [1954]]:

$$G_D(\mathbf{r}, t) = \frac{V}{N} \frac{n(\mathbf{r}, t)}{\delta V}. \quad (2)$$

Elle montre les fluctuations de la structure formée par les voisins lipidiques à la distance \mathbf{r} de la molécule entourée. Ici V et N sont le volume total du système et le nombre de molécules, respectivement, et $n(\mathbf{r}, t)$ est le nombre de molécules présentes dans l'élément de volume/surface δV à la distance \mathbf{r} .

L'objectif de cette thèse est d'obtenir une description plus physique des processus de diffusion des lipides, en s'appuyant sur la simulation par dynamique moléculaire (MD) et la théorie des liquides. Les trajectoires MD ont été analysées pour en extraire le comportement à des temps longs des fonctions de corrélation.

II. SIMULATIONS DE DYNAMIQUE MOLECULAIRE

Une série de simulations par dynamique moléculaire d'une bicouche lipidique de 1-palmitoyl-2-oleoylphosphatidylcholine (POPC) a été calculée pour deux modèles moléculaires : tout-atome OPLS [Jorgensen & Tirado-Rives [1988]; Jorgensen *et al.* [1996]] et gros-grain MARTINI [Marrink *et al.* [2004, 2007]] (Fig. 2).

Une membrane tout-atome consistant de 274 molécules de POPC a été simulée pen-

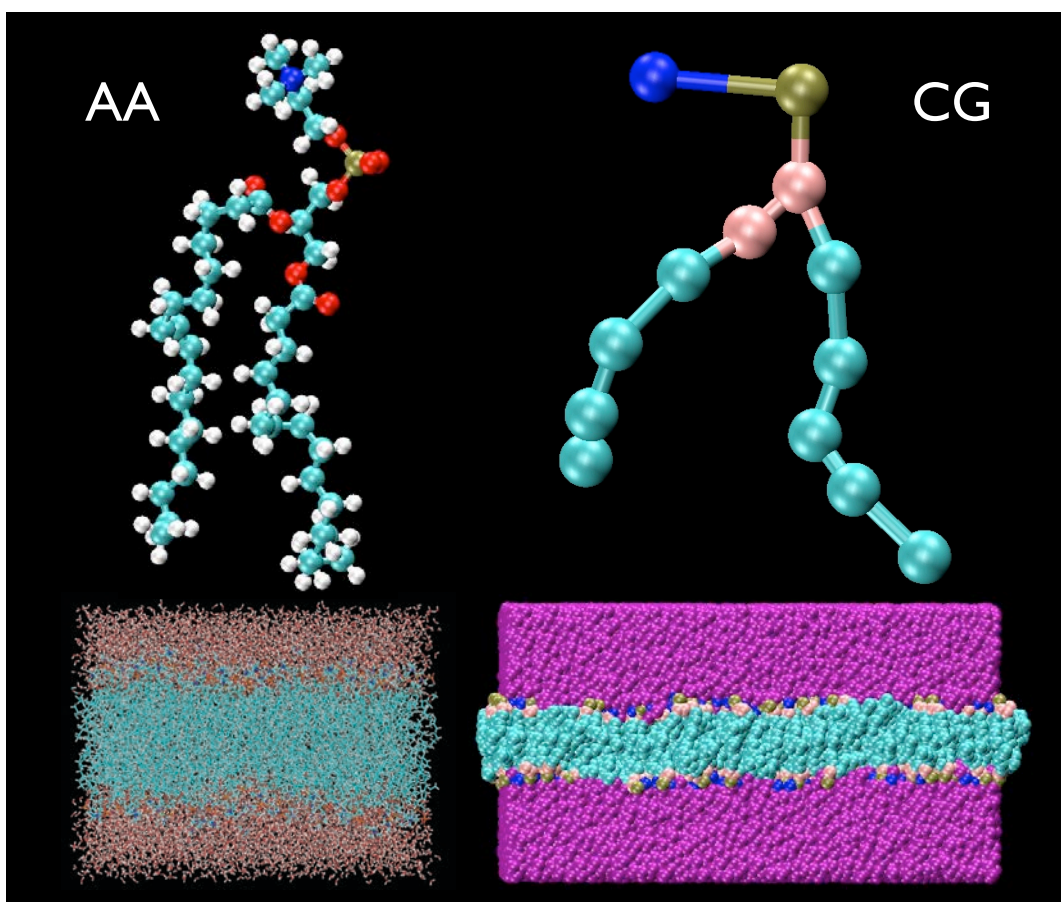


Figure 2: Comparaison entre les modèles tout-atome OPLS (AA) et gros-grain MARTINI (CG) de membrane de POPC.

dant 15 ns et 150 ns, dans l'ensemble isobare- isotherme [Stachura & Kneller [2013]]. La température de 310 K a été contrôlée par un thermostat de Nosé-Hoover [Hoover [1985]; Nosé [1984]] et la pression de 1 atm par un barostat de Parrinello-Rahman [Parrinello [1981]].

Afin d'avoir un accès à des temps de simulation plus longs pour une plus grande bicouche de POPC, des simulations MARTINI ont été effectuées pour un système de 2033 lipides pendant 600 ns, dans deux conditions thermodynamiques: NVT et NAp_zT (pression ajustée uniquement dans la direction perpendiculaire à la bicouche) [Stachura & Kneller

[2013]]. La température de 320 K a été fixée par le thermostat de Berendsen et la pression de 1 atm pour l'ensemble NAP_zT par la barostat de Berendsen [Berendsen & Postma [1984]. Ces calculs ont été aussi servi pour tester la capacité du modèle gros-grains de reproduire les propriétés dynamiques des systèmes tout-atome.

III. RESULTATS

Les analyses de l'évolution temporelle du déplacement carré moyen (DCM) du centre de masse des lipides ont montré des deviations de la forme linéaire caractéristique pour la diffusion normale. Les fits de l' éq. 1 (Fig. 3) ont donné des paramètres $\alpha \approx 0.68$ et

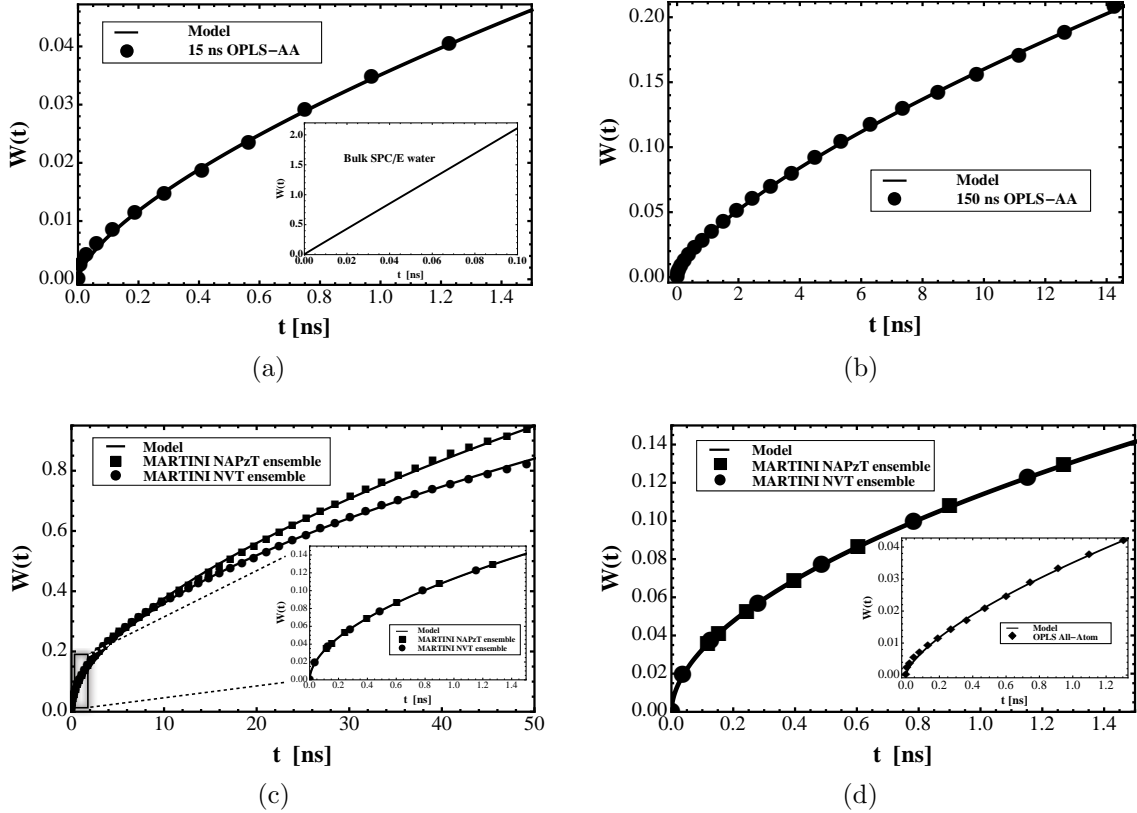


Figure 3: Les fits de l' éq. 1 de déplacement carré moyen pour les simulations: a) 15 ns OPLS-AA, b) 150 ns OPLS-AA, c) NVT et NAP_zT MARTINI pour des temps maximales de 50 ns et d) NVT et NAP_zT MARTINI pour des temps maximales de 1.5 ns.

$\alpha \approx 0.7$ pour les simulations OPLS-AA de 15 ns et de et 150 ns, ce qui correspond à la sous-diffusion dans le régime asymptotique ($t \rightarrow \infty$). Des résultats similaires ont été obtenues pour les simulations MARTINI, avec $\alpha \approx 0.57$ et $\alpha \approx 0.56$ pour les ensembles NAP_zT et NVT . Les constantes fractionnaires de diffusion sont de $D_\alpha \approx 0.018 \text{ nm}^2/\text{ns}^\alpha$ pour 15 ns et $D_\alpha \approx 0.016 \text{ nm}^2/\text{ns}^\alpha$ pour 150 ns (OPLS-AA) et de $D_\alpha \approx 0.051 \text{ nm}^2/\text{ns}^\alpha$ pour les deux simulations MARTINI. Ces valeurs sont du même ordre que les résultats expérimentaux ($D_\alpha \approx 0.101 \text{ nm}^2/\text{ns}^\alpha$) [Schwille *et al.* [1999b]].

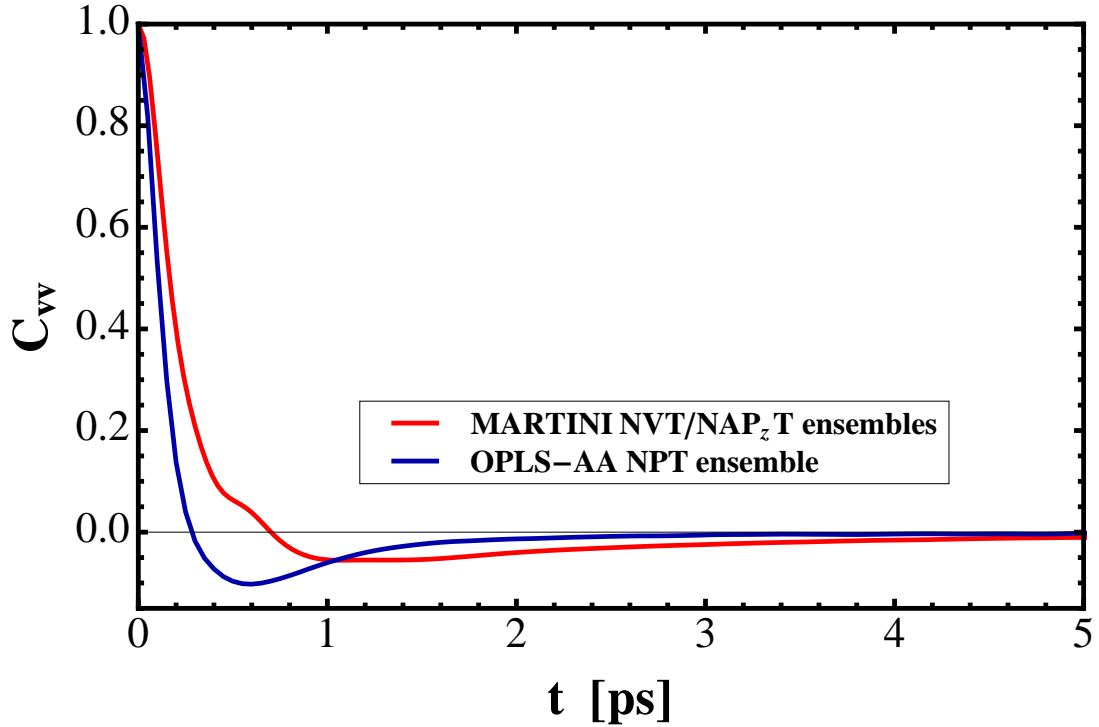


Figure 4: Comparaison entre les fonctions d’autocorrélation des vitesses pour les simulations de OPLS-AA et MARTINI.

Un observation similaire est faite pour les densités d’états (DOS) des centres de masse. Tous les DOS, calculés en utilisant trois méthodes différentes (par transformation de Fourier des fonctions d’autocorrélation de vitesse, FACVs, par estimation d’un processus auto-régressif, et par le facteur de structure dynamique incohérent, FSDI), donnent en

moyenne $\alpha \approx 0.45$ pour les deux champs de force (MARTINI et OPLS-AA). Ceci suggère encore moins une diffusion normale des lipides POPC dans le plan des bicouches que l'analyse des DCMs.

L'origine des mouvements sous-diffusifs des lipides a été expliquée par un "effet de cage". Il s'agit de la tendance des lipides d'inverser leurs vitesses et de rester plus localisées, ce qui s'exprime dans le comportement asymptotique de la fonction d'autocorrélation des vitesses qui est négative [Kneller [2011]]. En effet, un tel comportement peut être observé pour les deux modèles, OPLS-AA et MARTINI, même si cet effet est beaucoup plus faible

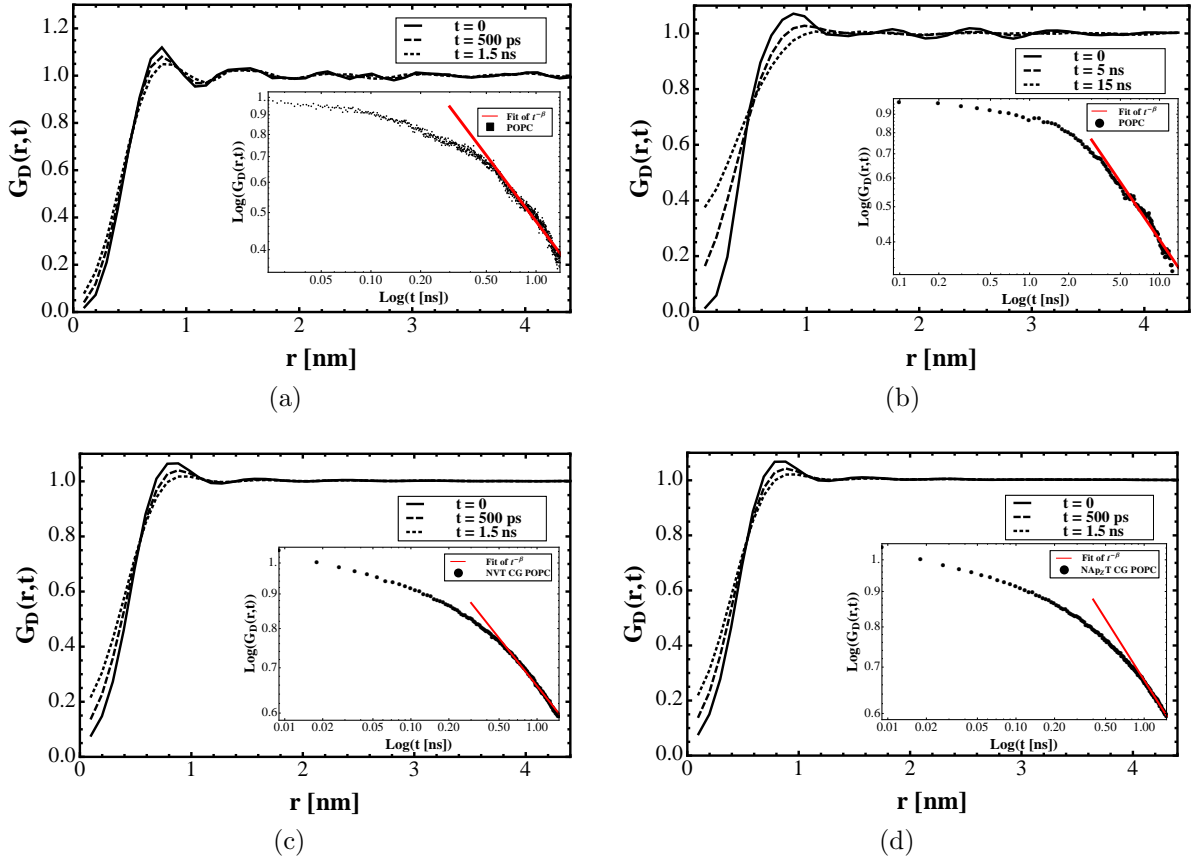


Figure 5: Les fonctions de corrélation de paire distincte dépendantes du temps, $G_D(r, t)$ pour les simulations: a) 15 ns OPLS-AA, b) 150 ns OPLS-AA, c) NVT MARTINI et d) et $N A p_z T$ MARTINI. Dans les encarts sont montrés les fits de des temps longs.

dans le deuxième cas, ce qui signifie que la cage formée par les voisins est plus souple que pour les simulations tout-atome (Fig. 4).

Afin de visualiser cette cage, les fonctions de corrélation de paire distincte dépendantes du temps, $G_D(r, t)$, ont été calculées pour les quatre simulations de POPC (15 ns et 150 ns OPLS et 600 ns *NVT* et *N_Ap_zT* MARTINI) et pour une boîte d'eau SPC/E simulée pendant 1 ns dans l'ensemble NVT. L'analyse asymptotique de la dissolution dans le temps de la première couche de voisins a montré une cage persistante, formée autour de chaque lipide tout-atome, avec une décroissance algébrique à des temps longs (Fig. 5).

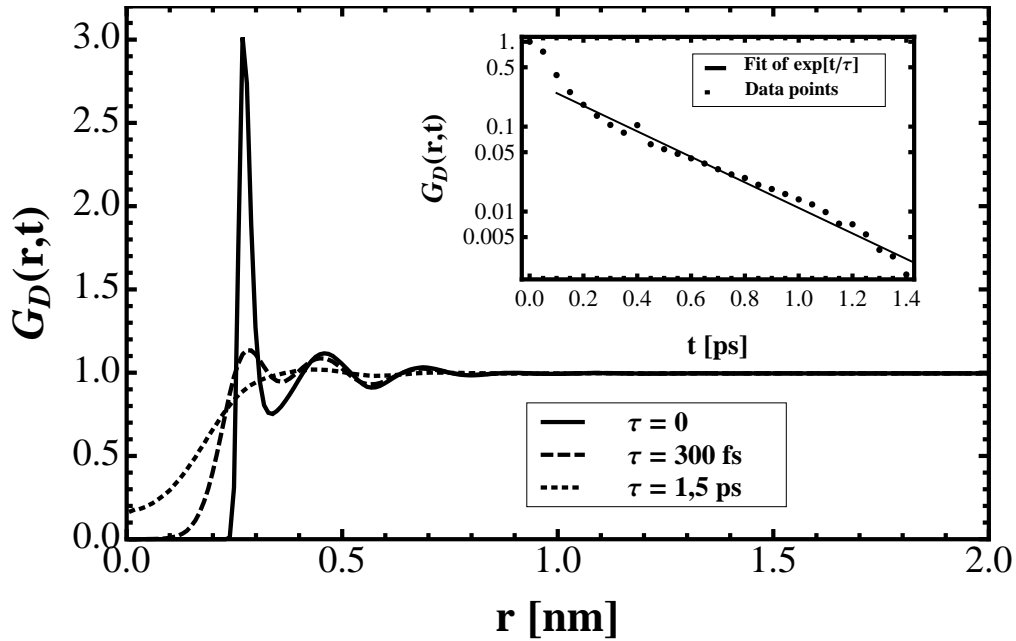


Figure 6: La fonction de corrélation de paire distincte dépendantes du temps, $G_D(r, t)$, pour la simulation de l'eau SPC/E.

L'effet de cage est préservé pendant des temps allant jusqu'à 10% de la longueur totale des trajectoires MD. En revanche, le $G_D(r, t)$ pour la décroissance de l'eau est beaucoup plus rapide (3 ordres de grandeur) et aussi exponentielle (Fig. 6). Ce résultat confirme

l'existence d'une forte corrélation entre les lipides et leurs voisins, l'effet de cage, qui est aussi une explication plausible pour la sous-diffusion des lipides POPC dans la bicouche. Dans le cas des simulations gros-grains, la décroissance de la première couche de voisins est aussi algébrique, mais la décorrélation complète des fonctions $G_D(r, t)$ est visible pour des temps inférieurs à 1% de la longueur totale des trajectoires MD. Ceci pourrait indiquer les limites du modèle gros-grains MARTINI pour reproduire complètement les propriétés dynamiques des systèmes lipidiques.

IV. CONCLUSION

Dans cette thèse, on a été montré que les mouvements latéraux des lipides POPC sont sous-diffusifs pour deux modèles: le modèle tout-atoms OPLS et le modèle gros-grains MARTINI. L'effet de cage associé à la sous-diffusion a été mis en évidence par la fonction de corrélation de paire dépendante du temps, $G_d(r, t)$. Pour les simulations des lipides POPC, $G_d(r, t)$ a montré une couche de voisins les plus proches très stable dans le temps, qui se désintègre avec le temps de façon algébrique. Avec le modèle MARTINI, cette décroissance est beaucoup plus rapide, ce qui peut indiquer les limites de ce type de champ de force pour reproduire entièrement la dynamique réelle.

Contents

Abstract	i
Résumé	iii
Résumé Substantiel	v
Contents	xiv
List of Figures	xvii
1 General Introduction	1
1.1 Biological membranes	1
1.2 Transport of molecules in cells and membranes	7
1.3 Modeling anomalous diffusion	11
1.4 Recent simulation work	14
2 Concept of Molecular Dynamics Simulations	17
2.1 Classical Molecular Dynamics Simulations	19
2.1.1 Concept and potential function	19
2.1.2 Periodic boundary conditions and treatment of electrostatic inter- actions	22
2.2 Treatment of thermodynamic conditions	24

3	Simulated systems and simulations	26
3.1	System setup	26
3.1.1	All-atom OPLS force-field	26
3.1.2	Coarse-grained MARTINI force-field	28
3.2	Membrane simulations	30
3.2.1	OPLS-AA force-field	30
3.2.1.1	System equilibration	31
3.2.1.2	Short production run - 15 ns	31
3.2.1.3	Extended simulation - 150 ns	34
3.2.2	MARTINI force-field	36
3.2.2.1	System equilibration	36
3.2.2.2	600 ns production run in the canonical ensemble	37
3.2.2.3	600 ns production run in the NAp_zT ensemble	38
3.3	Bulk water reference simulation	38
4	Results	40
4.1	Single molecule dynamics in a lipid bilayer	40
4.1.1	Mean Square Displacements	41
4.1.1.1	Atom-detailed simulations	41
4.1.1.2	Coarse-grained force-field results	44
4.1.1.3	Comparison between OPLS-AA and MARTINI force-fields	47
4.1.1.4	Bulk water comparison with membrane hydration water	49
4.1.2	Velocity autocorrelation function analysis	53
4.1.3	Density of States (DOS)	58
4.1.3.1	DOS as Fourier transform of VACF	58
4.1.3.2	Density of the States from the Autoregressive Model	65
4.1.4	Conclusions	71
4.2	Collective motions of lipids	71

CONTENTS

4.2.1	Pair Correlation Function	72
4.2.2	Visualization of the cage effect	74
4.2.3	Conclusions	84
5	Conclusions	85
6	Publications	88
	References	89

List of Figures

1	La complexité d'une membrane biologique ¹	vi
2	Comparaison entre les modèles tout-atome OPLS (AA) et gros-grain MARTINI (CG) de membrane de POPC.	viii
3	Les fits de l' éq. 1 de déplacement carré moyen pour les simulations: a) 15 ns OPLS-AA, b) 150 ns OPLS-AA, c) <i>NVT</i> et <i>N_Ap_zT</i> MARTINI pour des temps maximales de 50 ns et d) <i>NVT</i> et <i>N_Ap_zT</i> MARTINI pour des temps maximales de 1.5 ns.	ix
4	Comparaison entre les fonctions d'autocorrélation des vitesses pour les simulations de OPLS-AA et MARTINI.	x
5	Les fonctions de corrélation de paire distincte dépendantes du temps, $G_D(r, t)$ pour les simulations: a) 15 ns OPLS-AA, b) 150 ns OPLS-AA, c) <i>NVT</i> MARTINI et d) et <i>N_Ap_zT</i> MARTINI. Dans les encarts sont montrés les fits de des temps longs.	xi
6	La fonction de corrélation de paire distincte dépendantes du temps, $G_D(r, t)$, pour la simulation de l'eau SPC/E.	xii
1.1	Illustration ¹ showing the complexity of a membrane in cells and the structure of a lipid molecule. [1.3cm]	2
1.2	Schematic ² of the phosphatidylcholine chemical structure.	4
1.3	Sketch of the POPC chemical structure ³	6

LIST OF FIGURES

1.4	Crowded cell compartments visualized by cryoelectron microscopy ⁴ Actin filaments are shown in orange, ribosomes and other macromolecular assemblies in grey, and membrane structures in blue.	8
1.5	Illustration of a chromosome ⁵ , depicting its parts; the endings of each of the four arms(3,4), called telomeres (1) and the centromere (2) connecting the two chromatides.	9
1.6	Visualization of ion trafficking in cells involving Golgi apparatus and rectifier potassium channels (inward and delayed) ⁶ . The ion channels are synthesized in endoplasmic reticulum and through Golgi are transported to the plasma membrane.	10
1.7	Recorded diffusion of putty grains published by Perrin [1909].	12
1.8	MSD of a model system for various values of α [Kneller [2011]].	13
1.9	Plot representing the displacements of the DPPC lipids in x and y planes for the upper leaflet (a,b,c) and lower leaflet (d); (a) shows a 50 ps interval from 5.00 to 5.05 ns of the simulation, (b) a 500 ps interval from 5.0 to 5.5 ns, (c) a 5 ns interval from 5 to 10 ns, and (d) a 30 ns interval from 10 to 40 ns [Falck <i>et al.</i> [2008]].	15
2.1	Results of one of the first molecular dynamics simulation published by Alder [Alder & Wainwright [1957, 1959]] - the figure shows traces of the simulated hard sphere particles for about 3000 collisions.	17
2.2	Structure of the first simulated protein - bovine pancreatic trypsin inhibitor (BPTI) ¹⁰ . On the bottom of the figure is written full amino acid sequence of this protein.	18

4.

LIST OF FIGURES

2.3	Illustration of the periodic boundary conditions (PBC) method with the minimum image convention. The box in the middle is replicated in all directions and the non-bonded interactions are calculated only for the closest atoms or their images.	23
3.1	Simulated box of POPC all-atom model membrane. The system consists of total 274 lipids embedded in 10 471 water molecules.	27
3.2	Simulated box of POPC coarse-grained model membrane. The system consists of 2033 lipids hydrated by 231 808 water molecules.	28
3.3	Comparison between all-atom and coarse-grained models of POPC membrane.	29
3.4	Total energy of the POPC bilayer during 15 ns simulation with OPLS-AA force-field. The system is in equilibrium.	32
3.5	Plots representing the behavior of the system during the 15 ns production run. The plots show fluctuations of : a) the simulation box in all three dimensions; b) the area surface per lipid. Both are stable with the mean value of the latter of $0.638 \pm 0.004 \text{ nm}^2$, which indicates that the system is in equilibrium.	33
3.6	Total energy of the POPC bilayer of 150 ns all-atom simulation - the system is in energetic equilibrium.	34
3.7	Plots show the fluctuations of the box (a) and the surface area per POPC (b) for 150 ns simulation. The mean area per lipid of $0.637 \pm 0.006 \text{ nm}^2$ is close to the value obtained for the 15 ns simulation.	35
3.8	Total energy of 600 ns MARTINI simulation in NVT conditions.	37
3.9	Total energy fluctuations of 600 ns MARTINI simulation in the $N A p_z T$ ensemble.	38
3.10	Fluctuations of the total energy of the reference box of bulk SPC/E water simulated for 100 ps.	39

LIST OF FIGURES

4.1	The MSD, $W(t)$, calculated for the centres of the masses of the POPC lipids simulated for 15ns (a) and 150 ns (b). The inset in (a) shows the MSD for normal diffusion (SPC/E water).	42
4.2	The MSD, $W(t)$, calculated for the centres of the masses of the lipids simulated for 600 ns.	46
4.3	Comparison of the centre of mass MSDs calculated for the 15 ns all-atom and the 600 ns coarse-grained simulations (the maximal time-lag is 1.5 ns).	47
4.4	$W(t)$, calculated for the centres of the masses of the bulk SPC/E water simulated for 100 ps.	50
4.5	The MSD, $W(t)$, calculated for the centres of the masses of the water around POPC bilayer in case of 15 ns all-atom simulation (a) and 600 ns MARTINI (b).	51
4.6	Comparison of the centre of mass Velocity Autocorrelation Functions calculated for the 15 ns all-atom and 600 ns coarse-grained simulations.	56
4.7	Comparison of the integrals over the centre of mass VACFs calculated for the 15 ns all-atom and 600 ns coarse-grained simulations.	57
4.8	Calculated densities of states from the VACFs Fourier transforms for the 600 ns MARTINI simulations (CG) and 15 ns OPLS-AA simulation (AA - the inset).	62
4.9	Figures show the fits of Expression for the DOS (4.24) for the MARTINI (a) and the OPLS-AA (b) simulations. The insets present values of the function $s(\omega)$, Eq. (4.25), for the α parameters obtained from the fits (the red line is the value of D_α from the MSD calculations).	63
4.10	The figures show the densities of states for MARTINI (a) and OPLS-AA (b) estimated by AR model. In the insets are presented the results of the FT method for comparison.	68

LIST OF FIGURES

4.11 Comparison of estimated densities of states by the autoregressive model (AR) for the 600 ns MARTINI simulations (CG) and 15 ns OPLS-AA simulation (AA - the inset).	69
4.12 Figures show the fits of Eq. (4.24) to the autoregressive DOS for the MARTINI (a) and OPLS-AA (b) simulations. The insets compare the evolution of $s(\omega)$ with the value of D_α obtained from the MSD fits.	70
4.13 The schematic visualising the definition of the pair distribution function ¹¹	73
4.14 The pair distribution function, $g(r)$, for the bulk SPC/E water.	75
4.15 Three dimensional plots of the distant time- dependant pair correlation functions, $G_D(r, t)$, for the all-atom POPC 15 ns (a) and 150 ns (b) simulations.	76
4.16 3D plots of the $G_D(r, t)$, for the 600 ns NVT (a) and NAp_zT (b) MARTINI simulations.	77
4.17 3D plot of the computed $G_D(r, t)$ for the simulated bulk SPC/E water.	78
4.18 Plots show the calculated $G_D(r, t)$ of the OPLS-AA 15 ns (a) and 150 ns (b) simulations for three time-lags. Visible slow time decay of the first shell of neighbours in long time-tail analysis, the log-log plots in the insets, indicate power-law behavior.	79
4.19 Pair correlation function for the centre of mass of SPC/E water molecules for three time slices : $t = 0$ (solid line), $t = 300$ fs (dashed line) and $t = 1.5$ ps (dotted line). The first shell of neighbours, in log plot shown on the inset, decays rapidly and exponentially.	80
4.20 The $G_D(r, t)$ of the MARTINI NVT (a) and NAp_zT (b) simulations for three time lags : $t = 0$ (solid line), $t = 500$ ps (dashed line) and $t = 1.5$ ns (dotted line). Similarly to the all-atom case, the long-time tails (the insets) decay as a power-law.	81

4.21 Figures show the β parameter dependence on the time-lag, defining the beginning of the $G_D(r, t)$ long-time tail for the simulations : (a) 15ns OPLS-AA, (b) 150 ns OPLS-AA, (c) 600 ns *NVT* MARTINI and (d) 600 ns *NAp_zT* MARTINI. The maximal time-lag for which the $G_D(r, t)$ functions were computed is denoted by t_{MAX} 83

Chapter 1

General Introduction

1.1 Biological membranes

Biological membranes are one of the most important constituents of prokaryotic and eukaryotic cells. The very beginning of life can be related to the formation of a biological compartments protecting the very first organisms from their environment. This was possible only with the existence of biological membranes - physical barriers between cells and their exterior. A following step in the evolution of cells was a further compartmentalization of cells, leading to the formation of organelles. In this way, biological membranes allowed various microenvironments to coexist within cells, which increased their ability to adapt to different environments. A biological membrane consists of lipid molecules forming mono- and bi- layers. These layers, in cellular conditions, always form closed structures because of hydrophobic effects resulting from interactions between lipids and water molecules [Berg *et al.* [2005]]. The reason is that a lipid molecule has a hydrophobic part - a water-repulsive tail, and a hydrophilic one - a water-attractive headgroup. In order to shield hydrophobic regions from water, lipids organize themselves in an aggregated phase. A biological membrane contains also many other diverse types of molecules and actually is a very complex and heterogeneous system [Alberts *et al.* [2005]]. This is

1. General Introduction

why biological membranes play also an important role in the bidirectional transport of molecules across the bilayer (or monolayer), in relaying signals, in the adhesion of cells, and in many enzymatic processes.

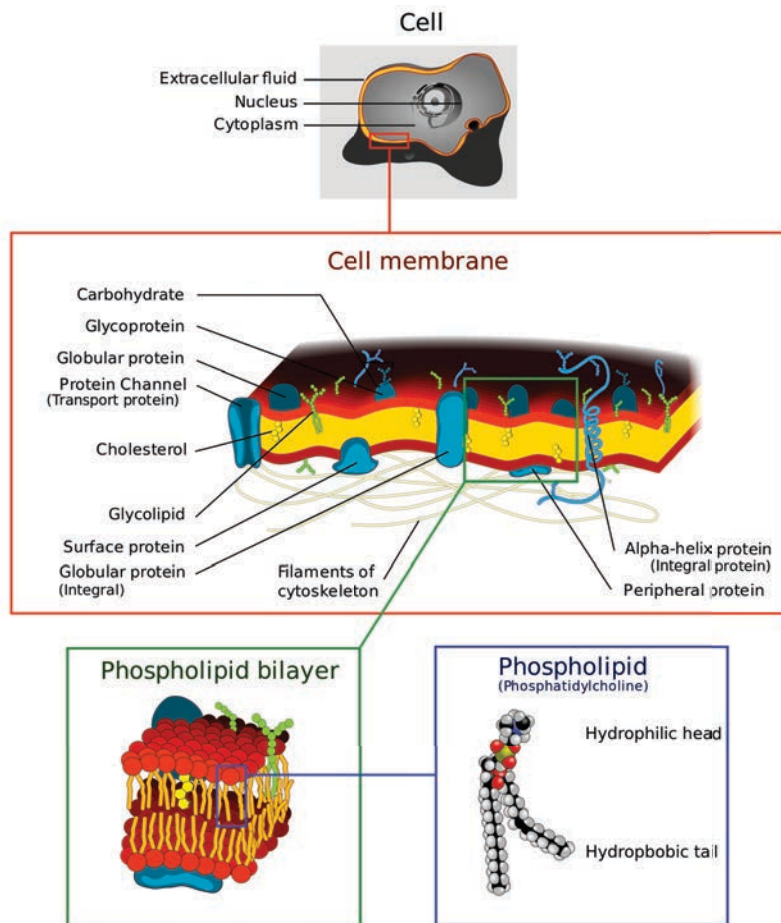


Figure 1.1: Illustration¹ showing the complexity of a membrane in cells and the structure of a lipid molecule.

¹Source : http://commons.wikimedia.org/wiki/File:Cell_membrane_detailed_diagram_4.svg

1. General Introduction

Lipids are a very diverse group of chemical compounds that are either hydrophobic or amphipathic (soluble in both - water and fats) [Berg *et al.* [2005]]. The lipids can refer to amassed fatty acids in a volume, more complex steroids, or phospholipids. Table 1.1 shows that cholesterol, cardiolipin and phospholipids are the most abundant lipids in animal cell membranes. The percentage of the total masses in different tissues indicates that the most abundant are phosphatidylcholine and phosphatidylethanolamine (phospholipids) and cholesterol for erythrocytes.

Table 1.1: Lipid composition in the heart, liver, erythrocytes and plasma (weight percentage of the total) [Christie [1985]].

LIPID CLASS	TISSUE			
	Heart	Liver	Erythrocytes	Plasma
Cholesteryl esters	0.22 ± 0.04	1.47 ± 0.10	-	16.04 ± 0.30
Triacylglycerols	3.77 ± 0.23	6.66 ± 0.15	-	48.65 ± 0.71
Cholesterol	4.06 ± 0.16	5.40 ± 0.13	30.23 ± 0.34	5.65 ± 0.10
Diacylglycerols	0.65 ± 0.07	-	0.38 ± 0.09	0.54 ± 0.06
Phosphatidylethanolamine	33.44 ± 0.21	19.91 ± 0.08	20.75 ± 0.21	-
Phosphatidylinositol	3.69 ± 0.06	4.43 ± 0.08	3.42 ± 0.14	-
Phosphatidylserine	-	-	3.11 ± 0.46	-
Phosphatidylcholine	38.57 ± 0.20	55.18 ± 0.13	32.03 ± 0.14	24.13 ± 0.59
Sphingomyelin	1.76 ± 0.50	2.09 ± 0.06	8.22 ± 0.17	1.99 ± 0.07
Lysophosphatidylcholine	-	-	0.89 ± 0.15	1.35 ± 0.06

Phospholipids have three main moieties (Fig. 1.2):

1. A hydrophilic headgroup, which consists of the phosphate group and additional groups, e.g. a $N(CH)_3$ group. The latter is called a choline group and is a part of phosphatidylcholines. Another example for a headgroup is the ethanolamine rest in phosphatidylethanolamine.

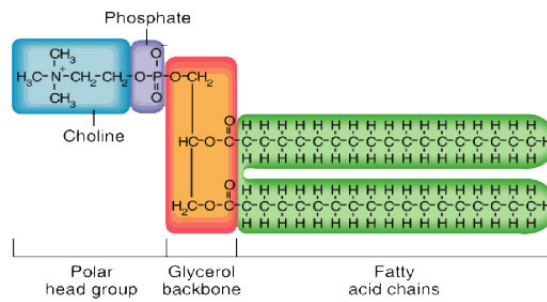


Figure 1.2: Schematic ² of the phosphatidylcholine chemical structure.

2. A backbone, consisting mostly of derivatives of glycerol, but in case of sphingomyelins, the base is a sphingosine, which is an amino alcohol with unsaturated fatty acid rest.

Table 1.2: Lipid abundance in different organelles in rat liver (weight percentage of the total) [A - Wuthier [1966], B - Gurr *et al.* [1965], C - Colbeau *et al.* [1971]].

LIPID CLASS	WHOLE TISSUE [A]	MEMBRANE			
		Nuclei [B]	Mitochondria [C]	Microsomes [C]	Plasma [C]
Phosphatidylethanolamine	25.2 ± 0.5	26.1	33.6 ± 1.3	21.6 ± 2.8	19.8
Phosphatidylinositol	7.2 ± 0.2	3.9	6.6 ± 1.5	8.2 ± 1.5	6.5
Phosphatidylserine	3.2 ± 0.1	5.5	0.9 ± 1.3	3.9 ± 2.8	3.7
Phosphatidylcholine	50.8 ± 0.4	57.3	40.5 ± 2.9	58.7 ± 4.0	43.1
Sphingomyelin	4.2 ± 0.2	6.3	2.4 ± 0.9	4.0 ± 0.5	23.1
Lysophosphatidylcholine	1.4 ± 0.2	-	1.4 ± 0.3	2.0 ± 1.0	1.8
Cardiolipin	2.2 ± 0.3	-	14.8 ± 1.2	1.6 ± 1.3	-

3. Tail(s) consisting of hydrocarbon chains that are derivatives of fatty acids. They can be either saturated (all the carbon atoms in the chains are connected by single

²Source : <http://withfriendship.com/images/g/30850/Phospholipid-picture.jpg>

1. General Introduction

bonds) or mono- and poli- unsaturated (at least one double bond).

The lipid composition of membranes presented in Table 1.2 for various organelles shows again that the most common ones are phosphatidylcholines and phosphatidylethanolamines. The abundance of the first does not fall below 40% of the total weight of the membrane for all the presented organelles and is the lowest for mitochondria, which exhibits on the other hand the highest concentration of cardiolipin and phosphatidylethanolamine. The latter is the second most abundant type of lipid, with the lowest abundance of 20% in a plasma membrane. According to these findings, phosphatidylethanolamine and in particular phosphatidylcholine are the basic lipids constituting biological membranes in cells. They stand for 51% of the total weight of all membranes in a tissue.

Table 1.3: Fatty acids composition in different animal species (weight percentage of the total) [A - Brockerhoff *et al.* [1966], B - Christie & Moore [1970], C - Brockerhoff & Hoyle [1963]].

FATTY ACID	SPECIES					
	Rat [A]	Horse [A]	Duck [A]	Pig [B]	Herring [C]	Seal [C]
16 : 0	23	26	21	29	21	10
16 : 1	5	8	6	3	11	16
18 : 0	6	5	6	18	-	-
18 : 1	35	31	49	41	23	26
18 : 2	19	9	16	8	1	2
18 : 3	2	18	2	-	-	-
20 : 1	-	-	-	-	10	14
20 : 5	-	-	-	-	9	7
22 : 1	-	-	-	-	10	7
22 : 6	-	-	-	-	5	8

The comparison above referred only to the properties of the headgroup moieties. The other differences concern the lengths of the hydrocarbon chains (tails) and their level of

1. General Introduction

saturation (number of double bonds). In Table 1.3 the content of diverse fatty acid tails is presented for six animal species: rat, pig, duck, horse, herring and seal. The nomenclature in the first column should be read as - the total number of carbon atoms in a chain : number of double bonds (“20 : 1” means for example a tail consisting of twenty carbon atoms with one double bond). As one can easily see, the most abundant tails are the saturated palmitoleic fatty acid rests (sixteen carbon atoms) and oleic acid rests with one double bond (eighteen carbon atoms). This result suggests that the most common lipid would be a phosphocholine with palmitoleic and oleic tails, which would be a 1-palmitoyl-2-oleoyl-sn-glycero-3-phosphocholine (POPC). An interesting observation is that higher order lipids with the unsaturated hydrocarbon chains of twenty and more carbon atoms are found only in aquatic animals leaving in cold environment, here herring and seal.

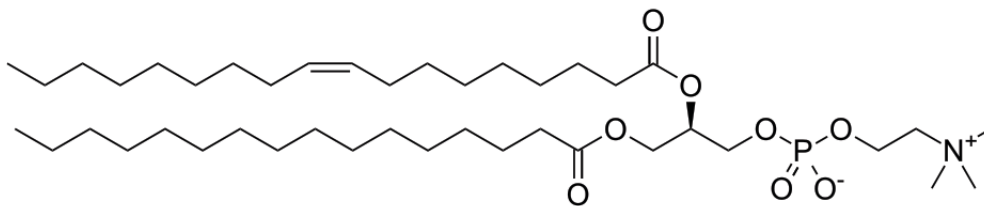


Figure 1.3: Sketch of the POPC chemical structure ³.

The surface area of a membrane is huge in comparison to macromolecules, so the probability of finding a specific membrane protein is low. Many processes in cells involve several proteins, and for that reason macromolecules taking part in the same reaction must stay localized and close to each other in biological membranes [Berg *et al.* [2005]]. To raise the probability of finding the necessary proteins in the reaction volume, nature developed several strategies. One of them is a confinement of proteins within physical barriers, which are formed by the cytoskeleton attached to the membrane. Another strat-

³Source : <http://en.wikipedia.org/wiki/File:1-palmitoyl-2-oleoylphosphatidylcholine.svg>

egy, more interesting from the perspective of this work, is to slow down the diffusion of the lipids and proteins, keeping them more localized in the bilayer. In this case, there is no need for physical barriers, since the very nature of the diffusion of molecules would already raise the probability of keeping them in the same place. One of the examples is the self-organization of lipids into domains (so-called rafts), which seem to attract proteins [Risselada & Marrink [2008]; Silva *et al.* [2007]]. These proteins diffuse with the lipids in the raft.

1.2 Transport of molecules in cells and membranes

The diffusion of molecules observed in living cells deviates in many cases from normal diffusion (the definition and its generalization is described in more details in the next section), where normality is defined by Einstein's diffusion law [Einstein [1905]], which predicts that the mean square displacement of the diffusing particle grows linearly with time. In biological membranes one observes instead an anomalous sublinear growth.

Anomalous diffusion has been observed in cells by various spectroscopic experimental methods. Cells, including biological membranes, are crowded with a huge number of different organelles and particles, as proteins, lipids, DNA, RNA and many more [Berg *et al.* [2005]]. Moreover, organelles are also internally crowded with diverse molecules. Very useful methods to study diffusion in such crowded systems are fluorescence-based techniques, such as the fluorescence correlation spectroscopy (FCS) and single particle tracking methods (SPT). The former measures the concentration fluctuations of fluorescent particles and the latter, the movements of a single fluorescent particle [Bronstein *et al.* [2009]; Owen *et al.* [2009]; Schwille *et al.* [1999b]].

SPT revealed for example that chromosomal loci in bacteria are moving subdiffusively

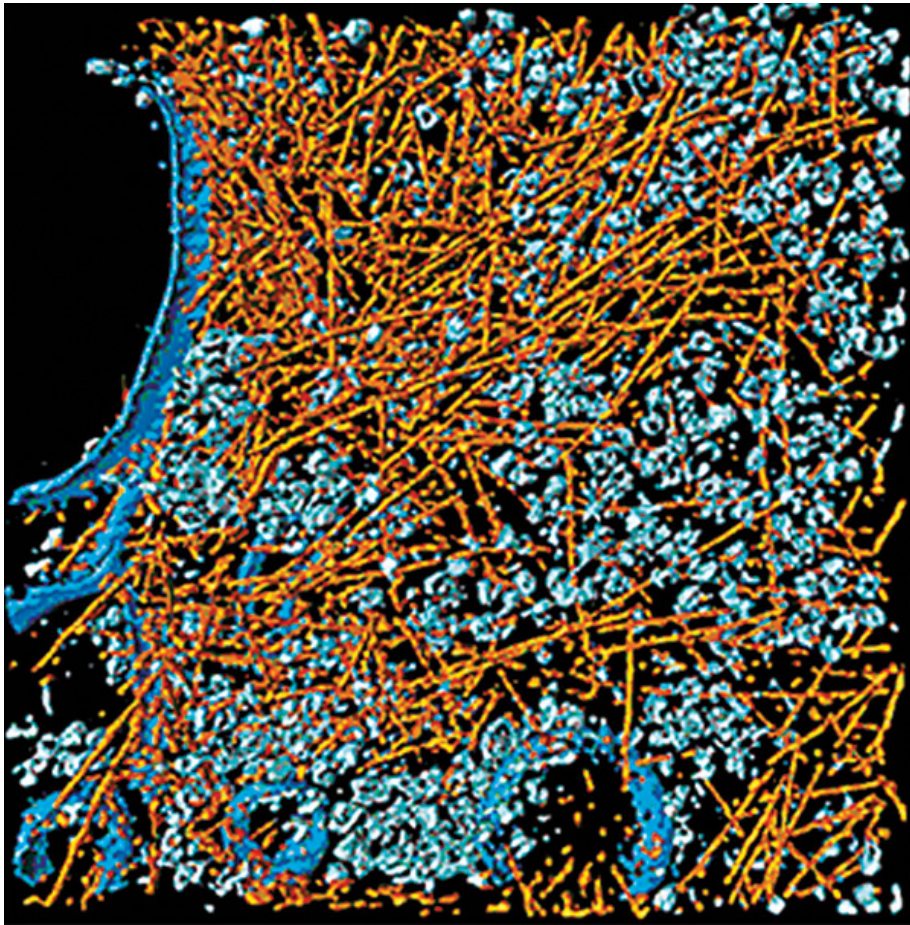


Figure 1.4: Crowded cell compartments visualized by cryoelectron microscopy⁴ Actin filaments are shown in orange, ribosomes and other macromolecular assemblies in grey, and membrane structures in blue.

through the cytosole[Weber *et al.* [2010]]. This finding is significant for the dynamical organization chromosomes, in particular for a possible contribution to the preservation of the chromosomal territories during the segregation process. Further results from different studies on chromosomal movements, which have been obtained again with SPT, show that the telomeres in eucaryotic nucleus stay localized and their movements exhibit a transient subdiffusion [Bronstein *et al.* [2009]]. This could explain the strong conservation

⁴Source : http://www.nature.com/embor/journal/v5/n1/fig_tab/7400056_F3.html

of the genome organization. From a general point of view of chromosomal transport

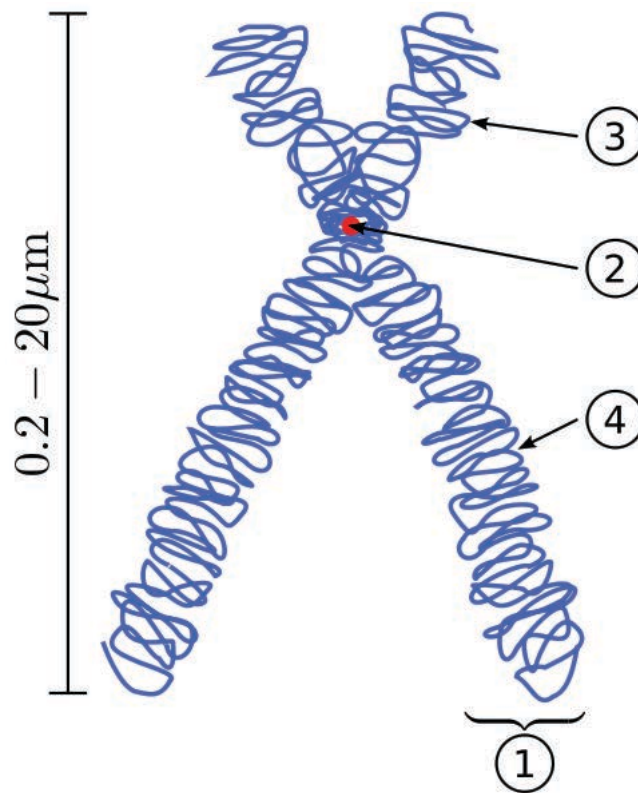


Figure 1.5: Illustration of a chromosome ⁵, depicting its parts; the endings of each of the four arms(3,4), called telomeres (1) and the centromere (2) connecting the two chromatides.

within nuclei, subdiffusion also leads to a preservation of the position without physical constraints.

Fluorescence Correlation Spectroscopy (FCS) studies of the diffusion of the DNA-binding protein LacI (lac repressor) show that this protein diffuses normally between bindings [Elf *et al.* [2007]]. This would suggest that most of the time the lacI protein is diffusing freely along DNA strands and is non-specifically bound. The same conclusions can be drawn from other FCS and SPT measurements for different small molecules in

⁵Source : <http://en.wikipedia.org/wiki/File:Chromosome.svg>

1. General Introduction

cells, whose diffusion constants are several times smaller in denser media, like cytoplasm (in comparison to water solution), but diffuse normally [Dix & Verkman [2008]].

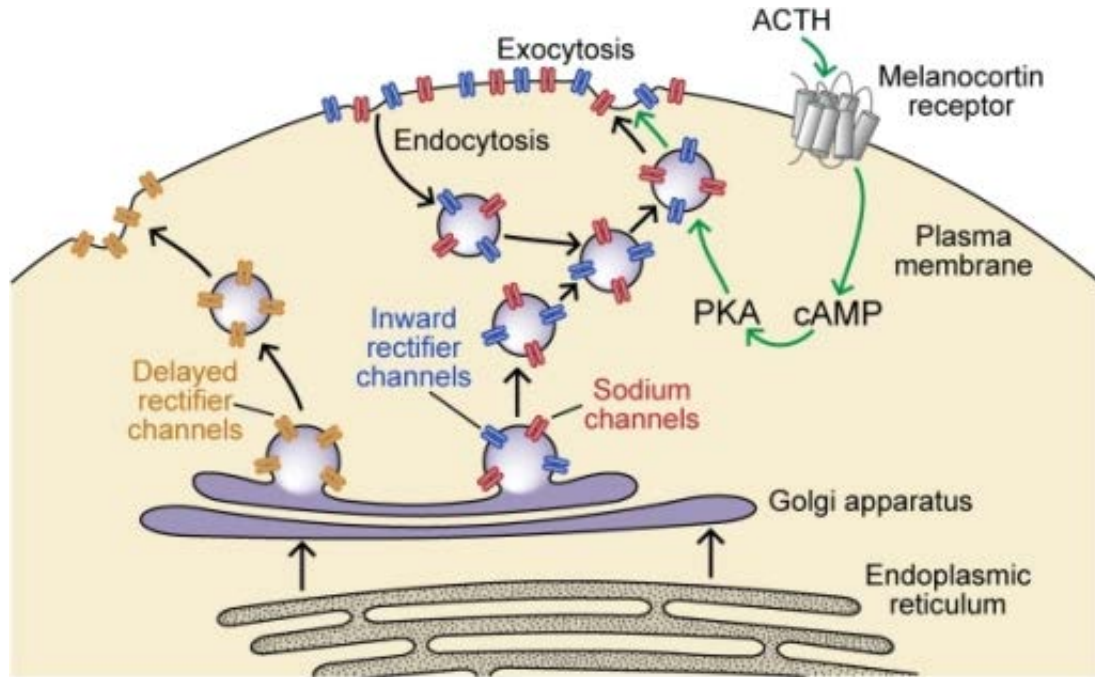


Figure 1.6: Visualization of ion trafficking in cells involving Golgi apparatus and rectifier potassium channels (inward and delayed)⁶. The ion channels are synthesized in endoplasmic reticulum and through Golgi are transported to the plasma membrane.

The aforementioned methods are also extensively used in studying the dynamics of molecules within biological membranes. The FCS studies of Schwille *et al.* [1999b] on living cells, revealed subdiffusive movements of dilauroyl-sn-glycero-3-phosphocholine lipids (DLPC) in the cell membrane. In contrast, the diffusion in lipid granules in yeast cells display transient anomalous diffusion for shorter times (SPT), but for longer times becomes normal [Jeon *et al.* [2012]]. A very similar observation has been published using quasi-elastic neutron scattering method (QENS) for the dimyristoyl-sn-glycero-3-phosphocholine (DMPC) in the fluid phase at the pico- to nano-second time scale [Armstrong *et al.* [2011]]. In the latter work the diffusion is found to be normal for larger inter-lipid distances, with

⁶Source : http://openi.nlm.nih.gov/detailedresult.php?img=2741594_pbio.1000203.g012&req=4

a value of diffusion coefficient consistent with other findings. But for smaller lipid-lipid lateral distances (0.23 nm) the nature of the movements are ballistic (motions without collisions with other molecules). Other QENS results show that phospholipids might diffuse together with their neighbors [Busch *et al.* [2010]]. This experiment of pico- to nano-second time scale suggests a dynamical clustering of lipids moving together in plane of a membrane.

As biological bilayers are vivid mosaics containing not only lipids but also proteins, the scope of experimentalists also focused on the diffusion of the latter. FCS studies of the Golgi resident membrane proteins [Weiss *et al.* [2003]] tracked the subdiffusion of these molecules in the endoplasmic reticulum. Other findings using SPT on potassium membrane channels, imply anomalous diffusion of these proteins [Weigel *et al.* [2011]]. Movements which are supposedly affected by the actin cytoskeleton network.

1.3 Modeling anomalous diffusion

In 1855 Adolf Fick published one of the first theoretical papers on diffusion, which was inspired by Fourier's work on heat transfer. The basic assumption in his work is that the direction of the diffusive flux, J , is from higher to lower concentrations of a substance [Fick [1855]],

$$J(\mathbf{x}, t) = -D\nabla C(\mathbf{x}, t), \quad (1.1)$$

where D is the diffusion coefficient. Expressing the conservation of the total number of particles in form of an equation of continuity, $\partial_t C(\mathbf{x}, t) + \nabla \cdot J(\mathbf{x}, t) = 0$, it follows then that $C(\mathbf{x}, t)$ fulfills the well-known diffusion equation,

$$\frac{\partial}{\partial t} C(\mathbf{x}, t) = D\Delta C(\mathbf{x}, t). \quad (1.2)$$

1. General Introduction

The solution of Eq. (1.2) is a Gaussian function. Later Einstein has given a probabilistic interpretation for Fick's model, in which he has shown that this Gaussian function is the mean squared displacement of the diffusing particles [Einstein [1905]]:

$$W(t) = \langle (\mathbf{x}(t) - \mathbf{x}(0))^2 \rangle = 2Dt. \quad (1.3)$$

Here \mathbf{x} is the position of the particle, D is the diffusion constant and $\langle \dots \rangle$ is an average over all realizations of a random walk. Experimental illustrations of Brownian movements were published by Jean Baptiste Perrin [1909], where he recorded the random walk trajectories of putty grains and reconstructed the Gaussian solution of the diffusion equation by histograms (Fig. 1.7).

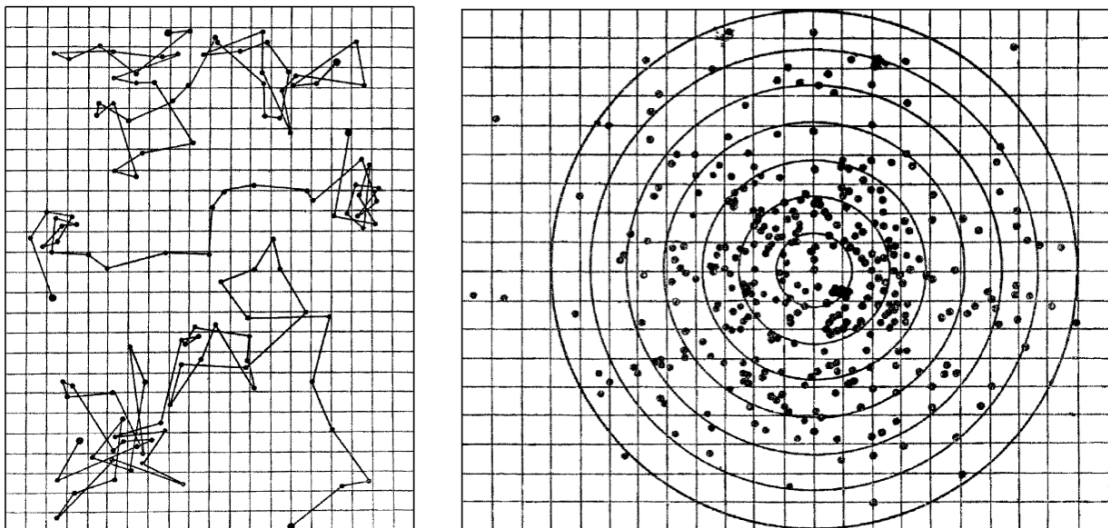


Figure 1.7: Recorded diffusion of putty grains published by Perrin [1909].

Reported exceptions from normal diffusion have been reported quite early [Blair [1943]; Freundlich & Kruger [1935]; Herzog & Kruger [1929]; Long *et al.* [1953]] and one of the manifestations is that the mean square displacement deviates from the linear form,

Eq. (1.3),

$$W(t) = 2D_\alpha t^\alpha, \quad 0 < \alpha < 2, \quad (1.4)$$

where the diffusion coefficient D is replaced by its fractional counterpart. The α parameter is defined in the range $\alpha \in (0, 2)$ and characterizes the type of diffusion. The regime $0 < \alpha < 1$ is typical for crowded systems and is called subdiffusion. For $1 < \alpha < 2$ we have superdiffusion, suggesting the presence of forces accelerating the motions of the particle under consideration.

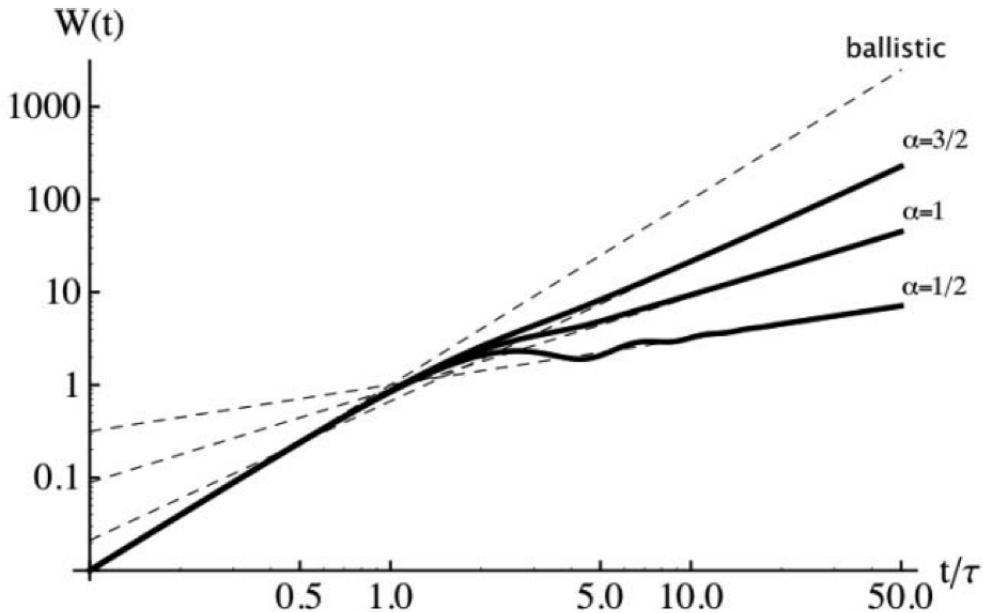


Figure 1.8: MSD of a model system for various values of α [Kneller [2011]].

Anomalous diffusion can be modelled by considering probability density functions of waiting times, ψ_t , and lengths of jumps, ψ_j , which is the base of the continuous time random walk model [Montroll & Scher [1973]; Montroll & Weiss [1965]; Shlesinger [1974]]. In case of subdiffusive processes, waiting times can be very long and the characteristic waiting time, $\int_0^\infty dt \psi_t(t)$, diverges. The corresponding diffusion equation has the form of a

fractional differential equation [Metzler & Klafter [2000]; Wyss [1986]]

$$\frac{\partial P(\mathbf{x}, t)}{\partial t} = {}_0\partial_t^{1-\alpha} D_\alpha \Delta P(\mathbf{x}, t), \quad (1.5)$$

where ${}_0\partial_t^{1-\alpha}$ denotes the fractional Riemann-Liouville derivative of order $(\alpha - 1)$ [Oldham & Spanier [2006]]. In general ${}_0\partial_t^{m-\beta} f(t) = d^m/dt^m \int_0^t \Gamma(\beta)^{-1} (t-t')^{\beta-1} f(t')$ is the fractional derivative of order $m - \beta$, where $m = 0, 1, 2$ and $\beta \geq 0$. The convolution expresses non-Markovian memory effects and for $\alpha = 1$ the normal diffusion equation is retrieved. In contrast to Eq. (1.2), $P(\mathbf{x}, t) \equiv P(\mathbf{x}, t | \mathbf{x}_0, t_0)$ is, however, the conditional transition probability of a stochastic process and not a concentration.

In the framework of the classical theory of liquids, the MSD can be expressed as [Boon & Yip [1991]]

$$W(t) = \langle (\mathbf{x}(t) - \mathbf{x}(0))^2 \rangle = 2 \int_0^t dt' (t-t') C_{vv}(t'), \quad (1.6)$$

where $C_{vv} = \langle \mathbf{v}(t) \cdot \mathbf{v}(0) \rangle$ is the velocity autocorrelation function of the diffusing particle. As shown in Fig. 1.8, the MSD exhibits for short times a so-called ballistic behavior, $W(t) = \langle |\mathbf{v}|^2 \rangle t^2$, which corresponds to movements without any collisions. For long times, the asymptotic forms of the MSDs show either normal diffusion, subdiffusion or superdiffusion [Kneller [2011]]. Equation (1.4) is true only in asymptotic regime for $t \rightarrow \infty$,

$$W(t) \stackrel{t \rightarrow \infty}{\sim} 2D_\alpha t^\alpha, \quad 0 < \alpha < 2. \quad (1.7)$$

1.4 Recent simulation work

Molecular dynamics simulation is a numerical method allowing to simulate the dynamics of complex liquids and solids at atomic resolution [Allen & Tildesley [1991]]. This computer technique gives access to a very detailed picture of the dynamics of molecular systems on pico- to nano-seconds scale. Despite the limitations of the accessible time scale, molecular

dynamics simulations provide deep insights.

In studies of biological membranes, molecular dynamics simulations are widely used and some simulations show contradictory findings concerning the dynamics of lipids within the membranes. In the work of [Kneller *et al.* \[2011\]](#) it was for example shown that the MSD for the lateral diffusion of lipid molecules in a dioleoyl-sn-glycero-3-phosphocholine (DOPC) membrane exhibits a subdiffusive form with $\alpha \approx 0.5$. Similar findings have been published for the dynamics in lipid bilayers [[Arnold *et al.* \[2004\]](#); [Ritchie *et al.* \[2005\]](#)] Other molecular dynamics simulation results reveal subdiffusive motions of the

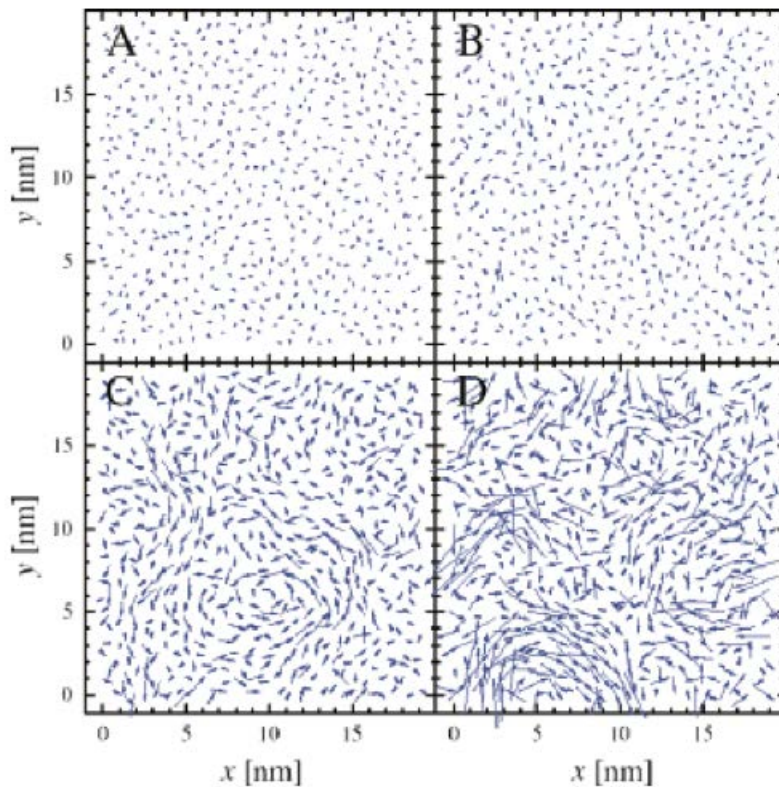


Figure 1.9: Plot representing the displacements of the DPPC lipids in x and y planes for the upper leaflet (a,b,c) and lower leaflet (d); (a) shows a 50 ps interval from 5.00 to 5.05 ns of the simulation, (b) a 500 ps interval from 5.0 to 5.5 ns, (c) a 5 ns interval from 5 to 10 ns, and (d) a 30 ns interval from 10 to 40 ns [[Falck *et al.* \[2008\]](#)].

DOPC, DSPC (distearoyl-sn-glycero-3- phosphocholine) and SOPC (1-stearoyl-2-oleoyl-sn-glycero-3- phosphocholine) lipids in mixtures with cholesterol [Jeon *et al.* [2012]]. On the other hand, extensive simulations of DMPC by Flenner *et al.* [2009] and Goose & Sansom [2013] show three regimes of lipids diffusion in the bilayer, suggesting that subdiffusion is a transient phenomenon. There are, moreover, some interesting findings of the collective motions of the lipids [Falck *et al.* [2008]]. The simulations, which were performed for DPPC systems of different sizes (from 128 to 4608 lipids), showed collective "flow-like" patterns of moving molecules strongly correlated over tens of nanometers. This suggests that neighboring molecules diffuse together, keeping their relative distances for long times.

The goal of this thesis is to elucidate this interplay of subdiffusion and the persistence of local "cages" formed by neighboring lipids.

Chapter 2

Concept of Molecular Dynamics

Simulations

Molecular dynamics (MD) is a computational method to study the structure and dynamics of liquids, which was introduced by Alder and Wainwright [Alder & Wainwright [1957]].

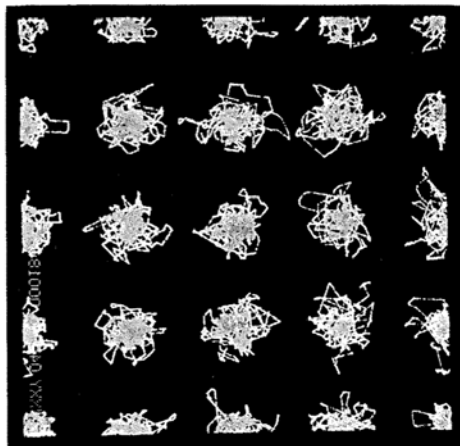


Figure 2.1: Results of one of the first molecular dynamics simulation published by Alder [Alder & Wainwright [1957, 1959]] - the figure shows traces of the simulated hard sphere particles for about 3000 collisions.

Following works of Alder and Wainwright, Rahman proposed in 1964 a realistic continuous potential for the system of liquid argon [Rahman [1964]], and performed a simulation for 864 argon molecules in a cubic box, which is considered the first classical MD simulation. Further works of Rahman, with Stilling, resulted in realistic simulations of liquid water [Stillinger [1974]]. Three years later the MD method advanced another step with the first simulation of a protein, bovine pancreatic trypsin inhibitor (BPTI), which was performed by McCammon *et al.* [1977].

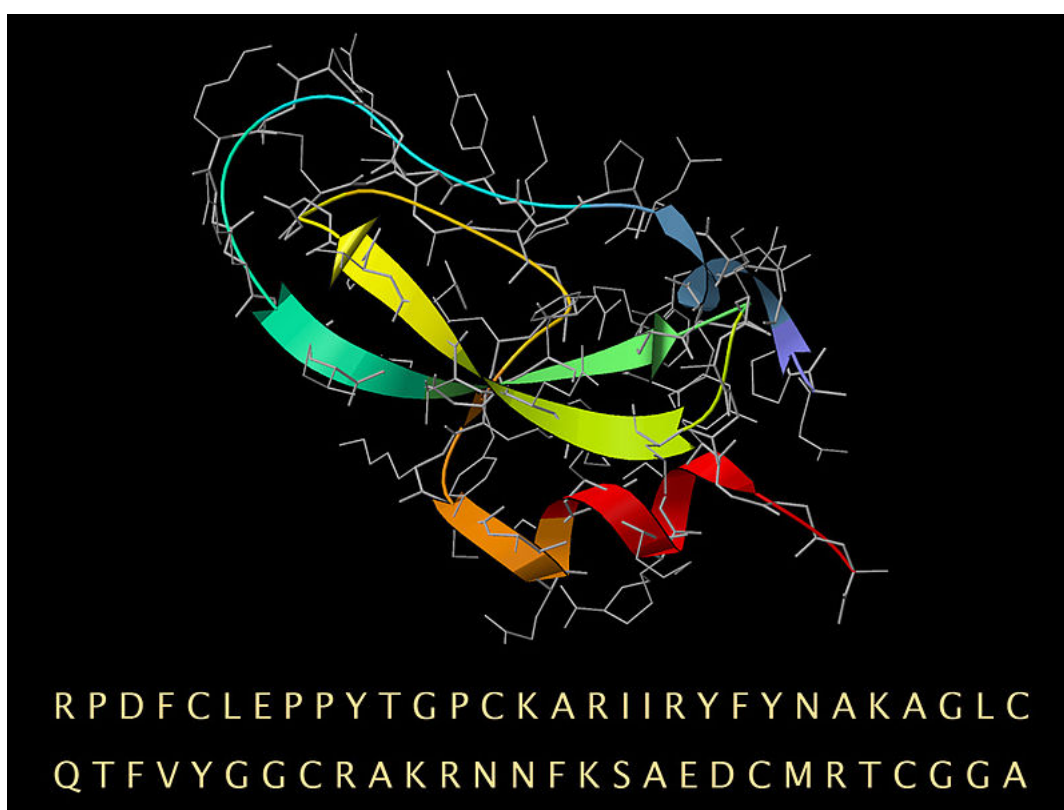


Figure 2.2: Structure of the first simulated protein - bovine pancreatic trypsin inhibitor (BPTI)¹⁰. On the bottom of the figure is written full amino acid sequence of this protein.

Since then, computer technology progressed enormously and allows today to simulate

¹⁰Source : http://en.wikipedia.org/wiki/File:BPTI_seq_ribbon_sticks.jpg

such diverse biological systems as DNA-protein complexes or lipid membranes by MD. One can in particular address biological relevant problems as protein folding and ligand binding.

2.1 Classical Molecular Dynamics Simulations

2.1.1 Concept and potential function

Molecular dynamics simulations are conducted by solving Newton's equations of motion for a system of N atoms on a discrete time scale,

$$m_i \frac{d^2 \mathbf{r}_i}{dt^2} = \mathbf{F}_i, \quad i = 1, 2, \dots, N. \quad (2.1)$$

Here \mathbf{F}_i is the acting force on the i -th atom, where m_i is its mass. The force is computed as the negative gradient of the potential energy $V(\mathbf{r}_1, \mathbf{r}_2, \dots, \mathbf{r}_N)$,

$$\mathbf{F}_i = -\frac{\partial V_i}{\partial \mathbf{r}_i} \quad (2.2)$$

The potential energy describes all interactions in the simulated system, which are treated in terms of classical mechanics. The equations of motions are solved for the atoms in the system and the electrons are not considered explicitly. The dynamics of electrons being much faster than one of the atomic nuclei, so one can consider that the movements of electrons instantly adjust to the movements of atom. This is the Born-Oppenheimer approximation. Moreover electrons are implicitly always in the ground states, so MD can not model processes of electron transfers or systems with electrons in excited states. It is one of the reasons why it is not possible to treat properly chemical reactions in classical MD. This is also true for all the quantum effects that can appear in the system, e.g. tunneling of protons or existence of noncovalent intermediates. Such phenomena cannot be

simulated by classical molecular dynamics simulations. Despite these limitations, classical MD simulations have proven to be very successful in reproducing experimental results and in predicting new properties of the systems under consideration.

The potential energy describes so-called bonded and non-bonded interactions,

$$V(\mathbf{r}_1, \mathbf{r}_2, \dots, \mathbf{r}_N) = \sum_{\text{bonds}} K_b (b - b_0)^2 \quad (2.3)$$

$$+ \sum_{\text{angles}} K_\theta (\theta - \theta_0)^2 \quad (2.4)$$

$$+ \sum_{\text{dihedrals}} \frac{V_n}{2} (1 + \cos(n\psi - \psi_0)) \quad (2.5)$$

$$+ \sum_{i < j} \frac{A}{r_{ij}^{12}} - \frac{B}{r_{ij}^6} \quad (2.6)$$

$$+ \sum_{i < j} \frac{q_i q_j}{\epsilon r_{ij}}. \quad (2.7)$$

Bonded interactions result from covalent bonds between atoms and include bond-stretchings with a harmonic force with force constant K_b around the equilibrium bond length, b_0 (2.3), harmonic bending of valence angles (2.4) with harmonic constants K_θ , and displacements of dihedral angles (2.5). Here V_n is the height of the energy barrier and n -th number of minima in the range $(0, 2\pi)$. Non-bonded interactions include van der Waals (short-range) and Coulomb interactions (long-range), which depend on the relative distances r_{ij} between interacting atoms. Van der Waals interactions describe repulsion between atoms due to volume exclusion, as well as dipole-induced attractions between atoms. These interactions are described by the Lennard-Jones function (2.6). The Coulomb term in the potential function 2.7, represents the electrostatic interactions between atom charges q_i and q_j , and ϵ is the permittivity constant for the medium in which the charges are embedded.

The values for the aforementioned physical quantities (e.g $K_b, b_0, \theta_0, q_i, \dots$) define the

force-field (ff). They are fitted to experimental data and/or quantum mechanical calculations. The calculation of the potential energy with all-atom force-fields is very time-consuming, since the computational effort for the two-body interactions between free N -particles (not bonded covalently) grows as N^2 . One of the approaches to reduce the computational effort is therefore to reduce the number of interaction centres. Three categories of force-fields are used today: all-atom (AA), united atom (UA) and coarse-grained (CG) ffs. The UA and CG ffs group several atoms into one particle. In the united atom model, one particle describes one heavy carbon atom with all aliphatic hydrogen atoms bound to it. In coarse-grained force-fields, several heavy atoms (with all hydrogen atoms bound to them) are represented as one interaction center, a so-called “bead”, allowing for simulations on much larger time and length scales.

As already mentioned, Newton’s equations of motion are numerically solved by a discretization scheme. One of these schemes is the leap-frog algorithm. This integrator uses the positions \mathbf{r}_i at time t and velocities \mathbf{v}_i at $t - \frac{1}{2}\Delta t$ to calculate the positions at time $t + \Delta t$ [Frenkel & Smit [2002]] :

$$\mathbf{v}_i(t + \frac{1}{2}\Delta t) = \mathbf{v}_i(t - \frac{1}{2}\Delta t) + \frac{\Delta t}{m_i}\mathbf{F}_i(t), \quad (2.8)$$

$$\mathbf{r}_i(t + \Delta t) = \mathbf{r}_i(t) + \Delta t \mathbf{v}_i(t + \frac{1}{2}\Delta t). \quad (2.9)$$

The new coordinates at $t + \Delta t$ are calculated after a *leap* over velocities at $t + \frac{1}{2}\Delta t$ (therefore the name *leap-frog*). The algorithm is robust and time-reversible, and the integration error is of order 3 in Δt . The total energy can, however, not be calculated directly at a given time step, as the potential and kinetic energies are not computed at the same time. For this reason the the so-called Velocity-Verlet algorithm has been proposed. As the Leap-Frog integrator, it integrates explicitly positions and velocities, but both are

available at the same time [Frenkel & Smit [2002]] :

$$\mathbf{r}_i(t + \Delta t) = \mathbf{r}_i(t) + \Delta t \mathbf{v}_i(t) + \frac{\Delta t^2}{2m_i} \mathbf{F}_i(t), \quad (2.10)$$

$$\mathbf{v}_i(t + \Delta t) = \mathbf{v}_i(t) + \frac{\Delta t}{2m_i} (\mathbf{F}_i(t + \Delta t) + \mathbf{F}_i(t)). \quad (2.11)$$

In both algorithms the explicit integration of velocities can be used to simulate systems in contact with an external heat bath, which requires the scaling of the velocities.

2.1.2 Periodic boundary conditions and treatment of electrostatic interactions

Molecular systems in MD simulations are many orders of magnitude smaller than macroscopic systems studied by experimental methods. A direct simulation would produce unwanted artefacts, especially at the edges of the simulated systems. In order to avoid such artefacts, one can apply periodic boundary conditions (PBC).

This means an infinite replication of the simulation box in all the directions. Assuming a cubic simulation box, the images of the i -th atom have the positions

$$\mathbf{r}'_i = \mathbf{r}_i + \mathbf{n}L = (x_i + n_x L, y_i + n_y L, z_i + n_z L) \quad (2.12)$$

where L is the dimension of the box and $\mathbf{n} = (n_x, n_y, n_z)$, with $n_{x,y,z} \in \mathbb{N}$. An illustration is given in Fig. 2.3. During MD simulations the use of PBC just means that molecules can leave the box and enter it on the opposite side. To avoid jumps in the forces the minimum image convention is used; interactions are computed for the closest site (either a "real" atom or its image). This convention implies also use of a cut-off radius for the short-range interactions, which is generally defined as half the length of the shortest linear box dimension ($r_{cutoff} \leq L$). This approach is, however, not correct for the long-ranged Coulomb interactions, which exceed the box dimensions. Here the simulated system is

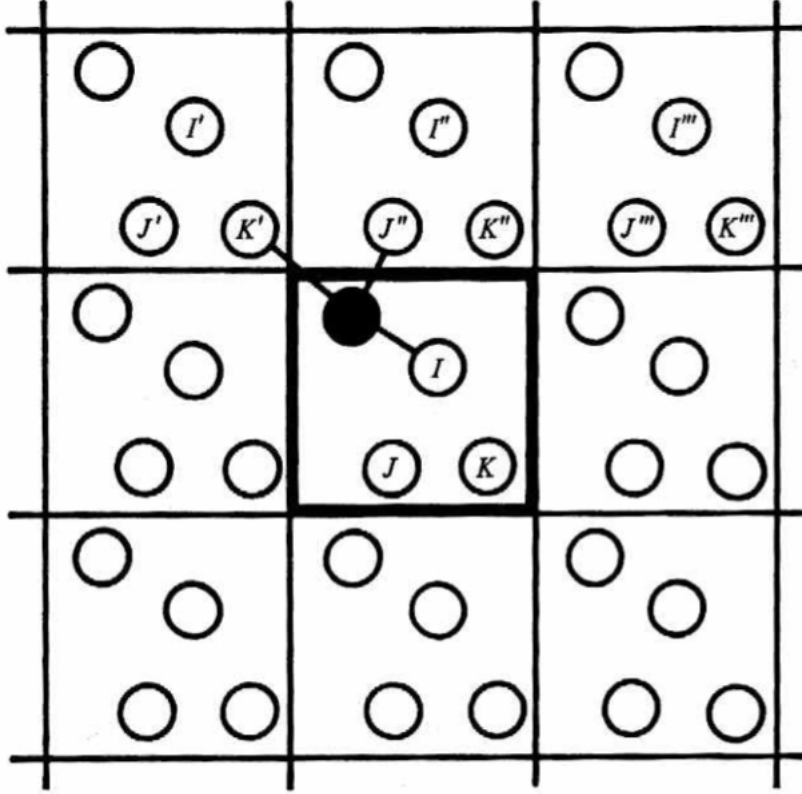


Figure 2.3: Illustration of the periodic boundary conditions (PBC) method with the minimum image convention. The box in the middle is replicated in all directions and the non-bonded interactions are calculated only for the closest atoms or their images.

treated as a pseudo-crystal, using the Ewald summation to compute the electrostatic energy and forces.

The Coulomb energy of a system with periodic boundary conditions reads [Frenkel & Smit [2002]]

$$V_{\text{electrostatic}}(\mathbf{r}_i) = \sum'_{|\mathbf{n}|=0} \sum_{i=1}^N \sum_{j=1}^N \frac{q_i q_j}{|\mathbf{r}_{ij} + \mathbf{n}L|}. \quad (2.13)$$

The series above does not include the interactions between identical atoms in the central box ($|\mathbf{n}| = 0$) which is indicated by the prime on the first sum. Series (2.13) does not

converge and depends on the order of summation. The most common choice is spherical shell summation, which means summation over the lattice of simulation cells within a finite radius $R \gg L$, taking the limit $R \rightarrow \infty$. Since the system under consideration is periodic, the electrostatic potential and the charge distribution are written as Fourier series. The Fourier series for the charge distribution is split into a component which is made convergent by a spherical Gaussian damping factor and the complement which is evaluated in real space [Ballenegger [2014]; Ewald [1921]]. An efficiency gain for the computation of the first component can be obtained by evaluating charge distribution on a mesh (grid) and computing its Fourier transform by the Fast Fourier Transform algorithm (FFT). This is the so-called particle-mesh Ewald (PME) summation [Darden *et al.* [1993]; Deserno & Holm [1998]].

2.2 Treatment of thermodynamic conditions

With the conventional molecular dynamics method systems are simulated in microcanonical conditions (NVE ensemble), i.e. with a constant number of atoms, N , a constant volume, V , and a constant total energy E . Most processes in nature happen, however, in conditions where the temperature, T , and/or pressure, p , are constant. More realistic for simulating biological systems is the canonical ensemble, where the total number of particles, the volume and the average temperature are kept constant ($N, V, T = const$), or the isothermal-isobaric ensemble ($N, p, T = const$), where the total number of particles, the average pressure and the average temperature are fixed ($N, p, T = const$).

In order to perform molecular dynamics simulations of a system in the NpT ensemble, Andersen and Nosé introduced the extended system method [Andersen [1980]; Hoover [1985]; Nosé [1984]]. In this approach scaling variables are introduced, which are additional degrees of freedom of the dynamical system and which represent, respectively, the thermostat and the barostat. By scaling the positions and the velocities of the system

with these these additional variables, one can obtain the desired ensemble. The equations of motions for the isothermal-isobaric ensemble read

$$\dot{\mathbf{r}}_i = \frac{\dot{V}}{3V} \mathbf{r}_i + \frac{\mathbf{p}_i}{m_i}, \quad (2.14)$$

$$\dot{\mathbf{p}}_i = \mathbf{F}_i - \frac{\dot{V}}{3V} \mathbf{p}_i - \xi \mathbf{p}_i, \quad (2.15)$$

$$\dot{V} = \frac{p_V}{W_V}, \quad (2.16)$$

$$\dot{p}_V = \frac{1}{3V} \left\{ \sum_{i=1}^N \frac{\mathbf{p}_i^2}{m_i} - \sum_{i=1}^N \mathbf{r}_i \cdot \mathbf{F}_i \right\} - p - \xi p_V, \quad (2.17)$$

$$\dot{\xi} = \frac{1}{W_S} \left\{ \sum_{i=1}^N \frac{\mathbf{p}_i^2}{m_i} + \frac{p_V^2}{2W_V} - (3N + 1)k_B T \right\}. \quad (2.18)$$

Here \mathbf{r}_i are the atomic positions, \mathbf{p}_i the associated momenta, m_i is the mass of atom i , and V is the (fluctuating) volume of the simulation box. The variable ξ plays the role of a “friction constant”, which can, however, take positive and negative values. The constants W_S and W_V are pseudo masses describing the inertia of the thermostat and barostat, respectively, which determine the reaction time of the system to adapt to the imposed values of pressure and temperature. As usual, k_B denotes the Boltzmann constant.

Another method to regulate the temperature and pressure in the simulated system is the Berendsen coupling scheme [Berendsen & Postma [1984]]. The algorithm imposes corrections to deviations from the reference temperature or/and pressure at each step of the simulation. The Berendsen method is very robust, but does not correspond to the usual thermodynamic NVT or NpT ensembles.

An generalization of the extended system method, which allows for pressure control in *anisotropic* systems, was proposed by Parrinello and Rahman [Parrinello [1981]]. Here the components of the stress tensor instead of the (scalar) pressure are adjusted to desired values.

Chapter 3

Simulated systems and simulations

3.1 System setup

In this thesis two types of force-fields were used for molecular dynamics simulations of POPC bilayers - the all-atom Optimized Potentials for Liquid Simulations (OPLS) [Jorgensen & Tirado-Rives [1988]; Jorgensen *et al.* [1996]] and the coarse-grained MARTINI force field [Marrink *et al.* [2004, 2007]]. The longest production run using the OPLS-AA ff was of 150 ns, given the limitations of computer power. In order to attain longer time scales and larger systems, additional simulations were performed with a coarse-grained model.

3.1.1 All-atom OPLS force-field

The OPLS-AA force-field was originally developed for the simulations of proteins in liquid solutions [Jorgensen & Tirado-Rives [1988]; Jorgensen *et al.* [1996]] and has been extended later for the simulation of macromolecules [Kony *et al.* [2002]; McDonald & Jorgensen [1998]; Takeuchi [2012]; Watkins & Jorgensen [2001]], including lipids [Pasenkiewicz-Gierula *et al.* [1999]; Róg *et al.* [2002]; Shinoda & Okazaki [2001]; Takaoka *et al.* [2000]].

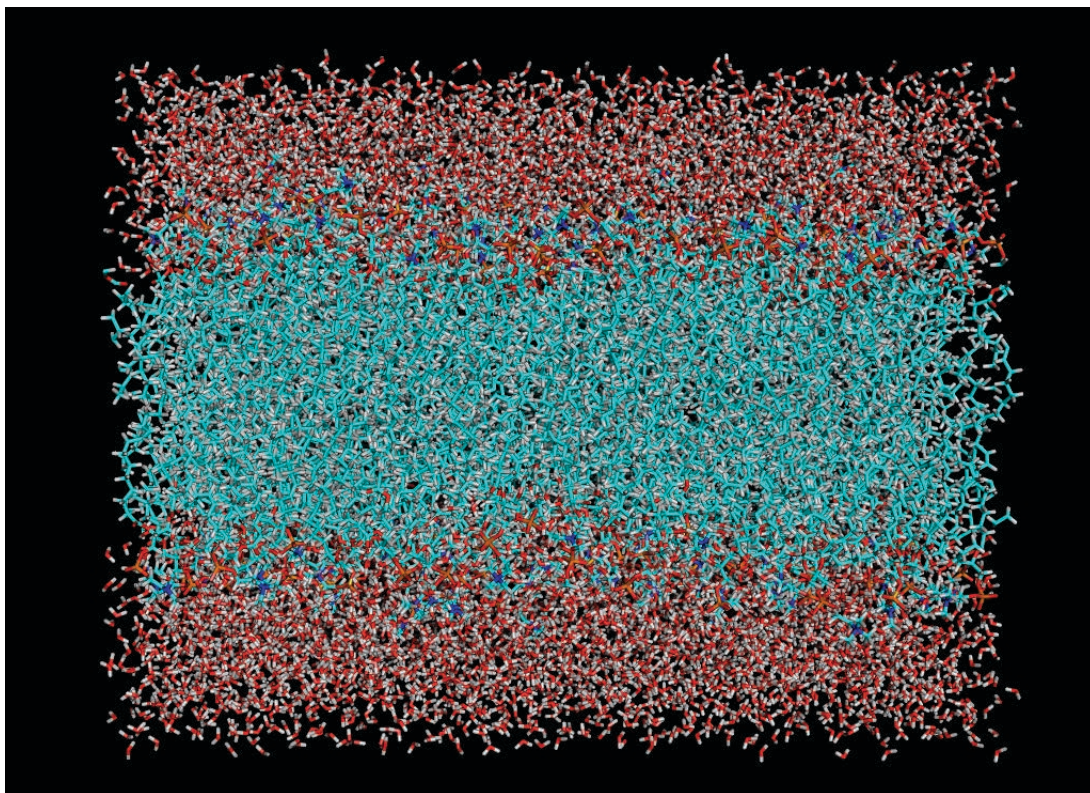


Figure 3.1: Simulated box of POPC all-atom model membrane. The system consists of total 274 lipids embedded in 10 471 water molecules.

The all-atom system consisted of 137 POPC lipids in each leaflet (274 lipids in total) and was built from POPC lipid patches provided by the VMD program [Humphrey *et al.* [1996]]. Thereafter it was fully hydrated with 10 471 water molecules using one of the tools from the GROMACS package [Hess *et al.* [2008]]. An average number of 38 water molecules per lipid is assumed to correspond to a fully hydrated POPC membrane (the expected value is of at least 27 water molecules per POPC molecule [Murzyn *et al.* [2001]; Nagle [1993]; Nagle *et al.* [1996]; Tristram-Nagle *et al.* [1998]]). The interactions of water were calculated with the SPC/E model, which assumes a rigid structure of the water molecules [Berendsen *et al.* [1987]]. The choice of the SPC/E force-field was motivated by the fact that it is one of the most commonly used models, which reproduces

well most properties of water and can be used in simulations with the OPLS-AA force-field [Hess & van der Vegt [2006]]. The final structure of the simulated system is shown in Fig. 3.1 [Stachura & Kneller [2013]].

3.1.2 Coarse-grained MARTINI force-field

The MARTINI force-field [Marrink *et al.* [2004, 2007]] was chosen for the extended simulations with a coarse-grained force-field. In this ff each molecule is built from beads, which represent each four heavy atoms with all hydrogen atoms bonded to them. Therefore one water bead equals four water molecules.

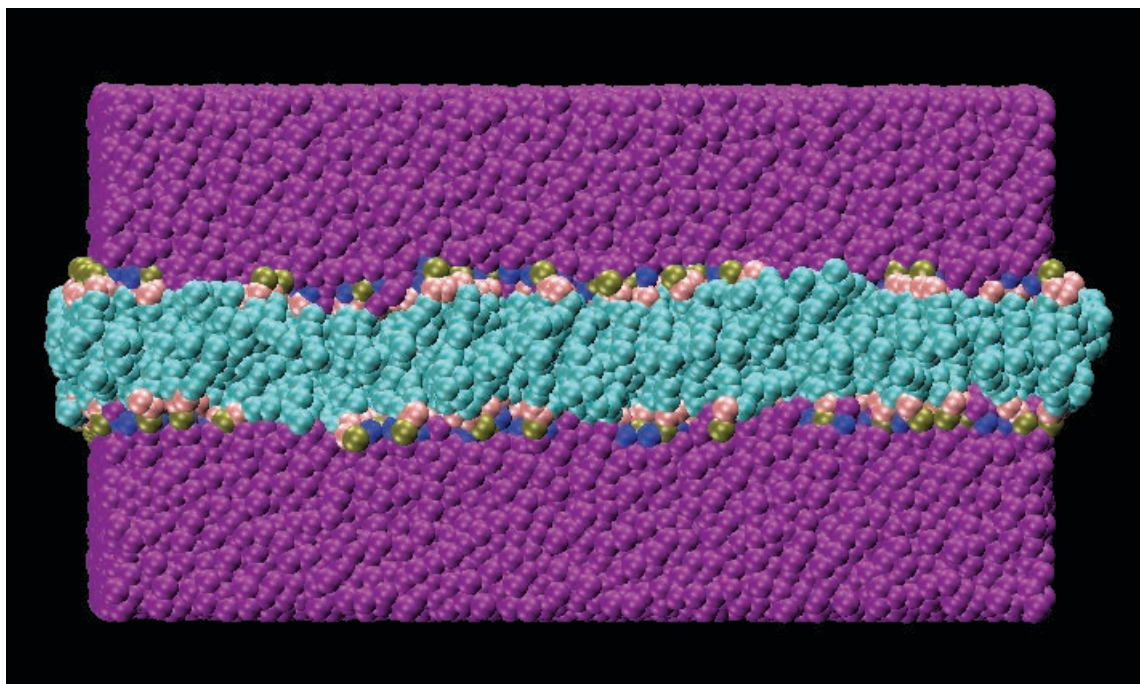


Figure 3.2: Simulated box of POPC coarse-grained model membrane. The system consists of 2033 lipids hydrated by 231 808 water molecules.

The POPC bilayer constructed for the simulations with the MARTINI ff consisted of 2033 lipids in total and was hydrated by 57 952 water beads, representing 231 808 wa-

ter molecules (Fig. 3.2) [Stachura & Kneller [2013]]. The starting structure was taken from Loeffler & Winn [2009].

In the MARTINI ff each POPC lipid molecule is built of 13 beads, and has a total mass $M_{CG} = 936 \text{ amu}$. The value is slightly higher than the real mass $M = 760.08 \text{ amu}$

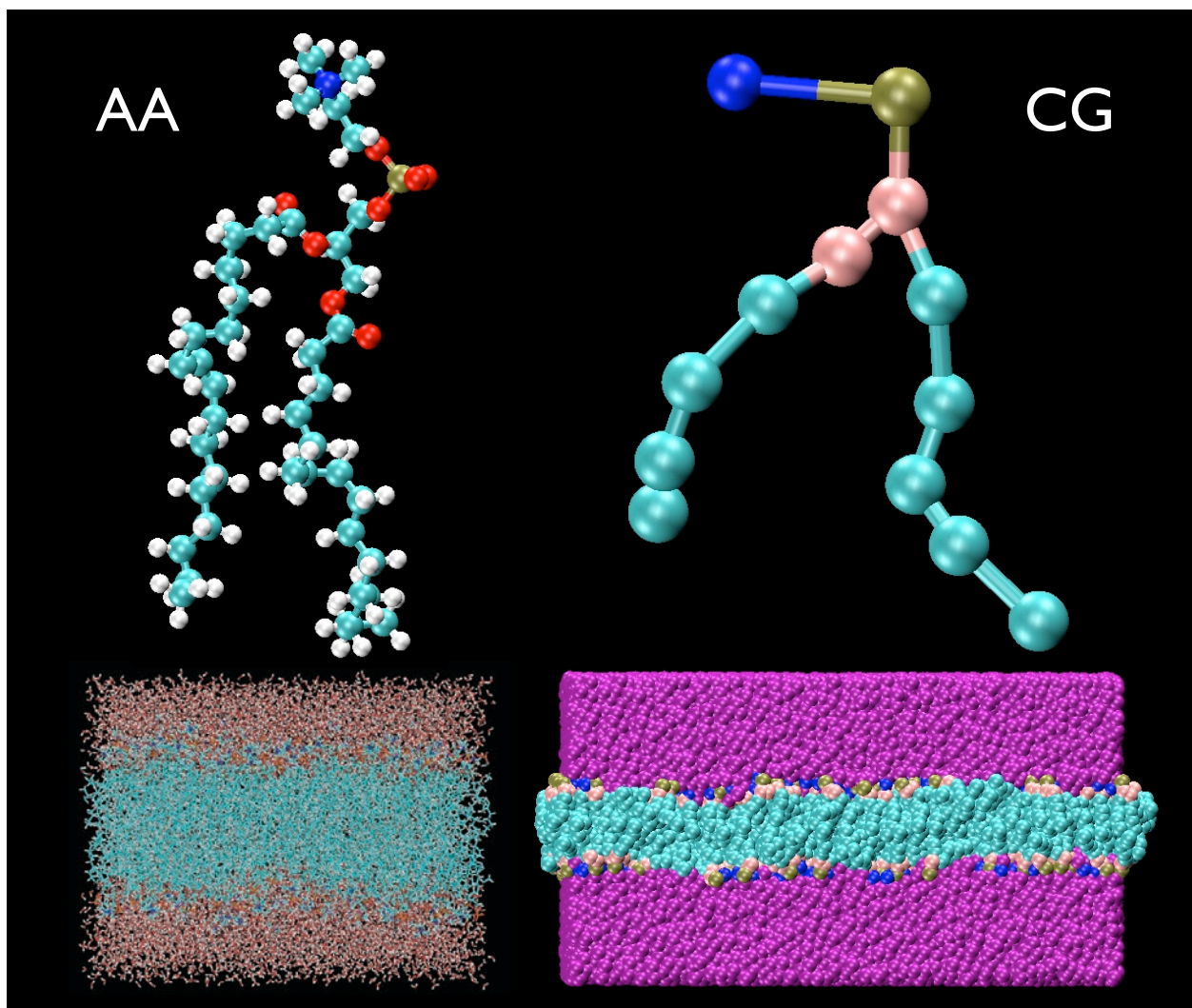


Figure 3.3: Comparison between all-atom and coarse-grained models of POPC membrane.

(amu means atomic mass units). To compensate for the higher masses the simulations were conducted at a temperature higher by 10 K compared to the temperature for the

all-atom calculations [Stachura & Kneller [2013]]. The comparison between all-atom and coarse-grained models is presented in Fig. 3.3.

3.2 Membrane simulations

All simulations in this thesis were conducted with the GROMACS package [Hess *et al.* [2008]] and the resulting trajectories were analysed with the nMoldyn program [Hinsen *et al.* [2012]; Kneller *et al.* [1995]]. All simulated systems (MARTINI and OPLS-AA ffs) were energetically equilibrated, before the production runs. Equilibration does not only imply constant total energy but also stable box fluctuations and surface areas per POPC lipid, which should be close to experimental data on average. All the simulations were performed above the main phase transition temperature of POPC lipids (270 K), which means that bilayers were in liquid phase [Lewis *et al.* [1988]; Litman *et al.* [1991]].

3.2.1 OPLS-AA force-field

The integration time-step in the all-atom simulations was generally set to 1 fs. An exception was the very first stage of the system equilibration, where the time-step was 2 fs. All bonds involving hydrogen atoms were constrained using the LINCS algorithm [Hess *et al.* [1997]]. Periodic boundary conditions were applied in all three directions with the minimum image convention. The Coulomb interactions were treated using the Particle-Mesh Ewald method with a real cut-off radius, r_{cutoff} , of 1.2 nm. The same r_{cutoff} was chosen for the van der Waals interactions. During simulations a constant temperature of 310 K was preserved either by Nosé-Hoover or Berendsen thermal baths. Most of the calculations were performed in isothermal-isobaric conditions (NpT), at a constant pressure of 1.01325 bar (1 atm). The pressures perpendicular and parallel to the bilayer were adjusted independently. The force-field parameters, were chosen as in similar simulations of POPC bilayers with the OPLS-AA force-fields [Murzyn *et al.* [2001]; Róg *et al.* [2003]].

3.2.1.1 System equilibration

The equilibration of the system was performed according to the method proposed by Berger *et al.* [1997]. The process has several stages:

1. A short 100 ps simulation in the canonical ensemble. The starting structure being far from equilibrium, a constant temperature was adjusted with the Berendsen thermostat, using a relatively short relaxation constant of 90 fs. The initial velocities of the atoms were generated according to the Maxwell-Boltzmann distribution at a temperature of 310 K.
2. Afterwards the system was coupled for 10 ps to the Berendsen barostat at 1 atm applying the pressure semi-isotropically (adjusting the pressure independently in perpendicular and vertical directions to the membrane). The relaxation time constants were set to 50 fs and 20 fs for pressure and thermal baths, respectively.
3. In the last stage, much longer isothermal-isobaric (NpT) simulations were conducted, where the system was coupled to the Nosé-Hoover thermostat and the Parrinello-Rahman barostat with the time constants of 200 fs and 500 fs, respectively. Again a pressure of 1 atm was adjusted semi-isotropically.

The last part of the equilibration process was performed until the total energy and surface area per lipid attained stable fluctuations around the desired mean values. Three consecutive simulations were conducted - 50 ns, then 30 ns and lastly 150 ns (230 ns in total), before the system was considered to be in equilibrium.

3.2.1.2 Short production run - 15 ns

After the equilibration phase a 15 ns production simulation was performed for further analyses. The total energy of the POPC membrane does not show any signs of decay - the energy fluctuations have the same amplitude around the mean value (Fig. 3.4). The

same can be said about the box fluctuations in the X, Y and Z directions (see Fig. 3.5a). The pressure applied during the simulation was treated isotropically in the XY-plane. The fluctuations in the X and Y directions are thus identical.

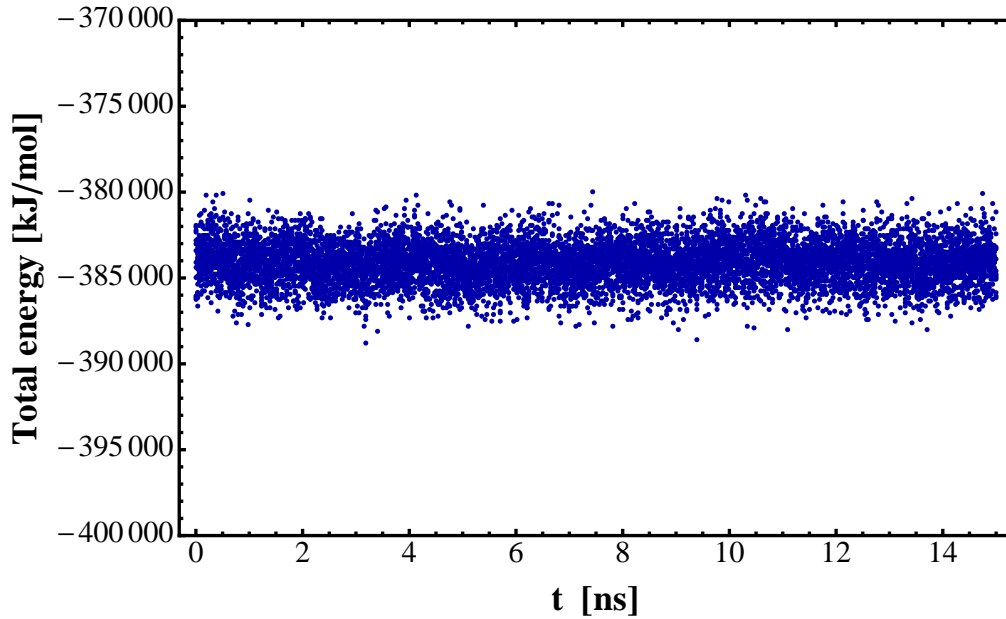
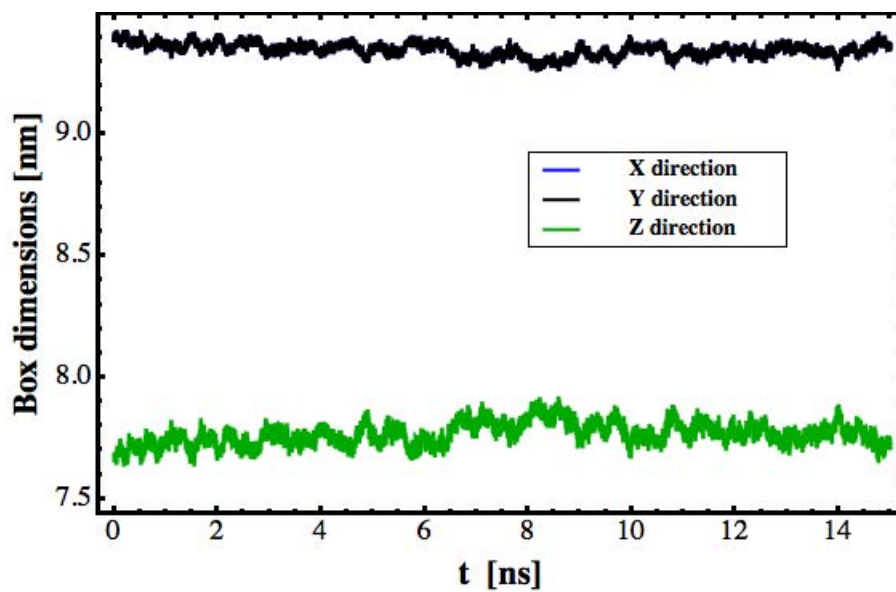
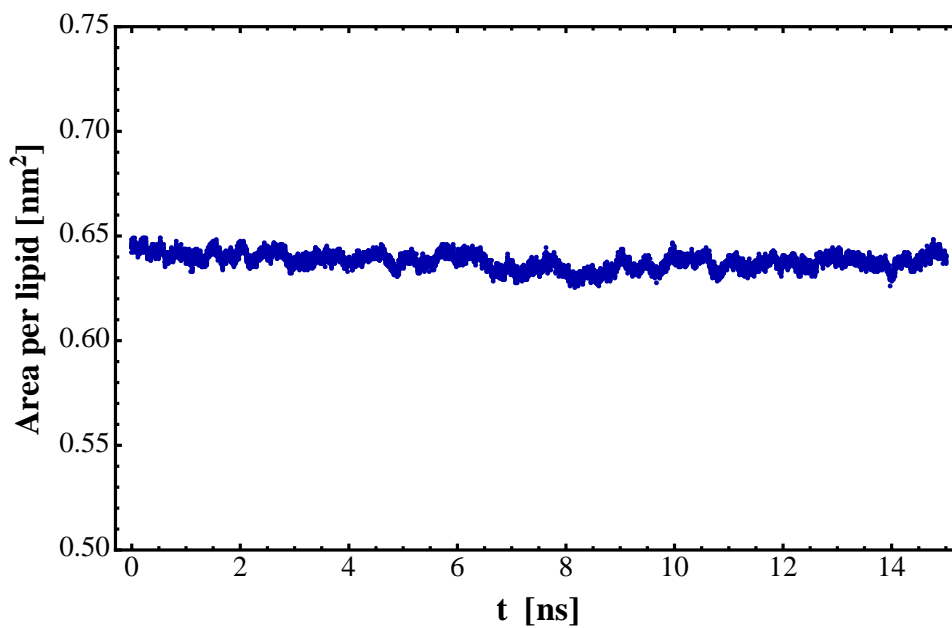


Figure 3.4: Total energy of the POPC bilayer during 15 ns simulation with OPLS-AA force-field. The system is in equilibrium.

The fluctuations of the surface area per lipid, which are presented in Fig. 3.5b, are relatively stable. The mean area per lipid is $0.638 \pm 0.004 \text{ nm}^2$, which is in good agreement with the experimental results. Published estimations of the surface area per POPC in the literature are 0.63 nm^2 using a surface pressure of 30 mN/m [Smaby *et al.* [1997]] and 0.66 nm^2 for a surface pressure of 20 mN/m [Hyslop *et al.* [1990]].



(a)



(b)

Figure 3.5: Plots representing the behavior of the system during the 15 ns production run. The plots show fluctuations of : a) the simulation box in all three dimensions; b) the area surface per lipid. Both are stable with the mean value of the latter of $0.638 \pm 0.004 \text{ nm}^2$, which indicates that the system is in equilibrium.

3.2.1.3 Extended simulation - 150 ns

For comparison, a longer 150 ns simulation was performed. Here the starting structure for the calculations was the last frame of the 15 ns simulation. Fig. 3.6 shows that the total energy of the membrane is stable. This is also true for the fluctuations of the simulation box (Fig. 3.7a).

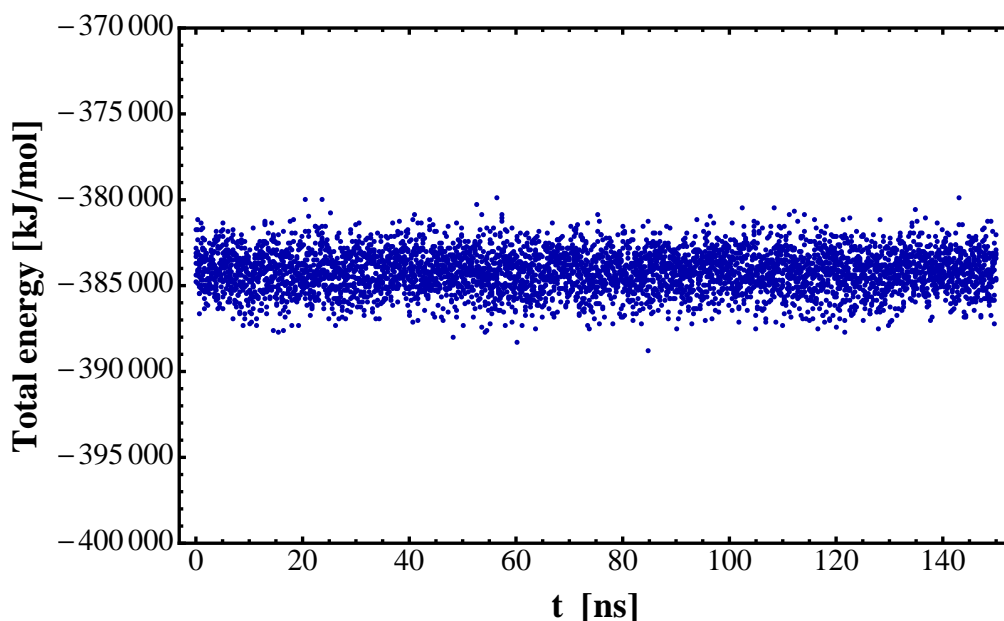
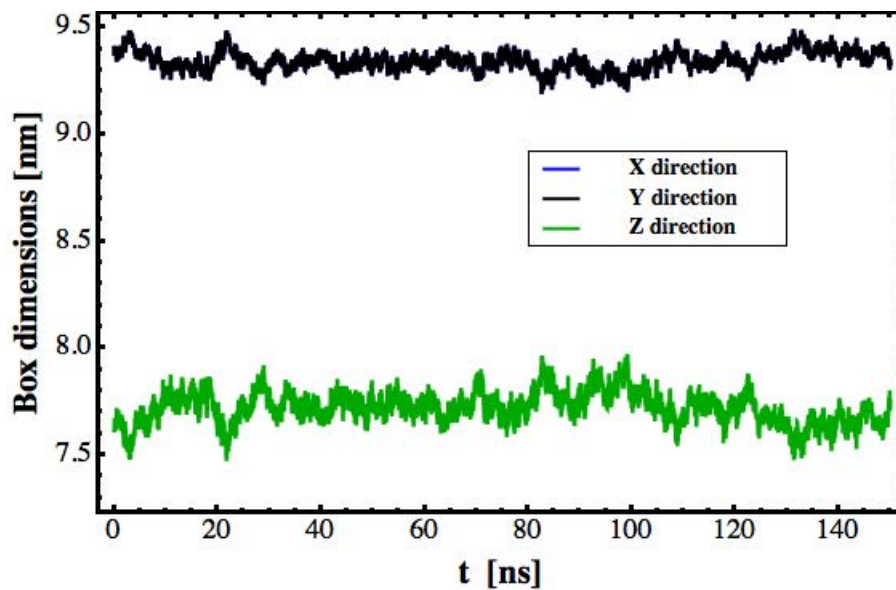
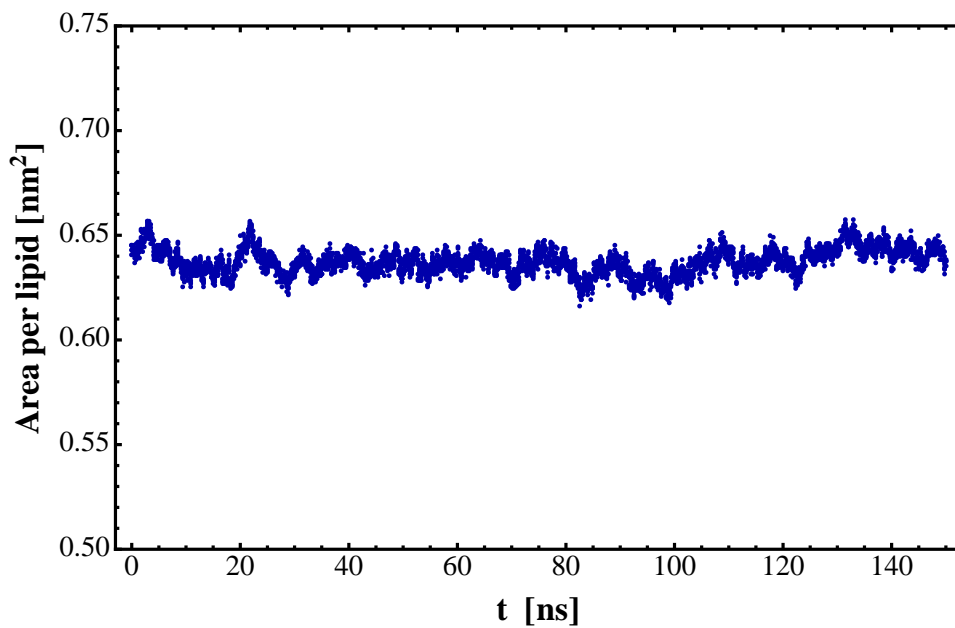


Figure 3.6: Total energy of the POPC bilayer of 150 ns all-atom simulation - the system is in energetic equilibrium.

The calculated mean surface area per POPC lipid, $0.637 \pm 0.006 \text{ nm}^2$, is very close to the value obtained for the 15 ns simulation. With the difference that the mean fluctuations are nearly twice larger. Nevertheless, the system can still be considered stable, as this value is much smaller than the difference of 0.03 nm^2 between the experimental surface areas obtained for 20 mN/m and 30 nM/m (Fig. 3.7b).



(a)



(b)

Figure 3.7: Plots show the fluctuations of the box (a) and the surface area per POPC (b) for 150 ns simulation. The mean area per lipid of $0.637 \pm 0.006 \text{ nm}^2$ is close to the value obtained for the 15 ns simulation.

3.2.2 MARTINI force-field

The MARTINI force-field parameters chosen in this thesis are very close to the ones published by the developers of the force-field [Marrink *et al.* [2004, 2007]]. The reduction of interaction centres in this ff allows for longer integration time-steps. In this study the integration time-step was chosen to be 30 fs for all simulations (the proposed values are between 20 fs and 40 fs). Coulomb and van der Waals interactions were smoothly switched to zero in a distance range, $r_{min} \leq r \leq r_{max}$ [Marrink *et al.* [2007]]. For short-range interactions $r_{min} = 0.9 \text{ nm}$ and $r_{max} = 1.2 \text{ nm}$ were used, and for long-range interactions $r_{min} = 0 \text{ nm}$ and $r_{max} = 1.2 \text{ nm}$. The simulations were conducted in two thermodynamic conditions - canonical (NVT) and pseudo-isothermal-isobaric (NAp_zT) [Marrink *et al.* [2007]]. A constant temperature of 320 K was kept using the Berendsen thermal bath with a relaxation time of $\tau_T = 1.5 \text{ ps}$. In case of NAp_zT simulations the surface area of the bilayer was constant and the Berendsen barostat adjusted only the pressure of 1 atm in direction perpendicular to the surface of the membrane. The coupling time constant was $\tau_p = 3 \text{ ps}$ and the compressibility $\beta = 4.5 \times 10^{-5} \text{ bar}^{-1}$.

3.2.2.1 System equilibration

In comparison to the all-atom calculations the procedure for the MARTINI system equilibration was much simpler, as the starting structure used for the simulations was already equilibrated. The system equilibration process was conducted for both systems for $1.2 \mu\text{s}$ in the respective ensembles, until drifts were sufficiently small. The mean surface area per POPC lipid is fixed at 0.666 nm^2 , which is very close to the experimentally estimated value of $0.673 \pm 0.013 \text{ nm}^2$ at a temperature of 323 K [Kučerka *et al.* [2011]].

3.2.2.2 600 ns production run in the canonical ensemble

After equilibration the system was simulated for additional 600 ns. The total energy of the bilayer, which is shown in Fig. 3.8, has attained stable fluctuations around the desired mean equilibrium value.

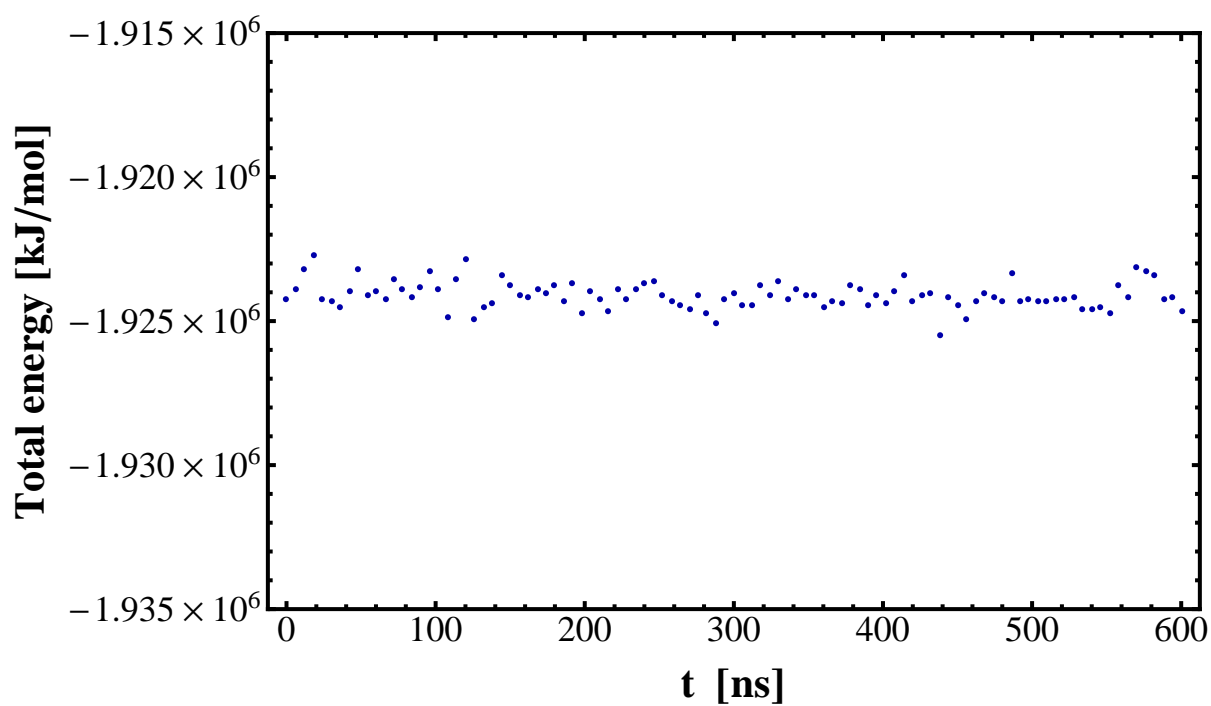


Figure 3.8: Total energy of 600 ns MARTINI simulation in NVT conditions.

3.2.2.3 600 ns production run in the NAp_zT ensemble

The simulations in the NAp_zT ensemble were performed for 600 ns, as well. The total energy of the bilayer is also reasonably stable, which is shown in Fig. 3.9.

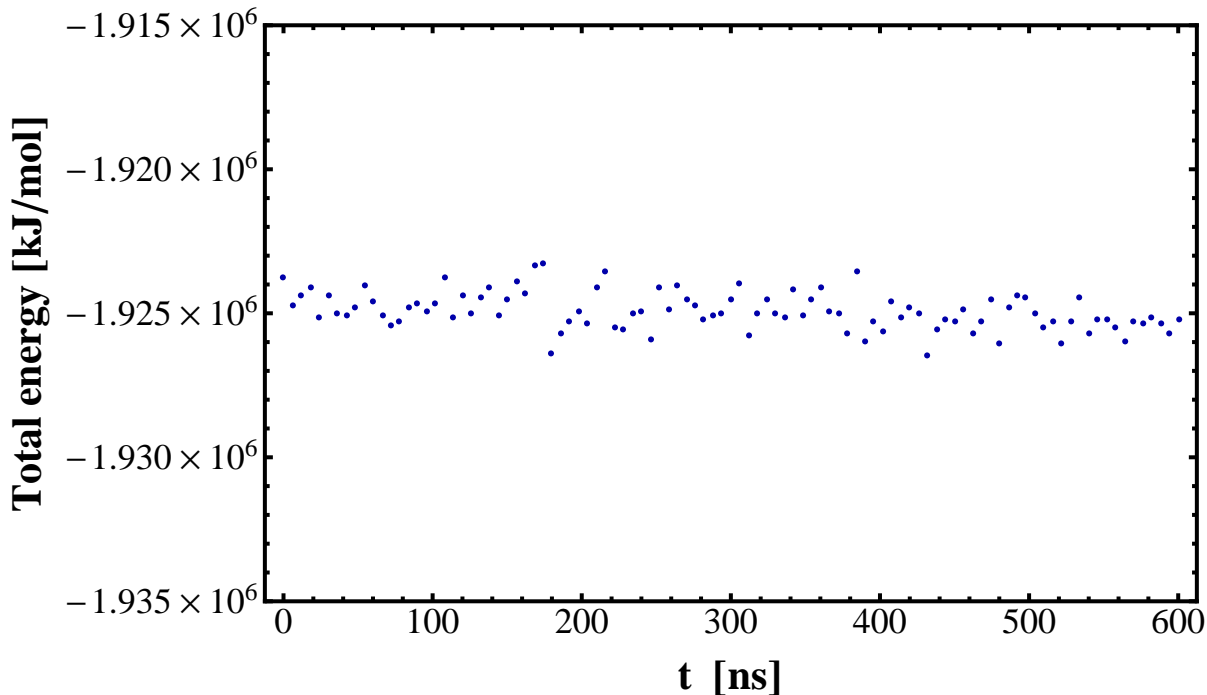


Figure 3.9: Total energy fluctuations of 600 ns MARTINI simulation in the NAp_zT ensemble.

3.3 Bulk water reference simulation

For comparison, a 100 ps simulation of SPC/E bulk water was performed in the canonical ensemble. The cubic simulation box of water of 5 nm edge length was created using GROMACS package [Hess *et al.* [2008]] and energetically equilibrated for 1 ns prior to

the production run. The starting velocities of atoms were generated according to the Maxwell-Boltzmann distribution for the temperature of 310 K. The system was coupled to the Berendsen thermostat to fix the temperature at 310 K, using a relaxation time of 90 fs. In the Fig. 3.10 fluctuations of the total energy during the production run are presented.

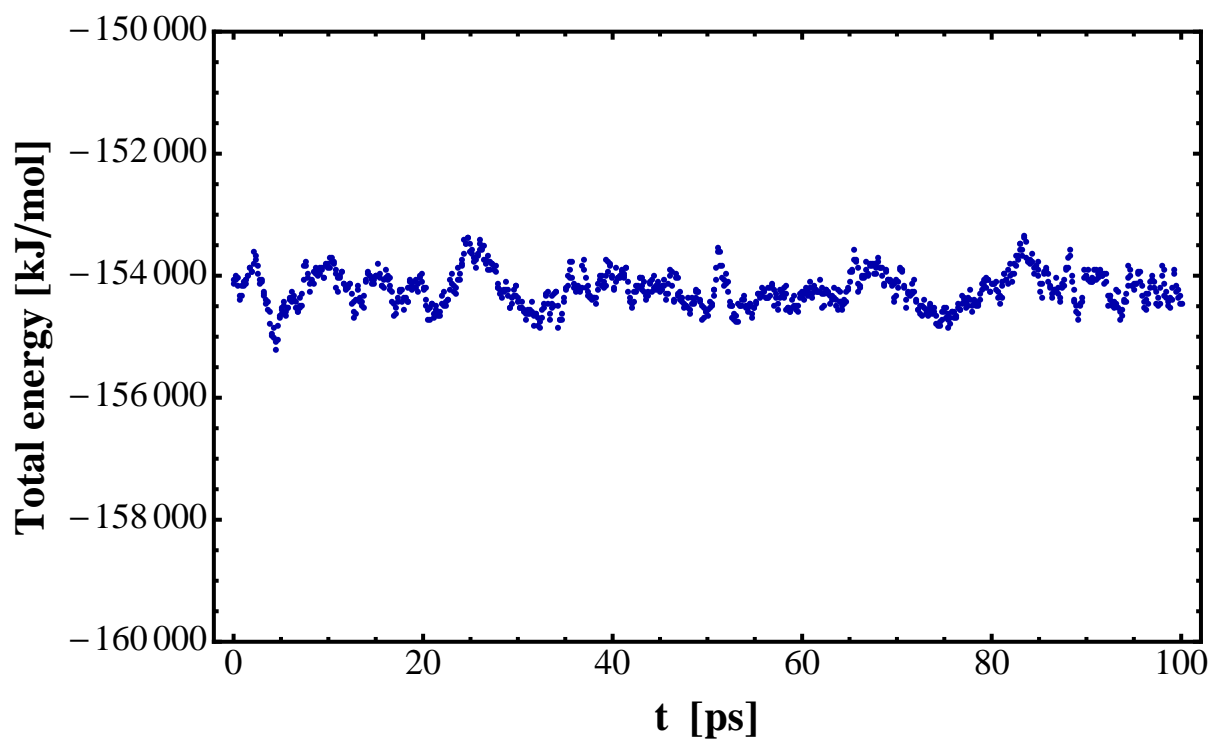


Figure 3.10: Fluctuations of the total energy of the reference box of bulk SPC/E water simulated for 100 ps.

Chapter 4

Results

4.1 Single molecule dynamics in a lipid bilayer

This chapter focuses on movements of a single lipid molecule. The single particle dynamics is described by autocorrelation functions [McQuarrie [2000]],

$$C(t) = \langle A(0) A(t) \rangle, \quad (4.1)$$

where $\langle \dots \rangle$ denotes a time average and A is the physical quantity under consideration. As an example, $A(t)$ can be the velocity of the molecule,

$$C_{vv}(t) = \langle \mathbf{v}(0) \cdot \mathbf{v}(t) \rangle. \quad (4.2)$$

Here \mathbf{v} is the velocity vector, which implies that $C_{vv}(t)$ is averaged over the three directions, X, Y, Z . In this thesis, all autocorrelation functions are calculated in the plane of the model membranes (lateral autocorrelation functions). It was mentioned earlier, the dynamics of the POPC lipids within the bilayers, is of main interest for this work.

The presented analyses of the OPLS all-atom and MARTINI coarse-grained simulations were performed with the nMoldyn program [Hinsen *et al.* [2012]; Kneller *et al.* [1995]].

4.1.1 Mean Square Displacements

The lateral mean square displacements, $W(t) = \langle (\mathbf{x}(t) - \mathbf{x}(0))^2 \rangle$, were calculated for the centers of mass (CM) of the all-atom and coarse-grained POPC lipids, using an efficient FFT implementation [Kneller *et al.* [1995]] of

$$W_i(n) \approx \frac{1}{N_f - n} \sum_{k=0}^{N_f - n - 1} (\mathbf{x}_i(k + n) - \mathbf{x}_i(n))^2. \quad (4.3)$$

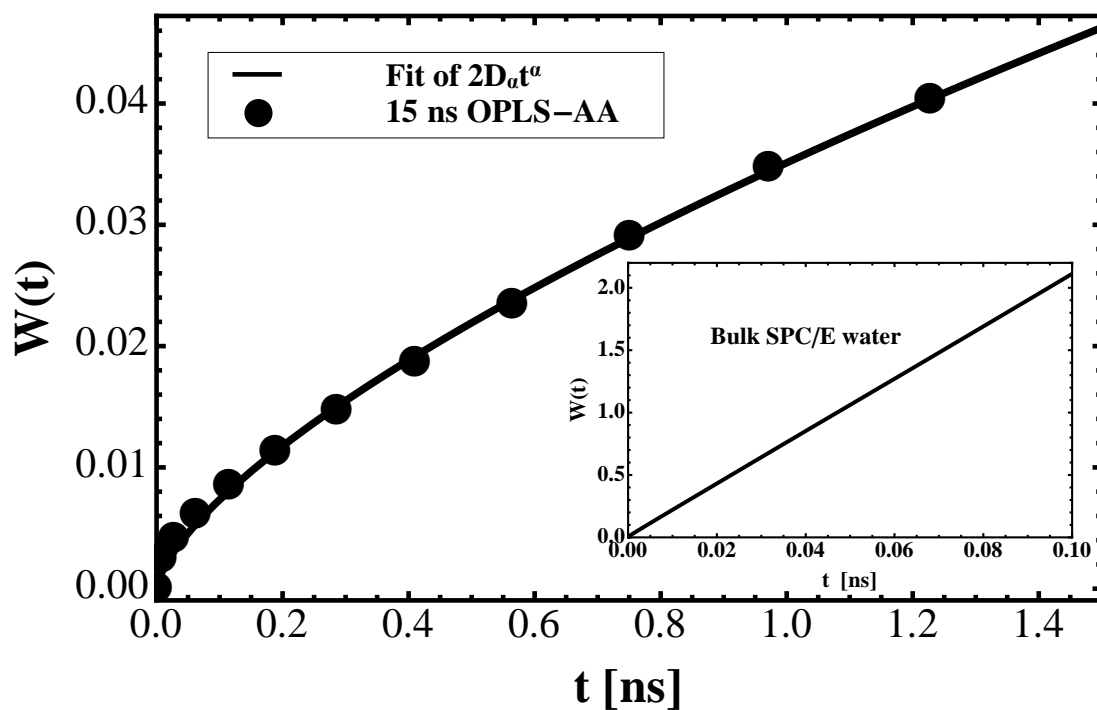
Here N_f is the total number of frames (time-steps) of the analysed trajectories, $\mathbf{x}(n) \equiv \mathbf{x}(n\Delta t)$, and Δt is the integration time-step. In order to raise statistical accuracy the center-of-mass MSDs were averaged over the total number of all lipids,

$$W_m = \frac{1}{N} \sum_{j=1}^N W_j(n) \quad (4.4)$$

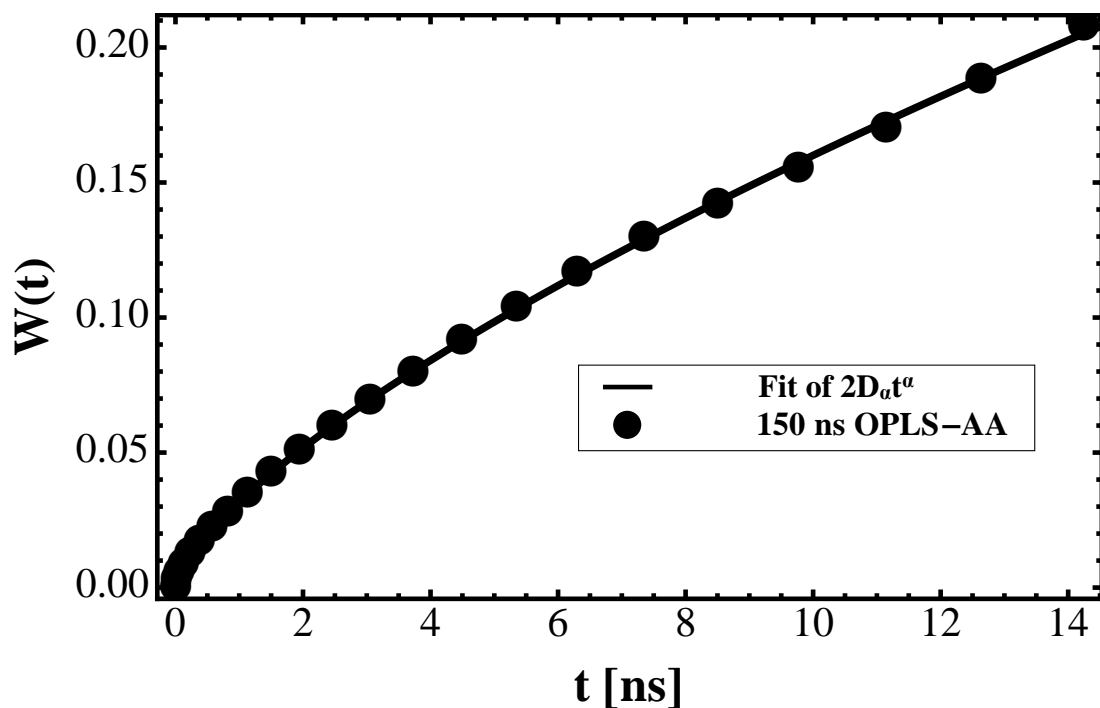
The maximum accessible lag-time of the analyses was chosen to be shorter than 10% of the total length of the MD trajectories. This choice was made in order to guarantee the statistical relevance of the results. For longer lag times the time averaging of the calculated functions might prove insufficient to obtain reliable results. Therefore the maximal lag-time for the 15 ns OPLS-AA simulation was 1.5 ns, 15 ns for the 150 ns OPLS-AA simulation and 50 ns for the MARTINI calculations.

4.1.1.1 Atom-detailed simulations

Expression (1.4) was fitted to the numerically lateral center-of-mass mean square displacements computed for both the shorter (15 ns) simulation and the longer (150 ns) simulation. The results are presented in Fig. 4.1. In both cases the MSDs exhibit clearly a sublinear behavior. This strongly contrasts with normal diffusion in case of simulated SPC/E water, for which the $W(t)$ evolves linearly with time (inset in Fig. 4.1a), as one expects for normal diffusion. The fitted values of the parameter α for 15 ns ($\alpha = 0.668$)



(a)



(b)

Figure 4.1: The MSD, $W(t)$, calculated for the centres of the masses of the POPC lipids simulated for 15ns (a) and 150 ns (b). The inset in (a) shows the MSD for normal diffusion (SPC/E water).

and 150 ns ($\alpha = 0.701$) fall in the regime of subdiffusion. These results are consistent with the experimentally determined value of $\alpha \approx 0.74$ for biological membranes [Schwille *et al.* [1999a]] and with simulation results of pure DOPC bilayer, $\alpha = 0.61$ [Kneller *et al.* [2011]]. This comparison shows that the characteristics of lateral diffusion in these biological membranes is the same. The fitted fractional diffusion constants D_α for POPC have values of $0.016 \frac{nm^2}{ns^\alpha}$ (150 ns) and $0.018 \frac{nm^2}{ns^\alpha}$ (15 ns). In order to compare obtained fractional diffusion constants with the value for DOPC ($D_\alpha = 0.101 \frac{nm^2}{ns^\alpha}$), one can calculate the typical time scale τ_{vacf} , which quantifies the asymptotic regime for VACF and depends on D_α and α parameter (more details are given in next section). The typical time scale τ_{vacf} is related to friction in a system as $\tau_{vacf} = \gamma^{-1}$. Therefore the larger τ_{vacf} the faster observed diffusion. For the POPC simulations calculated $\tau_{vacf} = 0.065 ps$ and $\tau_{vacf} = 0.046 ps$ for 15 ns and 150 ns simulations, respectively, are smaller than for the DOPC $\tau_{vacf} = 0.345 ps$, which shows the time scale of subdiffusive motions for the both systems is clearly different. The lateral diffusion of DOPC lipids in the bilayer is thus several times faster than for POPC membrane. This can be explained by the fact that the latter is less fluid at the same temperature - its main phase transition from gel to liquid, occurs at 270 K, while the transition for DOPC happens already

Table 4.1: Diffusion fractional constants, D_α and α parameters obtained from the fit of the Eq. (1.4) to the CM MSDs of POPC lipids for 15 ns and 150 ns OPLS-AA simulations.

OPLS-AA		
	15 ns	150 ns
α	0.668	0.701
$D_\alpha (nm^2/ns^\alpha)$	0.018	0.016

at 256 K [Lewis *et al.* [1988]; Litman *et al.* [1991]]. In comparison, the experimental value of $D_\alpha = 0.088 \pm 0.007 \frac{nm^2}{ns^\alpha}$ for $\alpha = 0.701$ has $\tau_{vacf} = 0.117 ps$, which is twice larger than for POPC and three times smaller than for DOPC. In this context it is important to underline that the experimental results in Ref. Schwille *et al.* [1999a] concern studies of a different type of lipid - DLPC (dilauroyl-sn- glycerol-3- phosphocholine), but computed τ_{vacf} for the simulations of POPC are of the right order of magnitude.

Due to the lack of any experimental works on fractional diffusion constants for POPC lipids, one can only compare results for the normal diffusion. NMR studies on the temperature dependence of normal diffusion constant ($\alpha = 1$) for POPC give values of $D = 0.012 \pm 0.004 \frac{nm^2}{ns}$ for the temperature of 308.15 K [Lindblom *et al.* [1981]] and $D = 0.014 \pm 0.002 \frac{nm^2}{ns}$ for 323.15 K [Köchy & Bayerl [1993]], which correspond to $\tau_{vacf} = 0.0017 ps$ and $\tau_{vacf} = 0.0021 ps$, respectively. These values are much smaller than τ_{vacf} obtained for the simulations, which means that diffusion of POPC lipids observed in the NMR experiments is much slower.

4.1.1.2 Coarse-grained force-field results

I recall that the mass of one lipid is $M_{AA} = 760.08 amu$, while the total mass of coarse-grained POPC lipid, M_{CG} , is 936 *amu* ("amu" : means atomic mass units). Obviously motions of heavier lipid molecules would be slower in comparison to lighter lipids and hence have a reduced fractional diffusion constant, D_α , which is proportional to the amplitude of the velocity autocorrelation function, C_{vv} [Kneller [2011]],

$$D_\alpha = \frac{1}{\Gamma(\alpha + 1)} \int_0^\infty dt {}_0\partial_t^{\alpha-1} C_{vv}(t), \quad (4.5)$$

where ${}_0\partial_t^{\alpha-1} C_{vv}(t) = d/dt \int_0^t dt' \Gamma(2 - \alpha)^{-1} (t - t')^{1-\alpha} C_{vv}(t')$ is the fractional Riemann-Liouville derivative of order $(\alpha - 1)$. As $C_{vv}(0)$ is the mean squared velocity, $\langle |\mathbf{v}|^2 \rangle = 2k_B T/m$, the reduction of the D_α is of around 20% ($\frac{M_{AA}}{M_{CG}} \approx 0.8$). In order to compensate

for that, the simulations with the MARTINI force-field were conducted at a higher

Table 4.2: Experimental values of the diffusion constant of POPC lipids for different temperatures [Köchy & Bayerl [1993]].

	Temperature		
	10°C	30°C	50°C
D ($10^{-12} \text{ m}^2/\text{s}$)	2.1 ± 0.7	4.0 ± 0.8	7.0 ± 1.0

temperature than the all-atom calculations. According to the temperature dependence of the POPC diffusion constant shown in Table 4.2 [Köchy & Bayerl [1993]], the rise of 10 K (10°C), from 310 K to 320 K, results in estimated increase of the diffusion constant by $\approx 23\%$. Therefore MARTINI simulations were performed at a temperature of 320 K. The lateral mean square displacements for both MARTINI simulations (with canonical, NVT, and pseudo-isothermal-isobaric, NAp_zT , thermodynamic conditions) were calculated for maximal time-lags of 50 ns, which is less than 10 % of the total trajectory length

Table 4.3: Fractional diffusion constants, D_α and α parameters obtained from the fit of Eq. (1.4) to the CM MSDs of coarse-grained POPC lipids for 600 ns NAp_zT and NVT simulations.

	MARTINI			
	NAp_zT 1.5 ns	NVT 1.5 ns	NAp_zT 50 ns	NVT 50 ns
α	0.515	0.508	0.571	0.558
D_α ($\text{nm}^2/\text{ns}^\alpha$)	0.057	0.058	0.051	0.051

(Fig. 4.2). The MSDs are very similar, especially for the shorter time-lags of 1.5 ns (inset

in Fig. 4.2), for which both MSDs are practically identical. The parameters from the fits of Eq. (1.4), which are presented in Table 4.3, give very similar values. The fractional diffusion constants D_α from the fits up to 50 ns are the same for the NVT and NAP_zT simulations: $0.051 \frac{nm^2}{ns^\alpha}$. The corresponding α parameters of $\alpha = 0.558$ and $\alpha = 0.571$, respectively, have also very similar values, and lie in the range of subdiffusion.

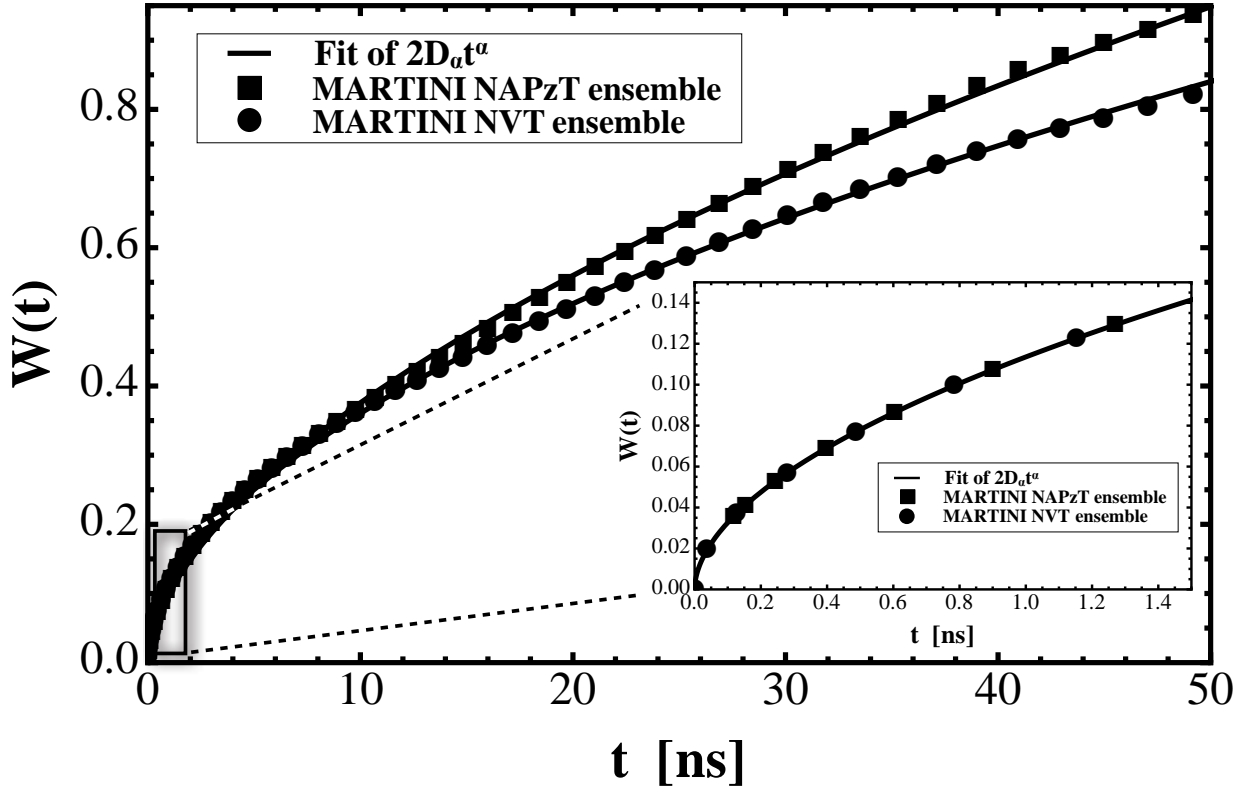


Figure 4.2: The MSD, $W(t)$, calculated for the centres of the masses of the lipids simulated for 600 ns.

In comparison to the results from the fits for 50 ns, the fractional diffusion constants obtained from the fits for a maximum time lag of 1.5 ps are slightly higher, but the values of α are smaller, meaning that for the longer time-lags the motions of molecules are "less

normal". The calculated mean $\tau_{\text{vacf}} = 0.44 \text{ ps}$ and $\tau_{\text{vacf}} = 0.30 \text{ ps}$ for the shorter (1.5 ns) and longer (50 ns) maximal time-lag, respectively, are very similar, which shows that analyses for shorter time-lags as short as 1.5 ns are already representative.

4.1.1.3 Comparison between OPLS-AA and MARTINI force-fields

In Figure 4.3 the lateral mean squared displacements for the simulations with the 15 ns OPLS-AA and the 600 ns MARTINI force field (*NVT* and *NAP_zT* ensembles in the latter case) are presented. The MSDs are compared for a maximal time-lag of 1.5 ns. For all simulations the calculated MSDs have a sublinear form. The curve of the all-atom MSD

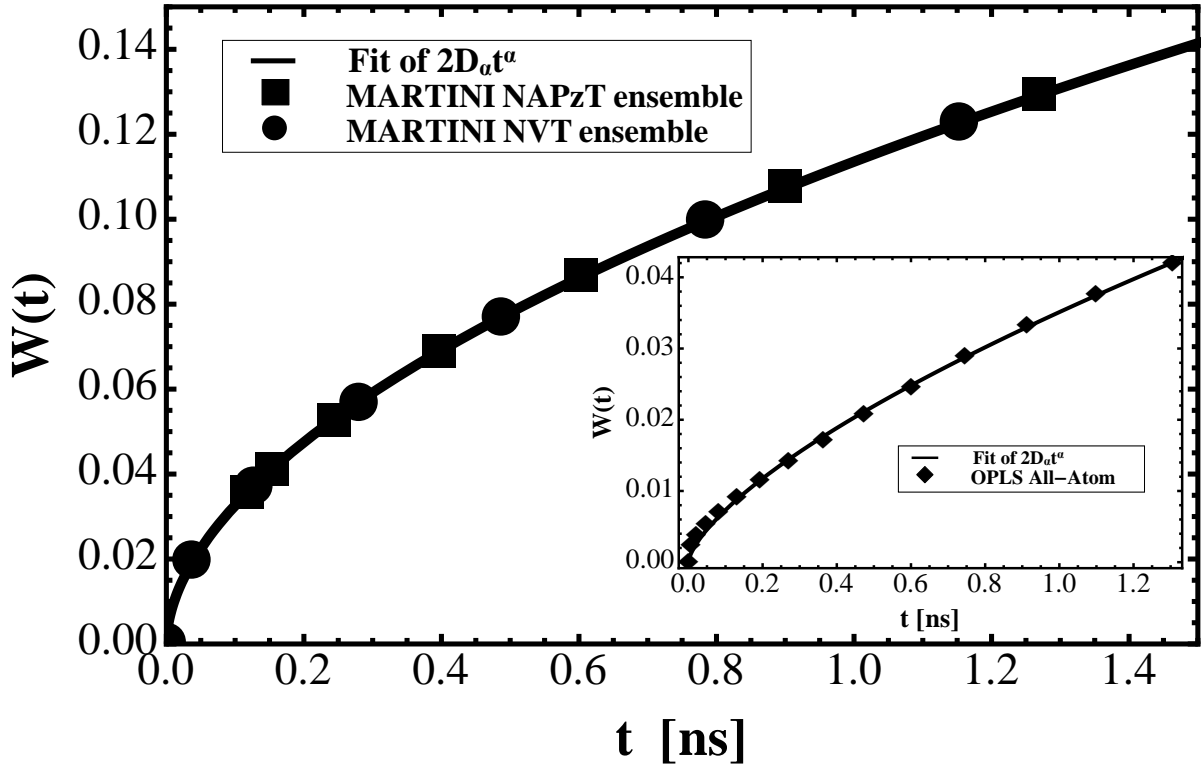


Figure 4.3: Comparison of the centre of mass MSDs calculated for the 15 ns all-atom and the 600 ns coarse-grained simulations (the maximal time-lag is 1.5 ns).

seems to be slightly more linear than for the coarse-grained case. This observation is reflected in a higher value of α parameter (see Table 4.4), implying more "normal" diffusional motions of all-atom POPC lipids. In all cases the fractional diffusion constants ($D_\alpha \approx 0.05 \frac{nm^2}{ns^\alpha}$) and $\tau_{vacf} = 0.44 ps$ and $\tau_{vacf} = 0.30 ps$ for the shorter (1.5 ns) and longer (50 ns) maximal time-lags are several times higher than the values for the all-atom simulations ($D_\alpha = 0.018 \frac{nm^2}{ns^\alpha}$) with $\tau_{vacf} = 0.065 ps$. This result is consistent with other findings showing that calculated diffusion constants from the MARTINI simulations are in most cases several times higher than experiments predict [Marrink *et al.* [2004, 2007]]. Moreover the scaling value of 4 has been mentioned in these works in case of motions of MARTINI water beads, where it was shown that diffusion constant is 4 times higher than the experimental value. This difference can be attributed to less detailed structure

Table 4.4: Fractional diffusion constants, D_α and α parameters obtained from the fit of Eq. (1.4) to the CM MSDs of coarse-grained POPC lipids for 600 ns NAp_zT and NVT simulations.

	OPLS-AA		NAp_zT CG		NVT CG	
	15 ns	150 ns	1.5 ns*	50 ns*	1.5 ns*	50 ns*
α	0.668	0.701	0.515	0.571	0.508	0.558
$D_\alpha (nm^2/ns^\alpha)$	0.018	0.016	0.057	0.051	0.058	0.051

of MARTINI lipids (13 beads in comparison to 134 atoms building real POPC molecule) and therefore smaller number of individual interactions between them. This could lead to less hindered movements, so faster lateral movements of POPC lipids.

The above results show, however, also that the dynamics obtained by the coarse-grained simulations with the MARTINI force-field, preserves the subdiffusive character of the lipid

motions.

It is worth noting that a transition from anomalous to normal diffusion was reported by Flenner *et al.* [2009] on a time scale of 10 ns and normal diffusion for POPC with the MARTINI ff by Niemelä *et al.* [2010], who analyzed a 500 ns simulation. In this work the subdiffusive nature of lipids motions is preserved for 15 ns and up to 50 ns for the all-atom and the 600 ns coarse-grained POPC lipids simulations, respectively. A possible explanation for these discrepancies is the statistical error, which is induced by using appropriate maximal lag-times.

4.1.1.4 Bulk water comparison with membrane hydration water

In order to verify if the simulated system of bulk water reproduces the behavior of a real water system, in particular normal diffusion, it is compulsory to compare the diffusion constant obtained from the simulation with an experimental value. Figure 4.4 shows the mean square displacement calculated for the reference SPC/E bulk water, which was simulated for 100 ps in canonical thermodynamic conditions at the temperature of 310 K (section 3.3). The diffusion constant calculated from the fit of Relation (1.3), gives the value of $3.528 \cdot 10^{-9} \frac{m^2}{s}$ ($3.528 \frac{nm^2}{ns}$). In comparison to experimental findings, where the diffusion constant is $D = 2.919 \cdot 10^{-9} \frac{m^2}{s}$ [Mills [1973]] for temperature of 307.15 K, the obtained value is reasonably close. According to studies of Mark & Nilsson [2001], simulations using the SPC/E water model yield best diffusion constants (compared to other models, e.g. TIP3P and SPC), but still the obtained value is about 20 % too large for the given temperature.

A very interesting subject is the behavior of water around lipid membranes. Experimental findings show that water molecules close to the surface of biological membranes interact with lipid molecules, forming a particular hydration layer [Arnold *et al.* [1983]; Fitter & Lechner [1999]; Gawrisch *et al.* [2007]; Pearson & Pascher [1979]]. They create a network of intermolecular bonds between lipids, which are linked to each other via hy-

drogen bonds of water molecules, so-called water-bridges, and thus stabilize the structure of membrane [Binder *et al.* [1999]; Mombelli *et al.* [2003]; Pasenkiewicz-Gierula *et al.* [1997]; Pearson & Pascher [1979]; Róg *et al.* [2009]; Steinbauer *et al.* [2003]].

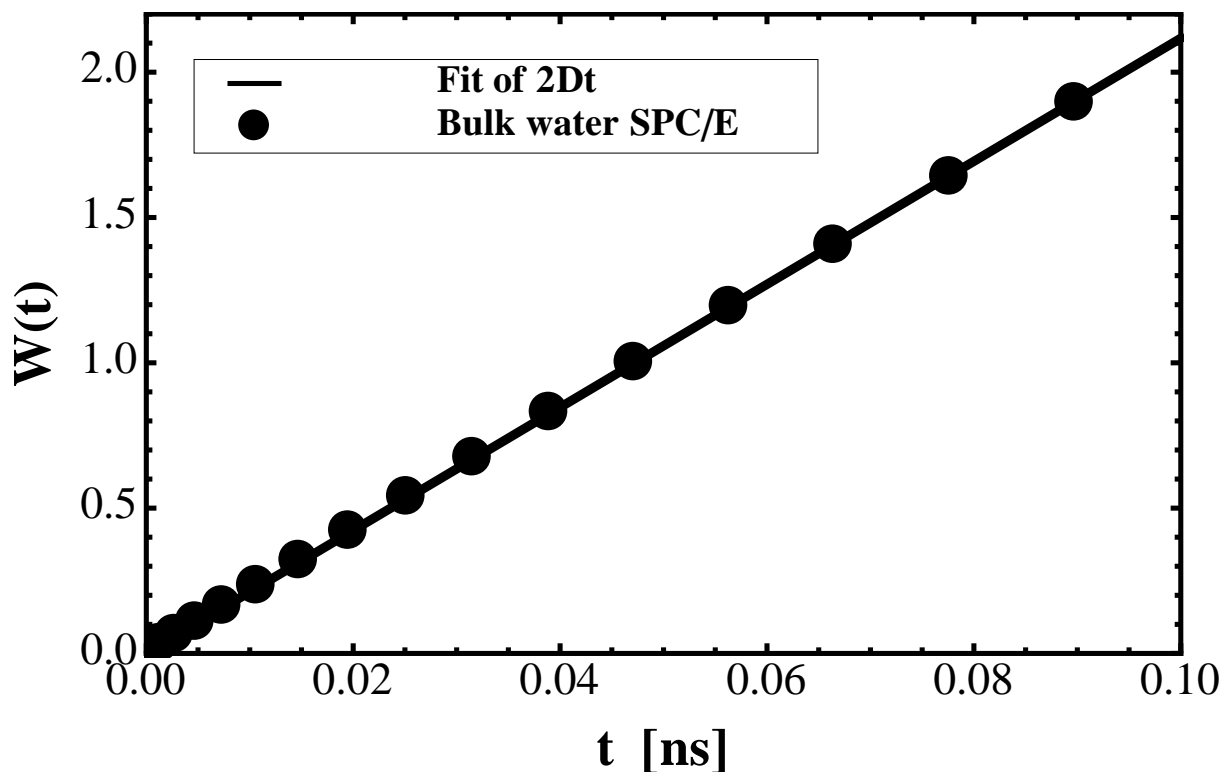
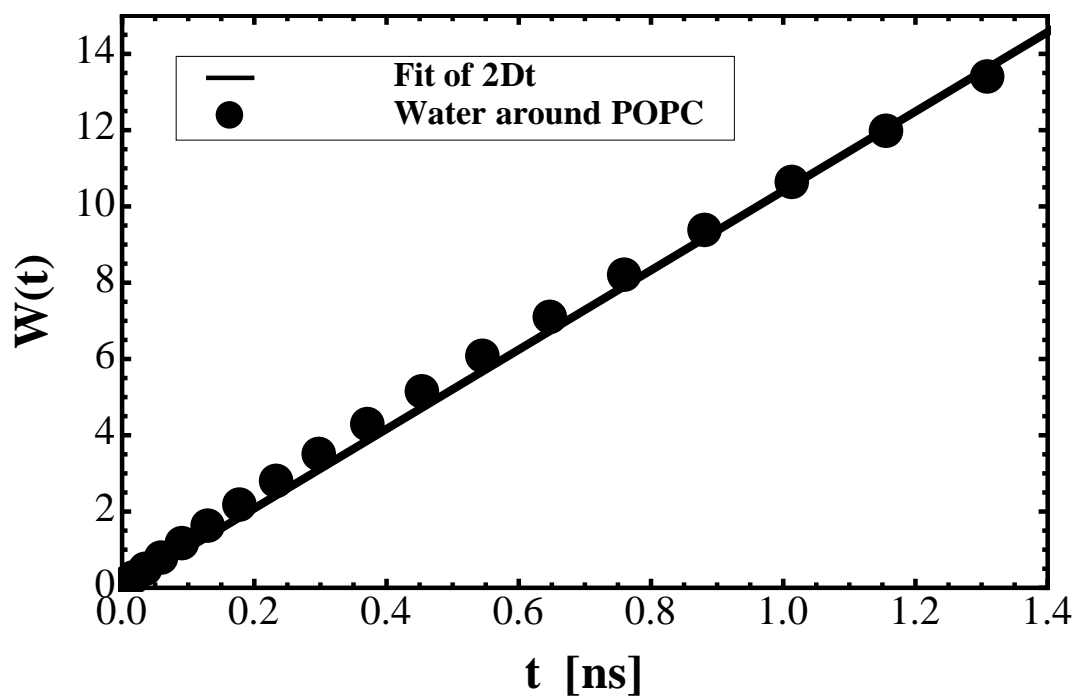


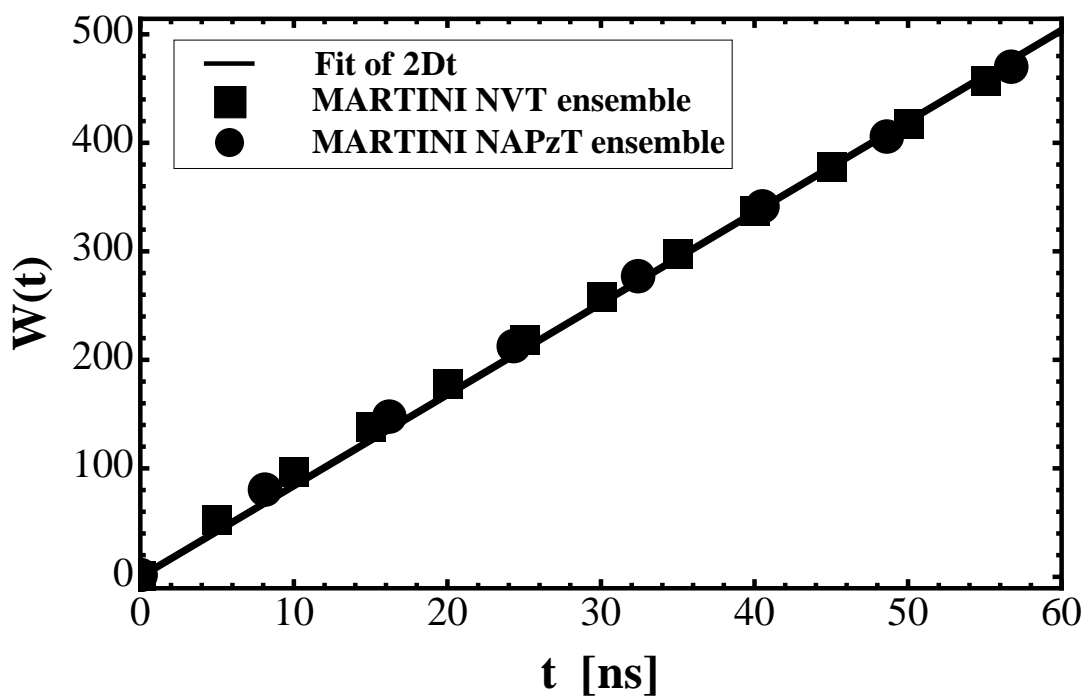
Figure 4.4: $W(t)$, calculated for the centres of the masses of the bulk SPC/E water simulated for 100 ps.

This obviously affects motions of water and some findings show a reduction of the diffusion constant by a factor of 2-5 in comparison to bulk water [Fitter & Lechner [1999]; Gawrisch *et al.* [2007]; Pasenkiewicz-Gierula *et al.* [1997]; Róg *et al.* [2009]].

Although this subject was not in the focus of this thesis, some short analysis can be given on the water motions in studied POPC systems in this thesis. The hydration level of atom detailed OPLS POPC bilayer and coarse-grained MARTNI membrane is ≈ 38



(a)



(b)

Figure 4.5: The MSD, $W(t)$, calculated for the centres of the masses of the water around POPC bilayer in case of 15 ns all-atom simulation (a) and 600 ns MARTINI (b).

water molecules and ≈ 28 water beads per POPC lipid, respectively. The reported number of water molecules forming hydrogen bridges vary with the type of lipids, but in case of fully hydrated POPC it may include up to average ≈ 9.4 molecules per one POPC lipid [Gawrisch *et al.* [2007]]. This means that $\approx 25\%$ of all water molecules surrounding simulated bilayers are potentially involved in forming water bridges. This should have an influence on the average diffusion constant of the simulated water molecules (alternatively water beads). Figure 4.5 shows plots of the mean square displacements for the centre of mass of SPC/E water from 15 ns OPLS-AA simulations (Fig. 4.5a) and for water beads of both, NVT and NAP_zT 600 ns MARTINI simulations (Fig. 4.5b). The calculated diffusion constants of $1.721 \cdot 10^{-9} \frac{m^2}{s}$ ($1.721 \frac{nm^2}{ns}$) (OPLS-AA) and $1.399 \cdot 10^{-9} \frac{m^2}{s}$ ($1.399 \frac{nm^2}{ns}$) (MARTINI) are indeed smaller than for the bulk SPC/E water - $3.528 \cdot 10^{-9} \frac{m^2}{s}$ ($3.528 \frac{nm^2}{ns}$), i.e. by a factor of ≈ 2 (Table 4.5).

Table 4.5: Comparison of the diffusion constants of a bulk and surrounding lipid bilayer SPC/E water, water in the MARTINI POPC simulations and the experimental value [Mills [1973]].

WATER				
	bulk SPC/E	SPC/E (mem.)	CG (mem.)	exper.
D ($10^{-9} m^2/s$)	3.528	1.721	1.399	2.919

This indicates that in the simulated systems presented in this thesis, similarly to earlier findings, exist strong water interactions involving water molecules/beads and POPC lipids in model membranes. Very interesting is the fact that diffusion constants for water beads in MARTINI systems (which are exactly the same for both thermodynamic conditions) is smaller than for all-atom case. This would suggest a much stronger effect of water-bridging (especially when the reported diffusion constant of bulk MARTINI water is ≈ 4

higher than experimental result [Marrink *et al.* [2007]]. This matter would need more further investigation to give a more coherent view of the problem.

4.1.2 Velocity autocorrelation function analysis

For the following considerations we need that the MSD and VACF are related via [Boon & Yip [1991]]

$$W(t) = 2 \int_0^t (t - t') C_{vv}(t') dt', \quad (4.6)$$

It follows now from Eq. (1.7) that its Laplace transform behaves as [Kneller [2011]]

$$\hat{W}(s) \stackrel{s \rightarrow 0}{\sim} 2D_\alpha \frac{\Gamma(\alpha + 1)}{s^{\alpha+1}}, \quad (4.7)$$

and on the other hand it follows from Eq. (4.6) :

$$\hat{W}(s) = \frac{2\hat{C}_{vv}(s)}{s^2}, \quad (4.8)$$

For an arbitrary function $f(t)$ the Laplace transform is defined as $\hat{f}(s) = \int_0^\infty dt \exp(-st) f(t)$ ($\Re\{s\} > 0$). The relation between asymptotic form of MSD and VACF can be obtained by comparing Eqs. (4.7) and (4.8), which leads to [Kneller [2011]]:

$$\frac{\hat{C}_{vv}(s)}{s} \stackrel{s \rightarrow 0}{\sim} D_\alpha \Gamma(\alpha + 1) s^{-\alpha}, \quad (4.9)$$

where $\hat{C}_{vv}(s)/s$ is the Laplace transform of the integral

$$f_c(t) = \int_0^t dt' C_{vv}(t'). \quad (4.10)$$

Since Eq. (4.9) is singular for any $\alpha > 0$, as s approaches zero, one obtains the equivalence

$$\hat{f}_c(s) \stackrel{s \rightarrow 0}{\sim} D_\alpha \Gamma(\alpha + 1) s^{-\alpha} \Leftrightarrow f_c(t) \stackrel{t \rightarrow \infty}{\sim} \alpha D_{\alpha-1} t^{\alpha-1} \quad (4.11)$$

and finally [Kneller [2011]]

$$W(t) \stackrel{t \rightarrow \infty}{\sim} 2D_\alpha t^\alpha \Leftrightarrow f_c(t) \stackrel{t \rightarrow \infty}{\sim} \alpha D_{\alpha-1} t^{\alpha-1}. \quad (4.12)$$

Since $C_{vv}(t) = df_c(t)/dt$, one obtains from Expression (4.12) the necessary condition

$$W(t) \stackrel{t \rightarrow \infty}{\sim} 2D_\alpha t^\alpha \Rightarrow C_{vv}(t) \stackrel{t \rightarrow \infty}{\sim} D_\alpha \alpha (\alpha - 1) t^{\alpha-2} \quad (4.13)$$

for the long-time tail of the VACF. I mention here that Expression (4.5) for the fractional diffusion constant follows from Eq. (4.9).

The asymptotic regime can be quantified as $t \gg \tau_{\text{vacf}}$, where [Kneller *et al.* [2011]]:

$$\tau_{\text{vacf}} = \left(\frac{D_\alpha}{\langle \mathbf{v}^2 \rangle} \right)^{\frac{1}{2-\alpha}}. \quad (4.14)$$

To facilitate comparisons in the time domain, the VACFs in this thesis are presented normalized,

$$\psi(t) = \frac{C_{vv}(t)}{C_{vv}(0)} \quad (4.15)$$

and the long-time tail of the integral (4.10) behaves then:

$$f_\psi(t) \stackrel{t \rightarrow \infty}{\sim} \frac{D_\alpha \alpha}{\langle \mathbf{v}^2 \rangle} t^{\alpha-1}. \quad (4.16)$$

The velocity autocorrelation functions were computed for the center of masses (CM) of the POPC lipids according to

$$C_i(n) \approx \frac{1}{N_f - n} \sum_{k=0}^{N_f - n - 1} (\mathbf{v}_i(k) \cdot \mathbf{v}_i(k + n)), \quad (4.17)$$

where N_f is the total number of frames (time-steps) of the analysed trajectories. Here $\mathbf{x}(n) \equiv \mathbf{x}(n\Delta t)$ and Δt is the integration time-step. For reasons of efficiency, Expression (4.17) is computed by a FFT-based Fast Correlation Algorithm [Kneller *et al.* [1995]]. Similarly to the computation of the MSDs, Eq. (4.4), all the VACFs were averaged over the total number of all the lipids, N :

$$C_m = \frac{1}{N} \sum_{j=1}^N C_i(n) \quad (4.18)$$

The integration of the numerical normalized VACFs of the timestep, Δt , was performed by using the central difference scheme [Stachura & Kneller [2013]],

$$f_\psi(n) \approx \sum_{k=0}^{0 < n < N_t - 1} \frac{\Delta t}{12} (8\psi(k) + 5\psi(k-1) - \psi(k+1)). \quad (4.19)$$

The velocity autocorrelation functions for the 15 ns all-atom OPLS and 600 ns coarse-grained MARTINI (NVT and NAp_zT) simulations are presented in Fig. 4.6. The VACF curves for the MARTINI case are identical for both ensembles. This is consistent with the observation of the MSDs for short time-lags of maximum 1.5 ns (section 4.1.1.2), which were also indistinguishable for the NVT and NAp_zT conditions. One distinguishes two regimes in the VACF: a short-time regime, containing the minimum of the VACF, which extends up to $\approx 3ps$, and a long-time regime. In case of the OPLS-AA ff the minimum is deeper and starts earlier than for the MARTINI ff. This suggests a weaker "cage effect" for the latter and faster lateral motions of the coarse-grained lipids. This is true in light of the MSD calculations, for which the fractional diffusion constants are higher than for the atom detailed simulations. In addition the VACFs of MARTINI simulations have a "bump" around 0.7 ps. The origins of it have not been discerned and do not have any theoretical explanation. More important is the long-time tail of the VACFs, which

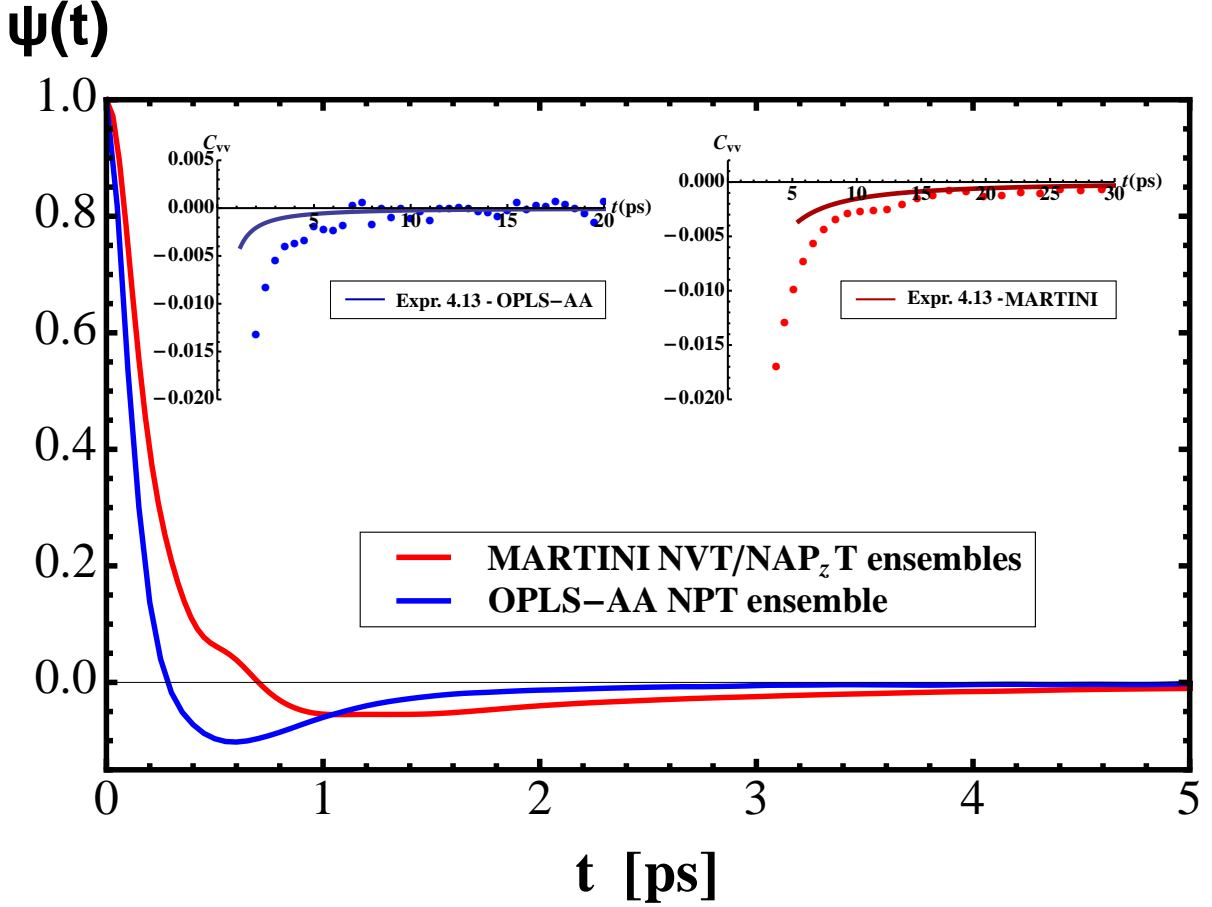
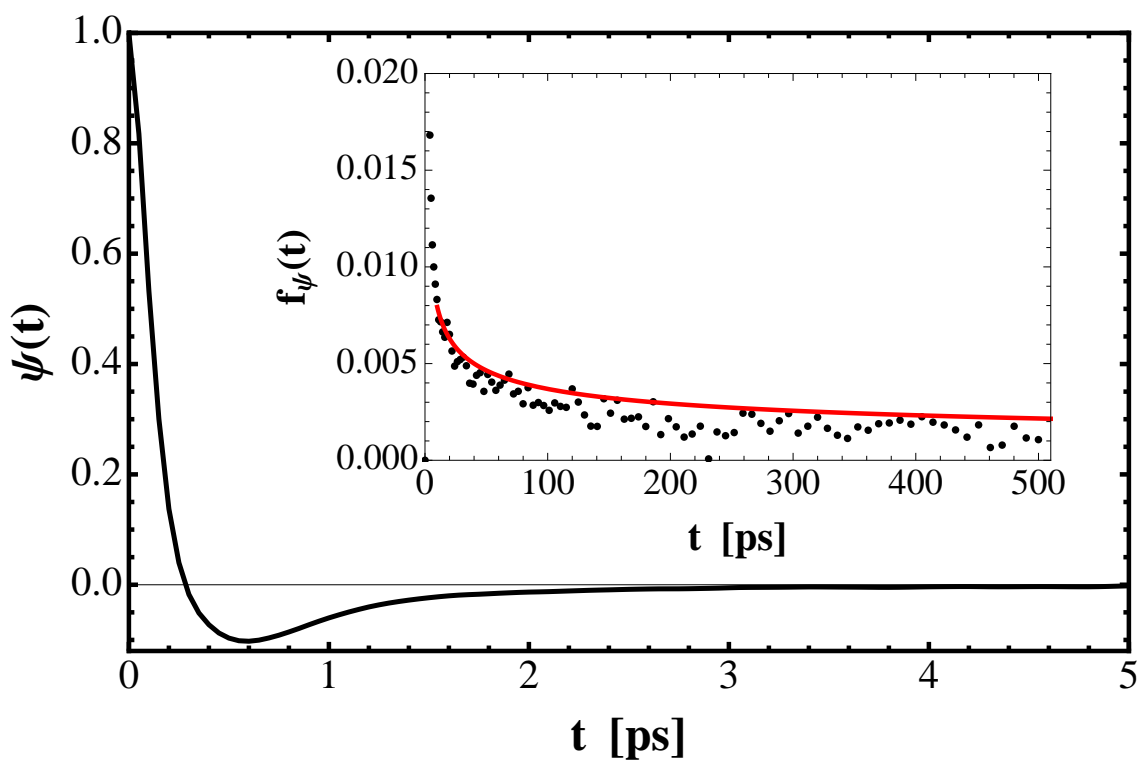
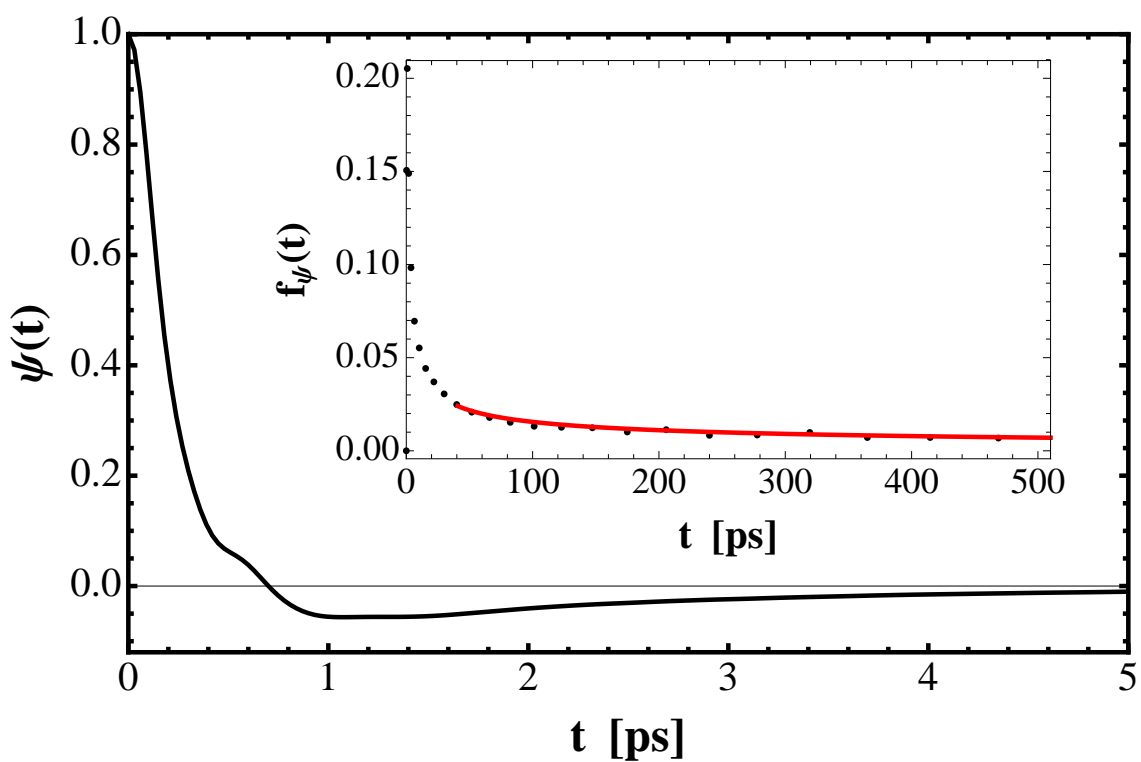


Figure 4.6: Comparison of the centre of mass Velocity Autocorrelation Functions calculated for the 15 ns all-atom and 600 ns coarse-grained simulations.

for both, the all-atom and the coarse-grained calculations, get closer to each other for longer time-lags and both approach asymptotically zero from negative values. Negative velocity autocorrelations of the molecules can be expressed in physical terms, namely as the tendency of reversing the direction of motion and staying localized for longer times ("cage effect"). The calculated typical time scales τ_{vacf} , Eq. (4.14), of 0.065 ps for OPLS-AA and 0.293 ps for MARTINI (the mean squared velocities $\langle \mathbf{v}^2 \rangle = 0.0057 \frac{\text{nm}^2}{\text{ps}^2}$ and $\langle \mathbf{v}^2 \rangle = 0.0068 \frac{\text{nm}^2}{\text{ps}^2}$ for the coarse-grained and all-atom lipids, respectively) define the asymptotic regime, which stands for $t \gg \tau_{\text{vacf}}$. The superposition of the model for



(a)



(b)

Figure 4.7: Comparison of the integrals over the centre of mass VACFs calculated for the 15 ns all-atom and 600 ns coarse-grained simulations.

the VACF tail, Eq. (4.13), with the values of the fractional diffusion constants and α parameters from the MSD fits (Table 4.4) are shown in the insets of Fig. 4.6. The theoretical curves start to converge with calculated VACFs for long time-lags, which are already noisy (especially in case of the all-atom simulations). The agreement is much less good than in earlier work on DOPC [Kneller *et al.* [2011]]. For this reason the long time-tails of the integrated VACFs were calculated, which are in consistent with the analytical forms of Eq. (4.10) (insets in Fig. 4.7), clearly indicating subdiffusive character of POPC lipid diffusion. The agreement is much better for the coarse-grained simulations, which is the result of better statistical accuracy than for the all-atom case. The available time lags are over 40 times longer trajectory than in the OPLS simulations and the correlation functions can be averaged over 7 times more POPC lipids.

4.1.3 Density of States (DOS)

4.1.3.1 DOS as Fourier transform of VACF

The density of states (DOS), $g(\omega)$, is obtained from the velocity autocorrelation function (VACF) by a Fourier cosine transform,

$$g(\omega) = \int_0^{\infty} dt C_{vv}(t) \cos(\omega t), \quad (4.20)$$

Noting that $C_{vv}(-t) = C_{vv}(t)$ it follows that

$$g(\omega) = \frac{1}{2} \int_{-\infty}^{+\infty} dt \exp(-i\omega t) C_{vv}(t). \quad (4.21)$$

Equation (4.20) is also called the power spectrum of $C_{vv}(t)$, which is an even function in ω . To understand the physical meaning of this function, consider a sample length τ of the VACF,

$$C_{vv}(t) = \lim_{\tau \rightarrow \infty} \frac{1}{\tau} \int_{-\frac{\tau}{2}}^{\frac{\tau}{2}} dt \mathbf{v}(t) \mathbf{v}(t+t') \quad (4.22)$$

According to the Wiener-Khinchine theorem [Boon & Yip [1991]], the Fourier transformed VACF, $\tilde{C}_{vv}(\omega)$, in limit of $\tau \rightarrow \infty$, equals the mean squared velocity in ω -domain, which is proportional to the frequency spectrum of the kinetic energy,

$$\tilde{C}_{vv}(\omega) = \lim_{\tau \rightarrow \infty} \frac{|\tilde{v}(\omega)|^2}{\tau} \propto E_k(\omega). \quad (4.23)$$

In order to obtain an analytical expression for the DOS in the low frequency region, Eq. (4.9), and $\tilde{C}_{vv}(\omega) = \Re\{\hat{C}_{vv}(i\omega)\}$ are used, where $\tilde{C}_{vv} \equiv g(\omega)$ is the cosine transform of $C_{vv}(t)$ and $\hat{C}_{vv}(s)$ its Laplace transform,

$$g(\omega) = \frac{1}{2} \tilde{C}_{vv}(\omega) \stackrel{\omega \rightarrow 0}{\sim} \frac{D_\alpha}{2} \Gamma(\alpha + 1) \omega^{1-\alpha} \sin\left(\frac{\pi\alpha}{2}\right). \quad (4.24)$$

In case of normal diffusion, $\alpha = 1$, the model derived above, tends for $\omega \rightarrow 0$ to the diffusion constant. In general:

$$D_\alpha = \lim_{\omega \rightarrow 0} \frac{g(\omega) \omega^{(1+\alpha)}}{\Gamma(\alpha + 1) \sin\left(\frac{\pi\alpha}{2}\right)}. \quad (4.25)$$

This alternative expression for D_α is certainly easier to use in practice than Expression (4.5). The Fourier spectra of ensemble averaged MARTINI and OPLS-AA VACFs, Eq. (4.18) were computed only for the 15 ns all-atom and 600 ns NAp_zT coarse-grained simulations (corresponding VACF are nearly identical for both NVT and NAp_zT ensembles).

In order to retrieve the fractional diffusion constant from $g(\omega)$, one has to work with the unnormalized VACFs, where $C_{vv}(0) = \langle \mathbf{v}^2 \rangle$. Here for the MARTINI POPC lipids $\langle \mathbf{v}^2 \rangle = 0.00568 \frac{nm^2}{ps^2}$ and $\langle \mathbf{v}^2 \rangle = 0.00678 \frac{nm^2}{ps^2}$ for the all-atom lipids.

For numerical calculations, the continuous Fourier transform

$$\tilde{C}_{vv}(\omega) = \int_{-\infty}^{+\infty} dt \exp(-i\omega t) C_{vv}(t), \quad (4.26)$$

may be computed via the discrete Fourier transform (DFT) [Brigham [1974]]:

$$\hat{C}_{vv}(k) = \sum_{n=-(N-1)}^{N-1} \exp\left(-2\pi i \frac{kn}{2N-1}\right) C_{vv}(n). \quad (4.27)$$

Here the $C_{vv}(n)$ is defined in range of $n \in (-N+1, N-1)$ and additionally $C_{vv}(n) = C_{vv}(n+l(2N-1))$ for $l \in \mathbb{Z}$, as the DFT implicitly assumes a periodic signal. Here N is the length of the trajectory. Then the approximation of the Fourier integral (4.26) is given by

$$\tilde{C}_{vv}(\omega) \approx \Delta t \hat{C}_{vv}(k), \quad (4.28)$$

where $\hat{C}_{vv}(k) \equiv C_{vv}(k\Delta\omega)$ and $\Delta\omega = 2\pi/(\Delta t(2N-1))$. With increasing number of points, for $N \rightarrow \infty$, the Fourier transform of VACF becomes more and more noisy. For this reason the $\tilde{C}_{vv}(\omega)$ is smoothed by a window function $w(t)$ and then the Fourier spectrum is calculated according to the following integral:

$$\tilde{C}_{vv}^{(w)}(\omega) = \int_{-\infty}^{+\infty} dt \exp(-i\omega t) w(t) C_{vv}(t). \quad (4.29)$$

The smoothing function $w(t)$ is positive and fulfills the conditions,

$$w(0) = 1, \quad (4.30)$$

$$w(t) = w(-t), \quad (4.31)$$

where the first condition conserves the integral of the spectrum

$$\int_{-\infty}^{+\infty} d\omega \tilde{C}_{vv}^{(w)}(\omega) = \int_{-\infty}^{+\infty} d\omega \tilde{C}_{vv}(\omega). \quad (4.32)$$

According to the convolution theorem of the Fourier transform [Brigham [1974]] the

smoothed Fourier transform is then

$$\tilde{C}_{vv}^w(\omega) = \frac{1}{2\pi} \int_{-\infty}^{+\infty} d\omega' \tilde{w}(\omega - \omega') \tilde{C}_{vv}(\omega'). \quad (4.33)$$

In this thesis the Fourier transform is smoothed with a Gaussian function [Harris [1978]]:

$$w(t) = \exp\left(-\frac{1}{2} \left[\frac{t}{\sigma}\right]^2\right) \longleftrightarrow \tilde{w}(\omega) = \sqrt{2\pi}\sigma \exp\left(-\frac{1}{2} [\sigma\omega]^2\right), \quad (4.34)$$

where σ is the width of $w(t)$, which in frequency domain is the inverse of the width in time, and

$$\lim_{\sigma \rightarrow \infty} \frac{\tilde{w}(\omega)}{2\pi} = \delta(\omega). \quad (4.35)$$

One can see that the smoothing becomes stronger if the value of σ decreases. Similarly to Eq. (4.29), the discrete Fourier transform is smoothed by the window function and then Eq. (4.27) simply becomes:

$$\hat{C}_{vv}^w(k) = \sum_{n=-(N-1)}^{N-1} \exp\left(-2\pi i \frac{kn}{2N-1}\right) w(n) C_{vv}(n). \quad (4.36)$$

In this thesis the densities of states were calculated with $\sigma = 10\%$ of the total length of the MD trajectories.

Figure 4.8 shows the comparison between the computed $g(\omega)$ for the coarse-grained (main plot) and the all-atom simulations (inset). In case of the latter the peak is less pronounced and occurs at $\omega \approx 3.5 THz$, whereas for the MARTINI simulation the peak is at $\omega \approx 1.5 THz$. Moreover, $g(\omega)$ is broader for the all-atom simulation.

The fits of Relation (4.24) to the calculated $g(\omega)$ for small angular frequencies are presented in the Fig. 4.9. The choice of the region that would be considered as for small ω is not clearly defined. The final choice of the maximal value of ω defining this region was taken to be smaller than 10% of the calculated maximal frequency ($\omega = 20 THz$),

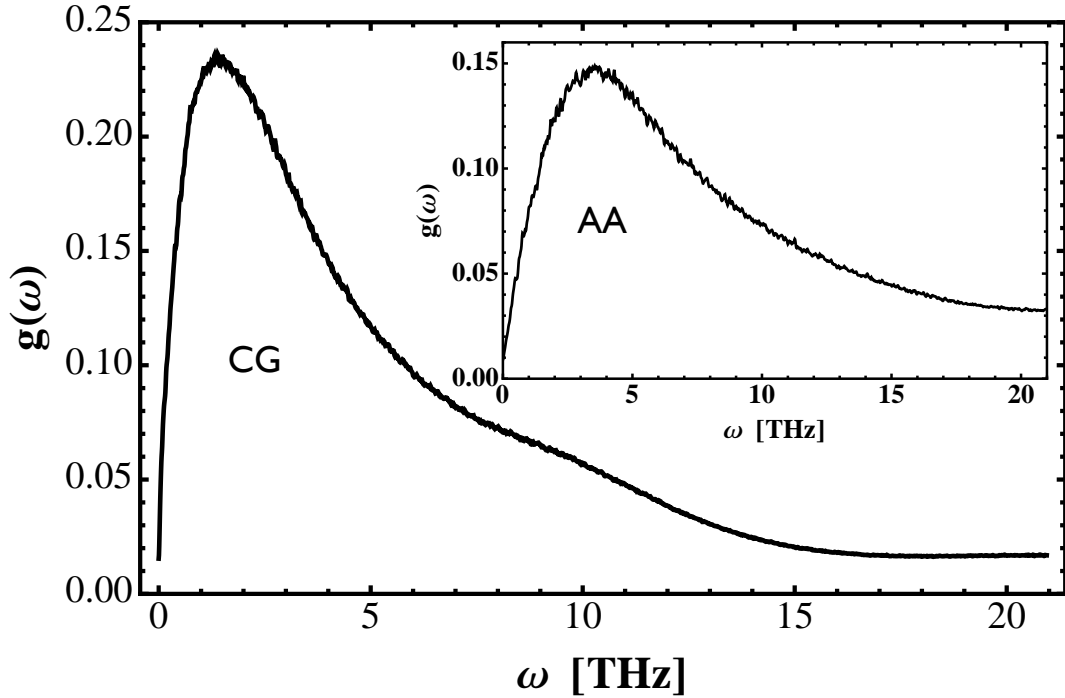


Figure 4.8: Calculated densities of states from the VACFs Fourier transforms for the 600 ns MARTINI simulations (CG) and 15 ns OPLS-AA simulation (AA - the inset).

with a condition that the small frequencies part refers only to ω smaller than the frequency for which the peak in $g(\omega)$ occurs ($\omega \in (0, 1.5 \text{ THz})$ for the coarse-grained calculations and $\omega \in (0, 3.5 \text{ THz})$ for all-atom case). Following this reasoning the fitted parts of the $g(\omega)$ were up to $\omega = 0.6 \text{ THz}$ and $\omega = 2.0 \text{ THz}$ for the MARTINI and OPLS-AA ffs, respectively. The fractional diffusion constants obtained from the fits have values of $0.059 \frac{\text{nm}^2}{\text{ns}^\alpha}$ for the MARTINI and $0.020 \frac{\text{nm}^2}{\text{ns}^\alpha}$ for the OPLS-AA simulations, which are slightly larger than the results from the MSDs fits (Tab. 4.6). The obtained α parameters of 0.437 and 0.467 for the all-atom and the coarse-grained DOS, respectively, are considerably smaller than their MSD counterparts. Especially in case of the former, the α parameter is $\approx 30\%$ lower, which suggests a stronger subdiffusional behavior of the lipids than the

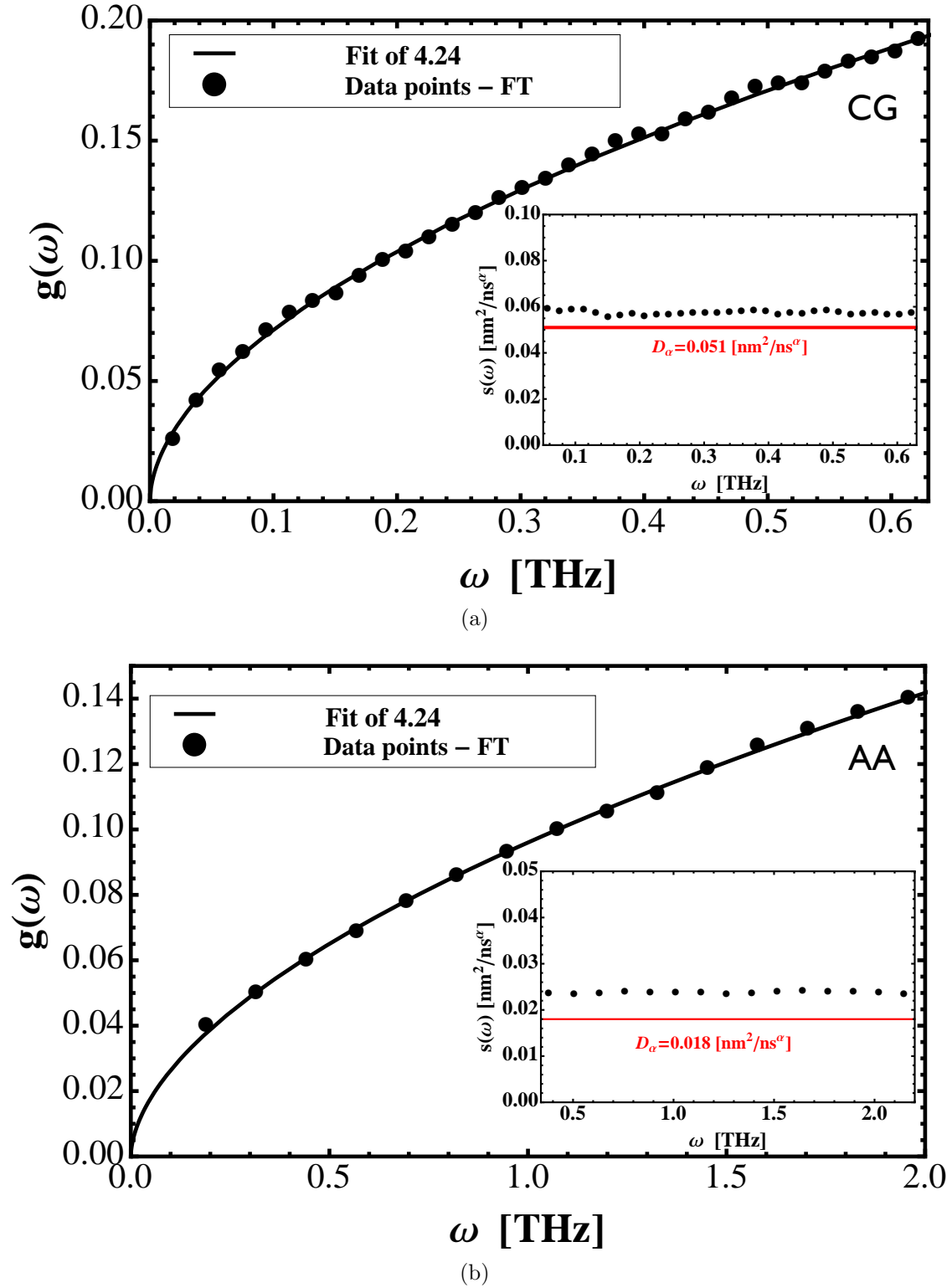


Figure 4.9: Figures show the fits of Expression for the DOS (4.24) for the MARTINI (a) and the OPLS-AA (b) simulations. The insets present values of the function $s(\omega)$, Eq. (4.25), for the α parameters obtained from the fits (the red line is the value of D_α from the MSD calculations).

MSD results indicate. This observation is also true for the MARTINI calculations, for which the α parameter has a very similar value to the α for the OPLS-AA. The calculated $\tau_{vacf} = 0.29 \text{ ps}$ for the OPLS-AA simulation is much higher than the ones computed for the MSD D_α and α parameters ($\tau_{vacf} = 0.065 \text{ ps}$), which implies observation of faster diffusion in the DOS. But, as expected, is smaller than for the $\tau_{vacf} = 0.50 \text{ ps}$ calculated for the MARTINI simulation, which is also higher than the mean $\tau_{vacf} = 0.30 \text{ ps}$ obtained from the MSD. The higher τ_{vacf} for the coarse-grained model than for the all-atom case means smaller friction in the system, according to $\gamma = (\tau_{vacf})^{-1}$. The values of $\gamma = 3.46 \text{ ps}^{-1}$ for the OPLS-AA simulation is higher than for the MARTINI force-field ($\gamma = 2.01 \text{ ps}^{-1}$), which corresponds to broader peak for the DOS in case of the former.

Table 4.6: Comparison between D_α and α parameters for OPLS-AA and MARTINI POPC lipids, obtained from the fit of Eq. (1.4) to the MSDs and of the Eq. (4.24) to the DOS for small ω .

	OPLS-AA		MARTINI	
	MSD	DOS	MSD	DOS
α	0.668	0.437	0.571	0.467
$D_\alpha \text{ (nm}^2/\text{ns}^\alpha)$	0.018	0.020	0.051	0.059

The function $s(\omega)$, Eq. (4.25), in the range of small angular frequencies, should be constant with the mean value close to D_α obtained from the corresponding fits (the insets in the Fig. 4.9). The functions were computed according to Eq. (4.24). The discrepancy to the red line (D_α from MSD) is attributed to the fact that α parameters obtained by the DOS and MSD methods, respectively, do not have the same values.

4.1.3.2 Density of the States from the Autoregressive Model

A discrete approximation of the continuous Fourier transform (4.26), which does not assume periodicity in time, is the infinite sum [Papoulis [1984, 1991]]

$$\tilde{C}_{vv}(\omega) = \Delta t \sum_{n=-\infty}^{+\infty} C_{vv}(n) \exp(-i\omega n \Delta t), \quad (4.37)$$

where $C_{vv}(n) \equiv C_{vv}(n\Delta t)$ and Δt again the sampling interval of the VACF. Then the z -transform of $C_{vv}(n)$, defined as Papoulis [1984, 1991]

$$C_{vv}^z(z) = \sum_{n=-\infty}^{+\infty} C_{vv}(n) z^{-n}, \quad (4.38)$$

is related as follows to Expression (4.37)

$$\tilde{C}_{vv}(\omega) = \Delta t C_{vv}^z(\exp(i\omega \Delta t)). \quad (4.39)$$

Concurrently, the velocity autocorrelation function can be considered in terms of a sample $v_N(n)$ of $v(t)$,

$$C_{vv}(n) \equiv \lim_{N \rightarrow \infty} \frac{1}{2N-1} \sum_{k=-(N-1)}^{N-1} v_N(n+k) v_N(k), \quad (4.40)$$

where the length of the sample is $2N-1$ and it follows from the convolution theorem of the z -transform, (the asterisk denotes a complex conjugate)

$$(f \circ g)(n) \longleftrightarrow F(z)G^*(1/z^*) \quad (4.41)$$

that

$$C_{vv}^z(z) = \lim_{M \rightarrow \infty} \frac{1}{2N-1} V_N(z) V_N^*(1/z^*). \quad (4.42)$$

The z-transform of the an autocorrelation function – here the VACF – can be easily calculated if one assumes an autoregressive model for the time series of the underlying time series [Papoulis [1984, 1991]]

$$v(n) = \sum_{k=1}^M a_k v(n-k) + R(n). \quad (4.43)$$

Here M is the order of the AR process, a_k are constant coefficients and $R(n)$ is white noise with zero mean and autocorrelation $\langle R(n)R(k) \rangle = \sigma_M^2 \delta_{nk}$. The amplitude of the noise $R(n)$ can be determined by using the fact that $R(n)$ is not correlated with past values of $v(n)$, $\langle R(n)v(n-k) \rangle = 0$,

$$\sigma_M^2 = C_{vv}(0) - \sum_{k=0}^M a_k C_{vv}(k), \quad (4.44)$$

Since $R(n)$ is white noise, it is not correlated with the velocity signal for different times. This property can be used to derive the following set of linear equations for the coefficients a_k :

$$C_{vv}(j) = \sum_{k=0}^M C_{vv}(|j-k|) a_k \quad (j = 1, 2, \dots, M) \quad (4.45)$$

Performing now the z-transform of Eq. (4.43) and using the parameters for the autoregressive model, one obtains

$$V_N(z) = \frac{R(z)}{1 - \sum_{k=1}^M a_k z^{-k}}, \quad (4.46)$$

where $R(z)$ is the z-transform of $R(n)$. In the next step the expression above is inserted to Equation (4.42). Using that

$$\lim_{N \rightarrow \infty} \frac{1}{2N-1} R(z) R^*(1/z^*) = C_{rr}(z) = \sigma^2. \quad (4.47)$$

the z -transform of the VACF is found to be [Kneller & Hinsen [2001]]:

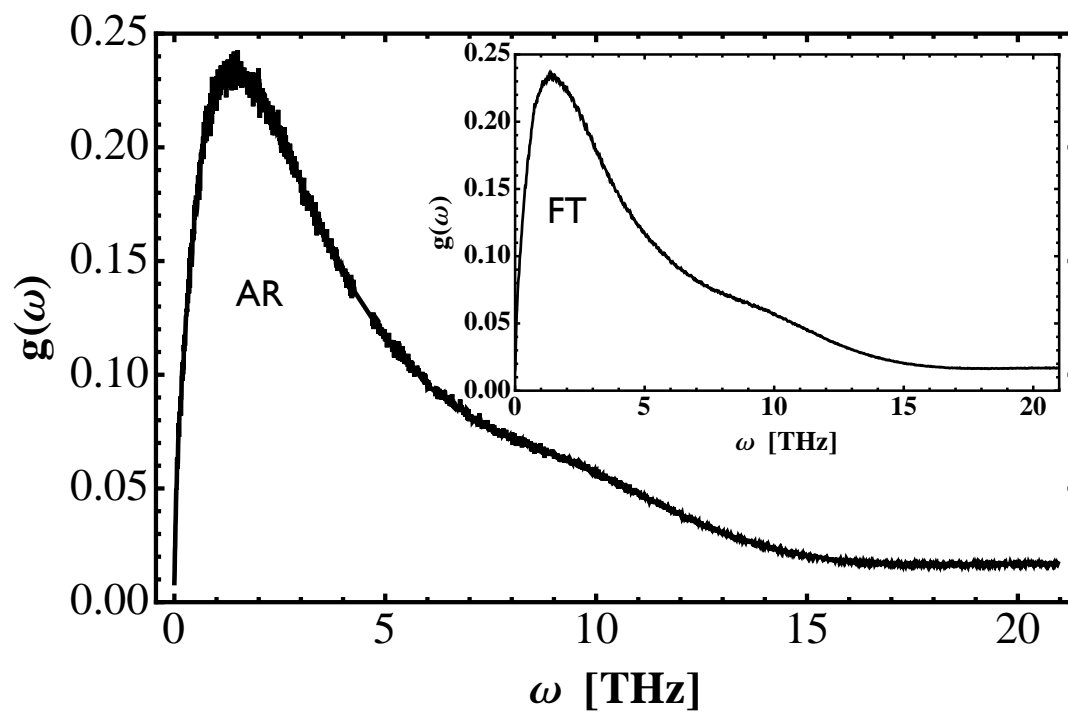
$$C_{vv}^z(z) = \frac{\sigma_M^2}{(1 - \sum_{k=0}^M a_k z^{-k})(\sum_{l=0}^M a_k z^l)} \quad (4.48)$$

Setting $z = \exp(i\omega\Delta t)$, the AR density of states becomes

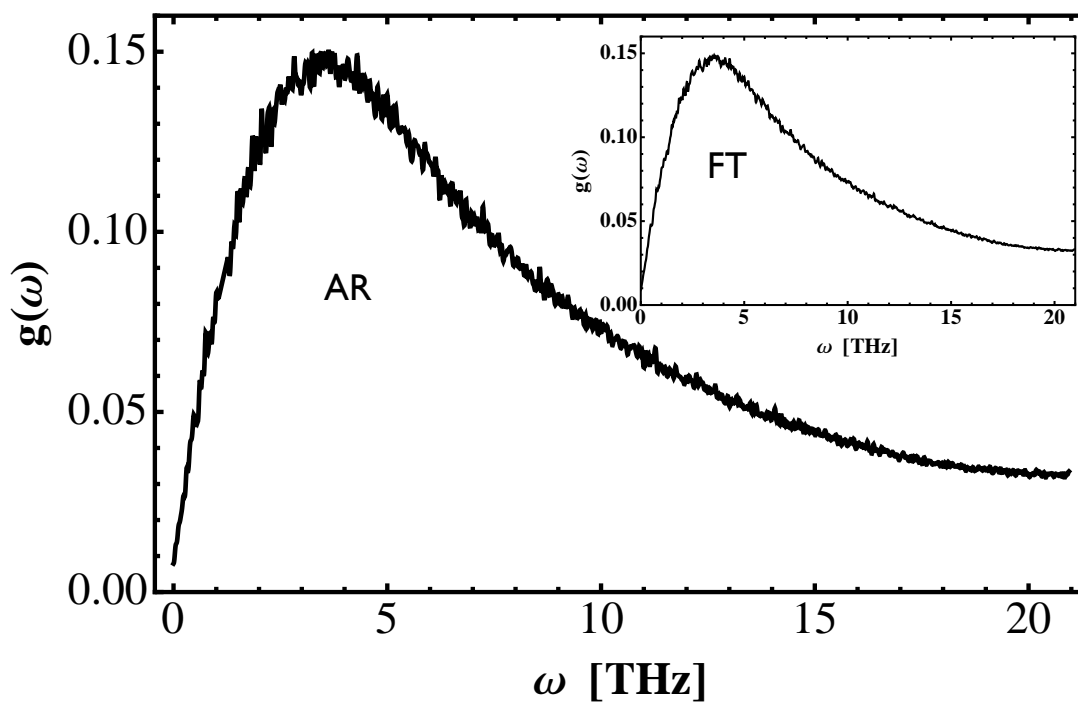
$$g^{AR}(\omega) = \frac{\Delta t}{2} C_{vv}^z \exp(i\omega\Delta t), \quad (4.49)$$

The coefficients of the autoregressive process of order M for the estimation of the densities of states, $g^{AR}(\omega)$, were obtained by solving the linear Yule-Walker equations (4.45) [Walker [1931]; Yule [1927]] with order $M = 666$ for the analysis OPLS-AA simulations and with $M = 3333$ for MARTINI simulations.

The estimated densities of states obtained from the AR model are very similar to those calculated by discrete Fourier transform (see Fig. 4.10). They show in particular the same differences between the DOS of the coarse-grained and the all-atom simulations (Fig. 4.11). In case of the latter the peak is also shifted to $\approx 3.5 THz$ (for CG $\approx 1.5 THz$). In Fig. 4.12 are presented the fits of Relation. 4.24 to the estimated $g(\omega)$ from the MARTINI (Fig. 4.12a) and OPLS-AA simulations. Stronger fluctuations of the $g(\omega)$ can be seen for both cases, but the characteristic curves of the DOS for subdiffusion are preserved. The fitted fractional diffusion constants and the α parameters are very close to the computed values from the Fourier transformed VACFs (Table 4.7). This is in particular true in case of the coarse-grained calculations, for which the D_α have exactly the same values of $0.059 \frac{nm^2}{ns^\alpha}$. The α parameters are practically the same and the α -parameters for the all-atom simulations obtained from the AR model and by classical Fourier transform are also very close. On the other hand, $D_\alpha = 0.023 \frac{nm^2}{ns^\alpha}$ overestimates the lateral diffusion of the POPC lipids even somewhat stronger compared to the analysis with the Fourier



(a)



(b)

Figure 4.10: The figures show the densities of states for MARTINI (a) and OPLS-AA (b) estimated by AR model. In the insets are presented the results of the FT method for comparison.

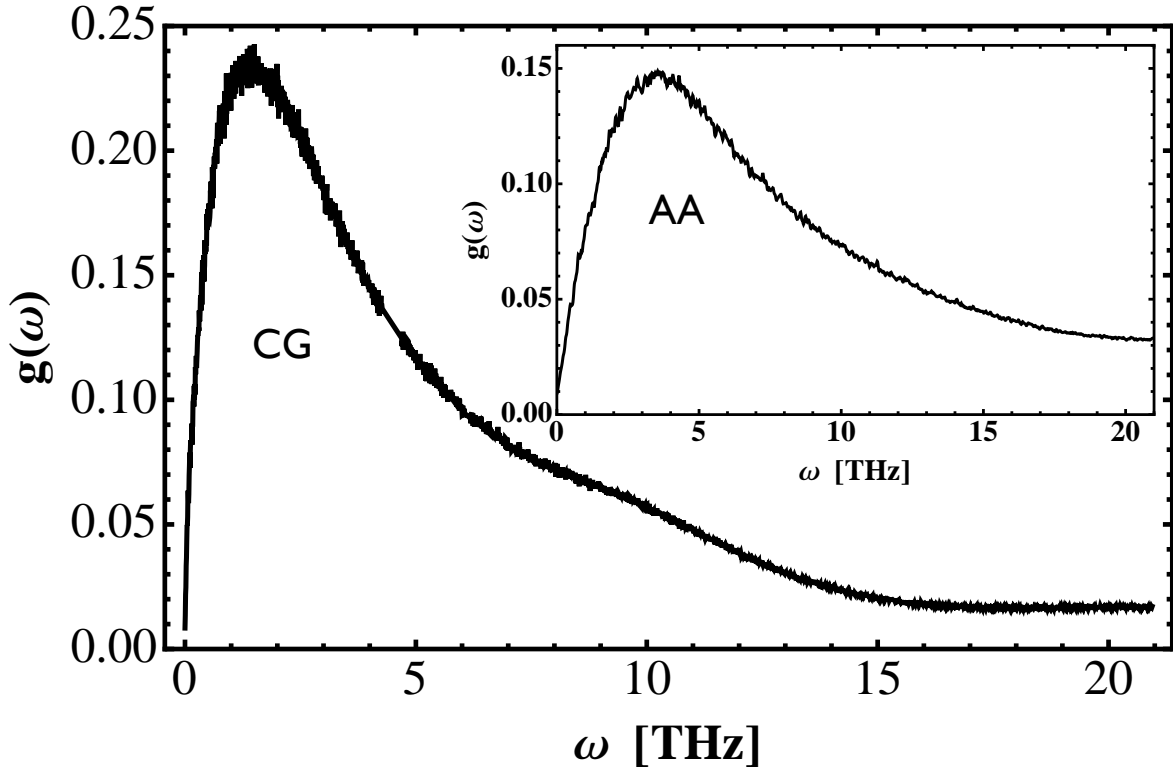
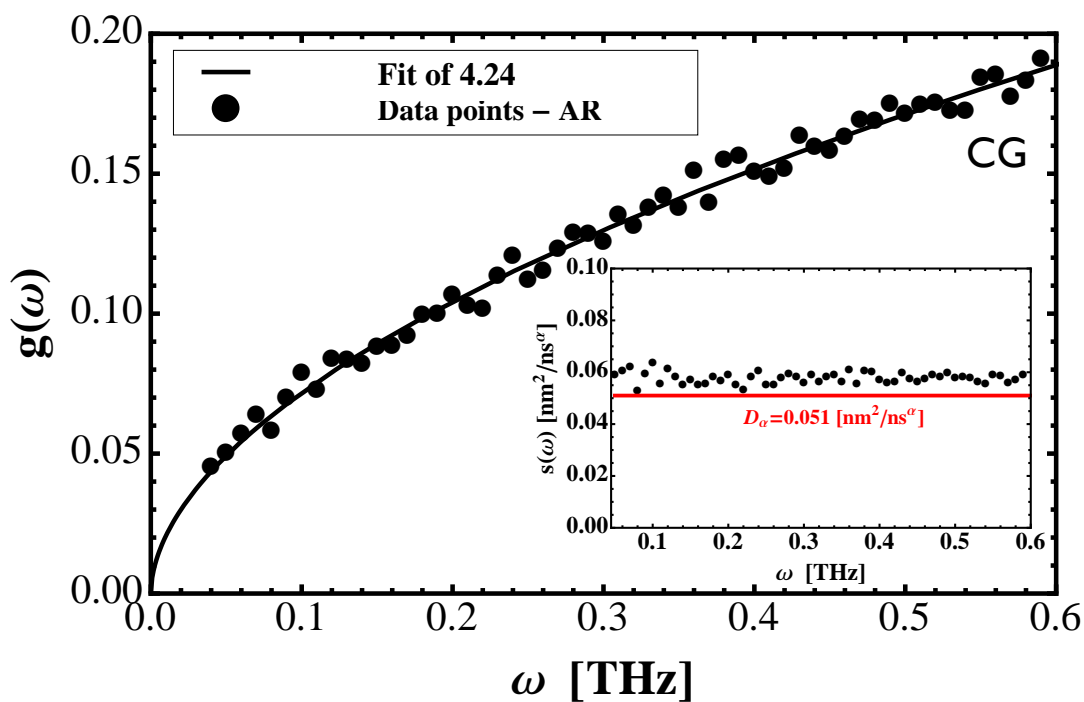
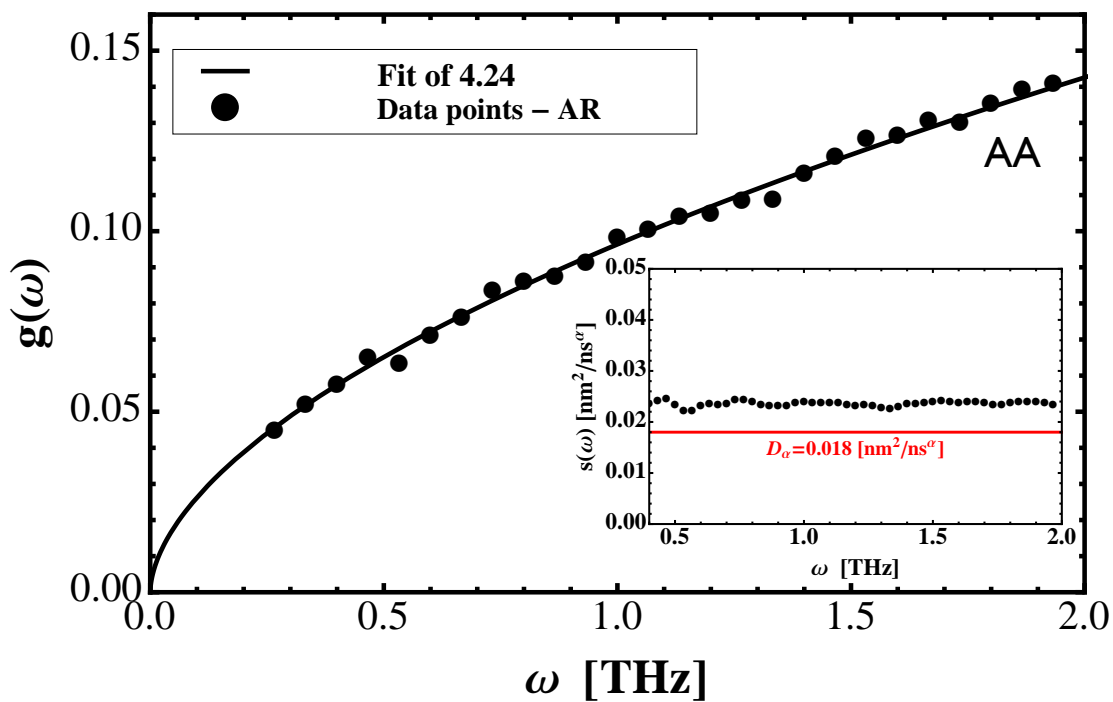


Figure 4.11: Comparison of estimated densities of states by the autoregressive model (AR) for the 600 ns MARTINI simulations (CG) and 15 ns OPLS-AA simulation (AA - the inset).

transform method. Nevertheless, $\tau_{vacf} = 0.33$ ps and $\gamma = 3.04$ ps⁻¹ for the OPLS-AA force-field and $\tau_{vacf} = 0.50$ ps and $\gamma = 1.99$ ps⁻¹ for the MARTINI force-field obtained from the AR model are very close to the FT calculations, which shows that both methods give nearly identical results.



(a)



(b)

Figure 4.12: Figures show the fits of Eq. (4.24) to the autoregressive DOS for the MARTINI (a) and OPLS-AA (b) simulations. The insets compare the evolution of $s(\omega)$ with the value of D_α obtained from the MSD fits.

Table 4.7: Comparison between D_α and α parameters for OPLS-AA and MARTINI simulations obtained from the fit of Eq. (1.4) to the MSDs and of Eq. (4.24) to the DOS for small ω . The DOS-FT means the $g(\omega)$ calculated by the Fourier transform and DOS-AR for $g(\omega)$ computed within the AR process.

	OPLS-AA			MARTINI		
	MSD	DOS-FT	DOS-AR	MSD	DOS-FT	DOS-AR
α	0.668	0.437	0.429	0.571	0.467	0.466
D_α (nm^2/ns^α)	0.018	0.020	0.023	0.051	0.059	0.059

4.1.4 Conclusions

In this chapter a single molecular dynamics of the OPLS all-atom and MARTINI coarse-grained POPC lipids was presented. The MD trajectories were analysed in terms of the mean square displacements, velocity autocorrelation functions and the densities of states. All the proposed models clearly show that the movements of POPC lipids within model membrane exhibit a subdiffusive characteristics, within the accuracy of the analysis. The analyses of the MSDs predict an α parameter of ≈ 0.7 and ≈ 0.6 for the OPLS-AA and MARTINI simulation, respectively. The analyses of the DOS indicate a stronger subdiffusive characteristics, with α parameter of ≈ 0.4 . The independent estimation of DOS using autoregressive process confirms the results for $g(\omega)$, obtained by the Fourier transform of the velocity autocorrelation function.

4.2 Collective motions of lipids

In contrast to the earlier chapter, which covered the single molecular dynamics, this chapter concentrates solely on the collective motions of POPC lipids in the plane of model membrane. The main goal is to visualize the cage of nearest neighbors of a tagged diffusing

particle. This subject will be presented in terms of spatio-temporal density fluctuations within the simulated POPC membranes.

4.2.1 Pair Correlation Function

Structural and dynamical correlations in condensed matter systems are described by the van Hove correlation function [Van Hove [1954]]

$$g^{(VH)}(\mathbf{r}, t) = \frac{1}{N} \sum_{\alpha, \beta=1}^N \langle \delta(\mathbf{r} - [\mathbf{R}_\beta(t) - \mathbf{R}_\alpha(0)]) \rangle \quad (4.50)$$

where $\mathbf{R}_\alpha(t)$ is the position of particle α , which is the center of mass of a lipid molecule in the context of this thesis. The van Hove correlation function plays a fundamental role in the interpretation of neutron and light scattering experiments on liquids and colloids [Bée [1988]; Berne & Pecora [2000]; Lovesey [1984]]. It splits into a self- and a distinct part,

$$g^{(VH)}(\mathbf{r}, t) = g_S^{(VH)}(\mathbf{r}, t) + g_D^{(VH)}(\mathbf{r}, t), \quad (4.51)$$

where

$$g_S^{(VH)}(\mathbf{r}, t) = \frac{1}{N} \sum_{\alpha=1}^N \langle \delta(\mathbf{r} - [\mathbf{R}_\alpha(t) - \mathbf{R}_\alpha(0)]) \rangle, \quad (4.52)$$

$$g_D^{(VH)}(\mathbf{r}, t) = \frac{1}{N} \sum_{\alpha \neq \beta=1}^N \langle \delta(\mathbf{r} - [\mathbf{R}_\beta(t) - \mathbf{R}_\alpha(0)]) \rangle. \quad (4.53)$$

The distinct part describes is of interest in the following since it quantifies the structural correlations in the system under consideration. One verifies easily that its spatial average

over the volume V of the system yields the mean particle density, $\rho = N/V$, for large N ,

$$\frac{1}{V} \int_V dV g_D^{(VH)}(\mathbf{r}, t) = \frac{N-1}{V} \approx \rho. \quad (4.54)$$

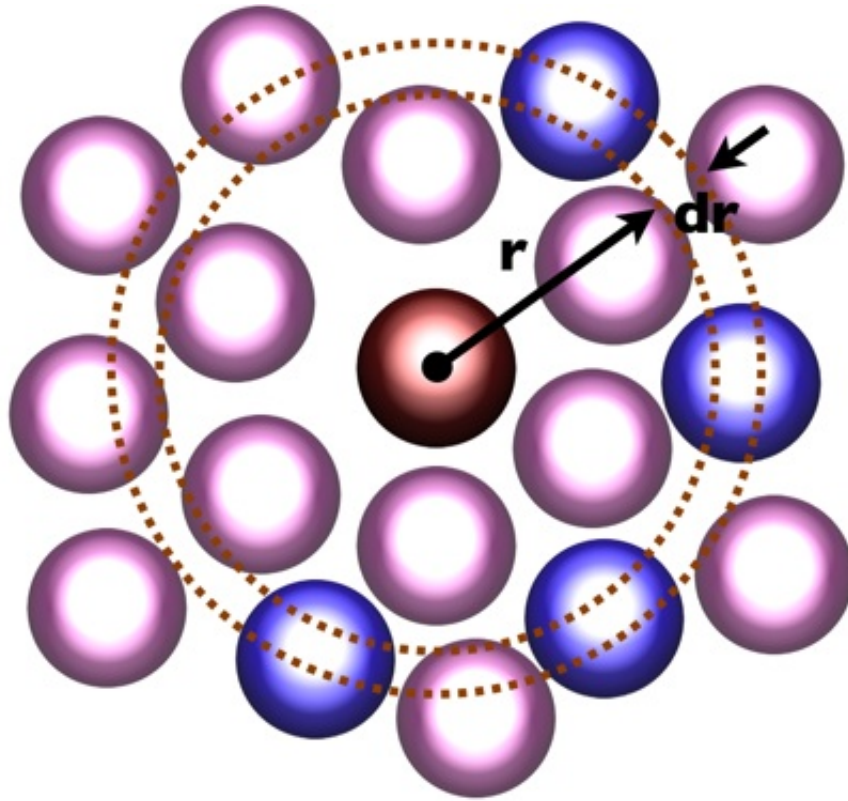


Figure 4.13: The schematic visualising the definition of the pair distribution function¹¹.

This motivates the definition of the time-dependent pair correlation function through

$$G_D(r, t) = \frac{1}{\rho} \frac{1}{\Delta V_r} \int_{\Delta V_r} dV g_D^{(VH)}(\mathbf{r}, t), \quad (4.55)$$

¹¹Source : Adapted from D.S. Goodsell, Trends Biochem. Sci. 16:203-206, 1991.

where ΔV_r is the volume of a spherical shell of thickness Δr and $r = |\mathbf{r}|$. (see Fig. 4.13). As r tends to infinity, the spatial correlations between the position of a tagged central particle α and the partner particles β decay and therefore their density in the shell between r and $r + \Delta r$ approaches the mean density, ρ , such that

$$\lim_{r \rightarrow \infty} G_D(r, t) = 1. \quad (4.56)$$

The static pair correlation function is obtained through

$$g(r) = G_D(r, 0). \quad (4.57)$$

In order to elucidate the time-dependent structural correlations in the POPC lipid membranes, $G_D(r, t)$ is computed for the centers-of-mass of the lipid molecules, by binning, according to Eq. (4.55), the (normalized) density of partner lipids β around each lipid molecule α in concentric rings of thickness Δr and averaging the resulting histograms over all central particles α .

4.2.2 Visualization of the cage effect

The lateral time-dependant pair correlation functions, $G_D(r, t)$ were calculated according to Eq. (4.55) choosing a maximal time lag of 10% of the respective trajectory length. For comparison, a similar analysis, but in three dimensions, was performed for the bulk SPC/E water system simulated for 1 ns in NVT ensemble. The biggest radius value was set to be smaller than half the box length in either x or y direction for the all-atom POPC lipids, i.e. 4.4 nm, with the radial step, Δr , of 0.1 nm. The same parameters were used for the MARTINI simulations. For the water the maximal radius was 2.0 nm, which was less than half the edge of cubic simulation box, with $\Delta r = 0.01 \text{ nm}$.

The distinct time-dependant pair correlation functions, $G_D(r, t)$, for the all-atom and the

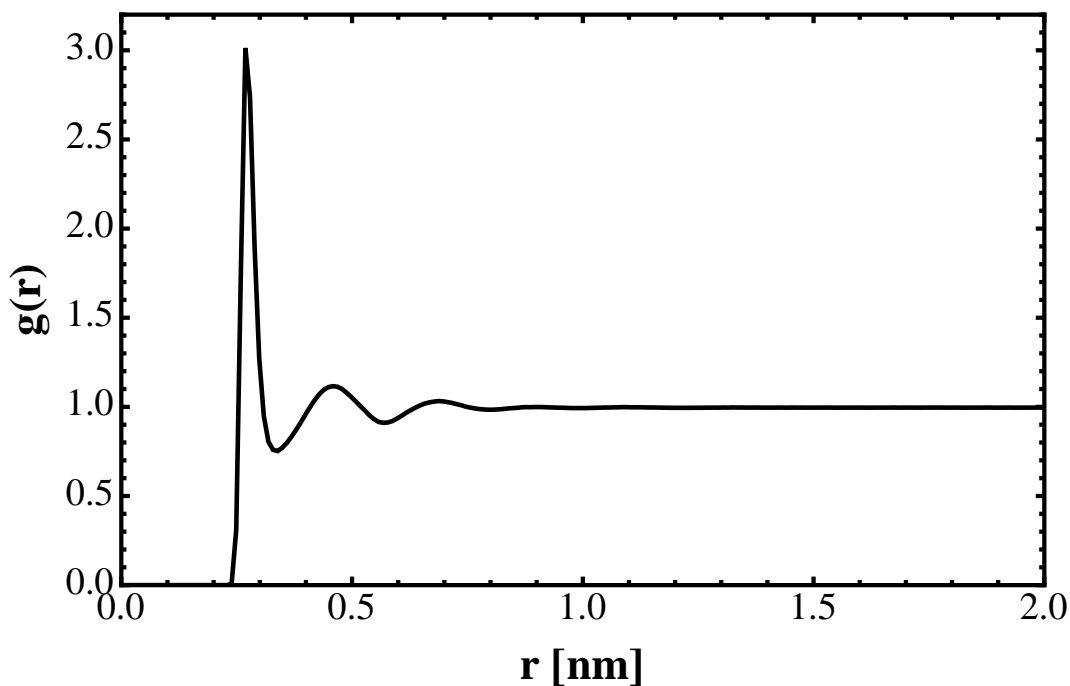
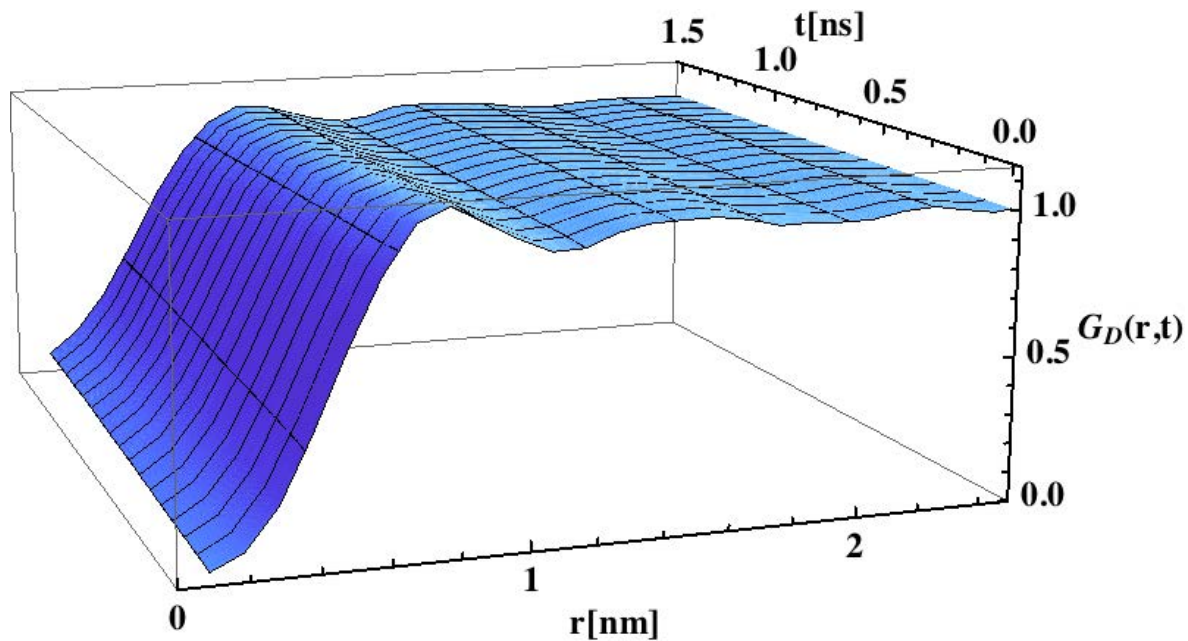


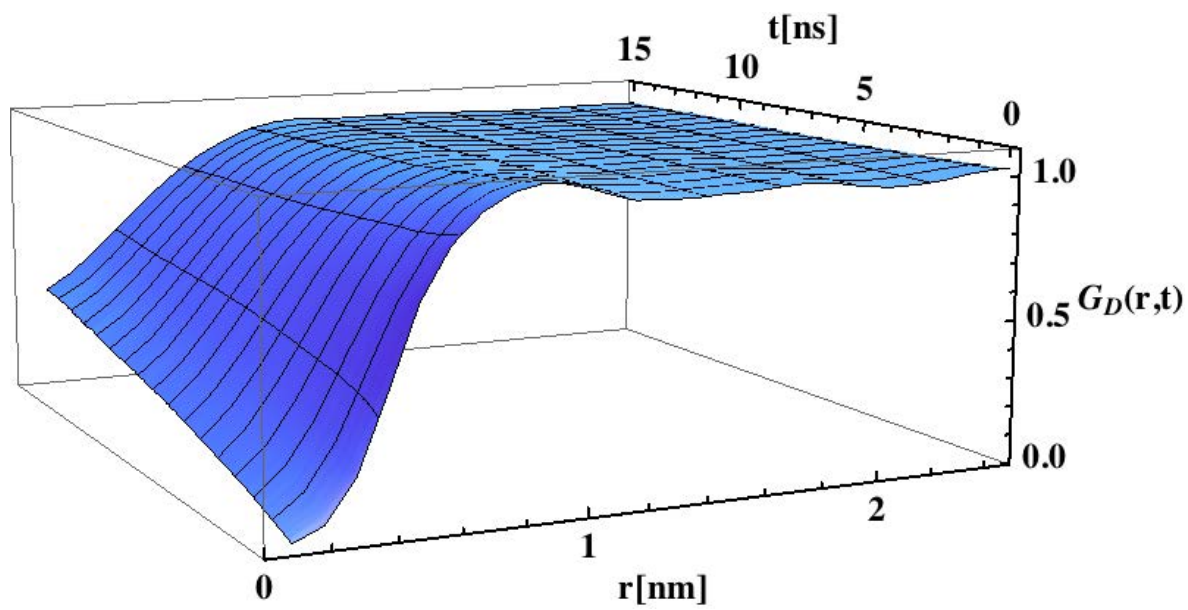
Figure 4.14: The pair distribution function, $g(r)$, for the bulk SPC/E water.

coarse-grained simulations are shown in three dimensional plots in Figs. 4.15 and 4.16, respectively. The first peak of the $G_D(r, t)$ at $r = 0.8 \text{ nm}$, corresponds to the first shell of neighbors surrounding each POPC lipid. It is visible that the peaks decay slowly and the general structure of the shell is preserved until reaching the mean density. This behavior of the $G_D(r, t)$ differs strongly from the results for the simulated bulk SPC/E water (Fig. 4.17). In case of the latter, the first shell of neighbors decays much more rapidly. Figure 4.18 shows the decay of the first peak for three time slices (time-lags) in case of the OPLS-AA 15 ns (4.18a) and 150 ns (4.18b) simulations. The first time slice, for $t = 0$, is the pair distribution function (solid line).

For the 15 ns simulation the maximal calculated time-lag was for 1.5 ns and in the figure (dotted line) it is noticeable that around this value the $G_D(r, t)$ reaches the mean density.

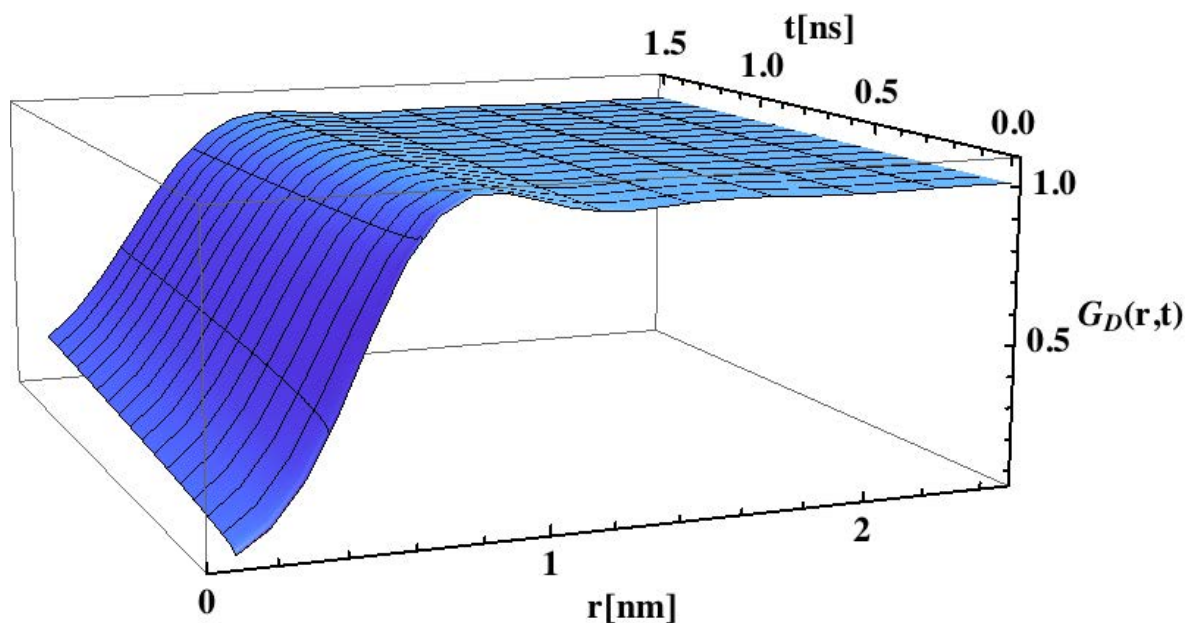


(a)

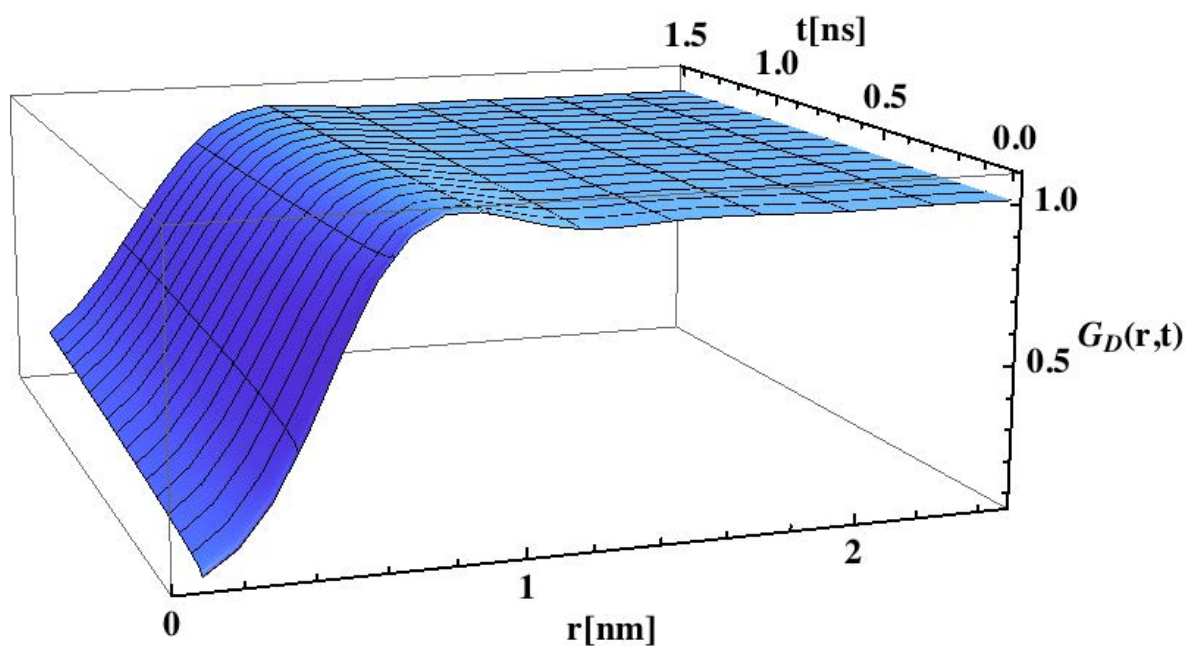


(b)

Figure 4.15: Three dimensional plots of the distant time- dependant pair correlation functions, $G_D(r,t)$, for the all-atom POPC 15 ns (a) and 150 ns (b) simulations.



(a)



(b)

Figure 4.16: 3D plots of the $G_D(r,t)$, for the 600 ns NVT (a) and $N_{Apz}T$ (b) MARTINI simulations.

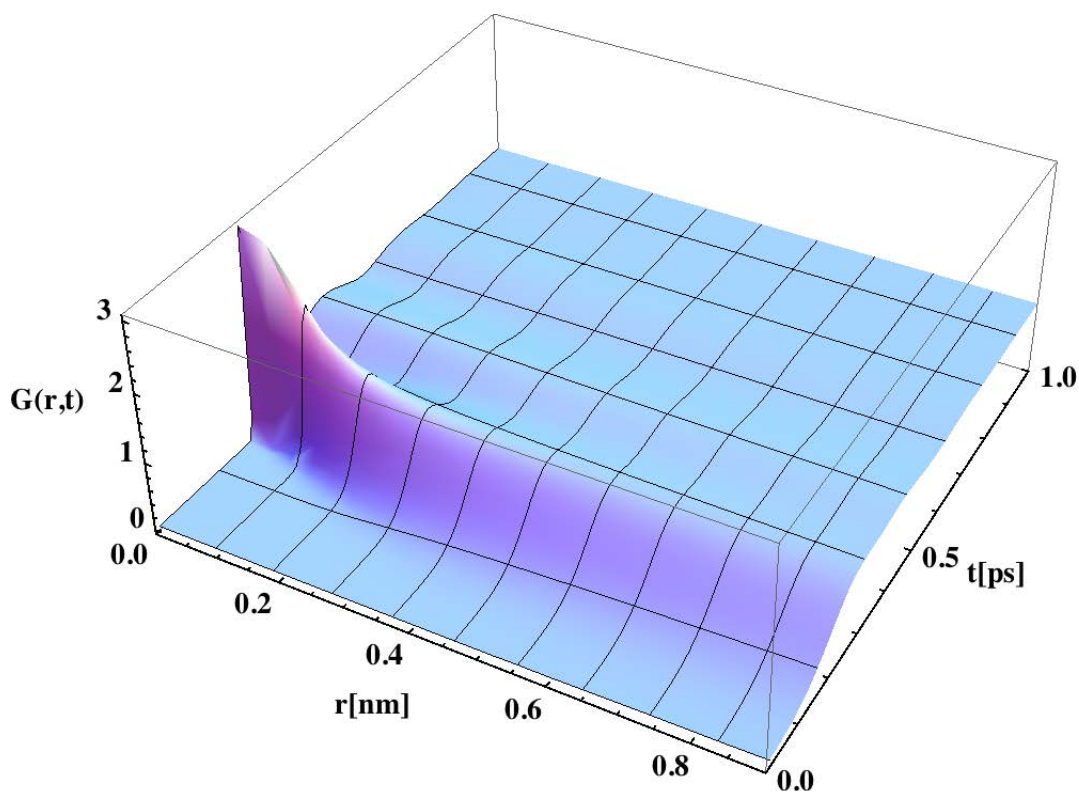
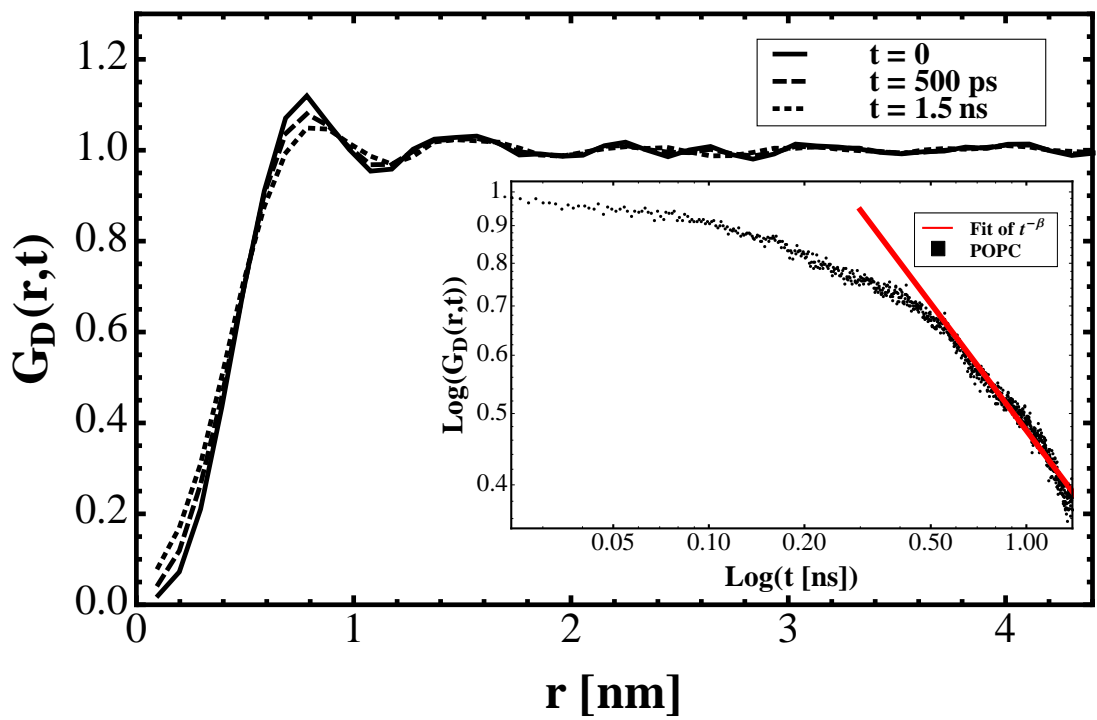
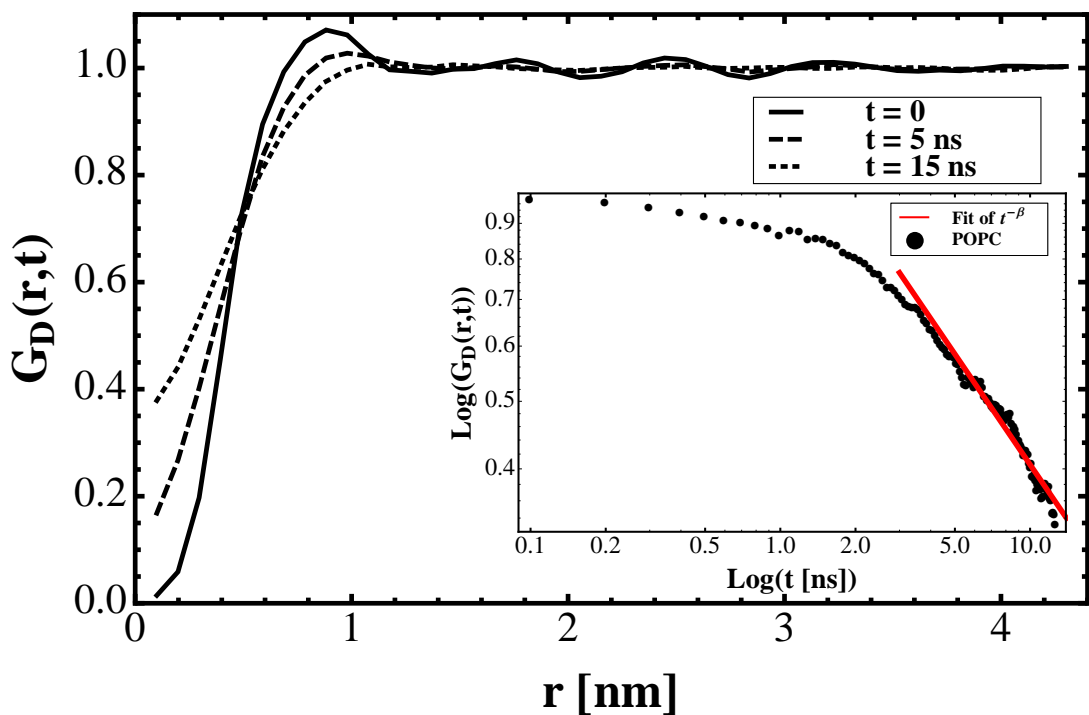


Figure 4.17: 3D plot of the computed $G_D(r,t)$ for the simulated bulk SPC/E water.

In case of the 150 ns simulation the functions starts to reach the mean density around 10 ns, and the function finally reaches the mean density around 15 ns (dotted line). These results show the persistence of the cage of nearest neighbors by the POPC molecules. The density correlations are strong, which leads to maintaining the structure of the first shell of neighbors. This observation contrasts strongly with results for the simulated bulk SPC/E water, presented in Fig. 4.19. The decorrelation of the $G_D(r,t)$ is not only more rapid – the first peak vanishes already after 1.5 ps (dotted line) – but also the character of this decay is different than for the POPC lipids, which was already visible in Fig. 4.17. It is worth noticing that the computed pair distribution function for $t = 0$ (solid line), matches very well known molecular dynamics results [Rahman & Stillinger [1971]; Sciortino *et al.* [1996]]. Moreover the first peak at $r = 0.2$ nm agrees with experimentally measured pair



(a)



(b)

Figure 4.18: Plots show the calculated $G_D(r,t)$ of the OPLS-AA 15 ns (a) and 150 ns (b) simulations for three time-lags. Visible slow time decay of the first shell of neighbours in long time-tail analysis, the log-log plots in the insets, indicate power-law behavior.

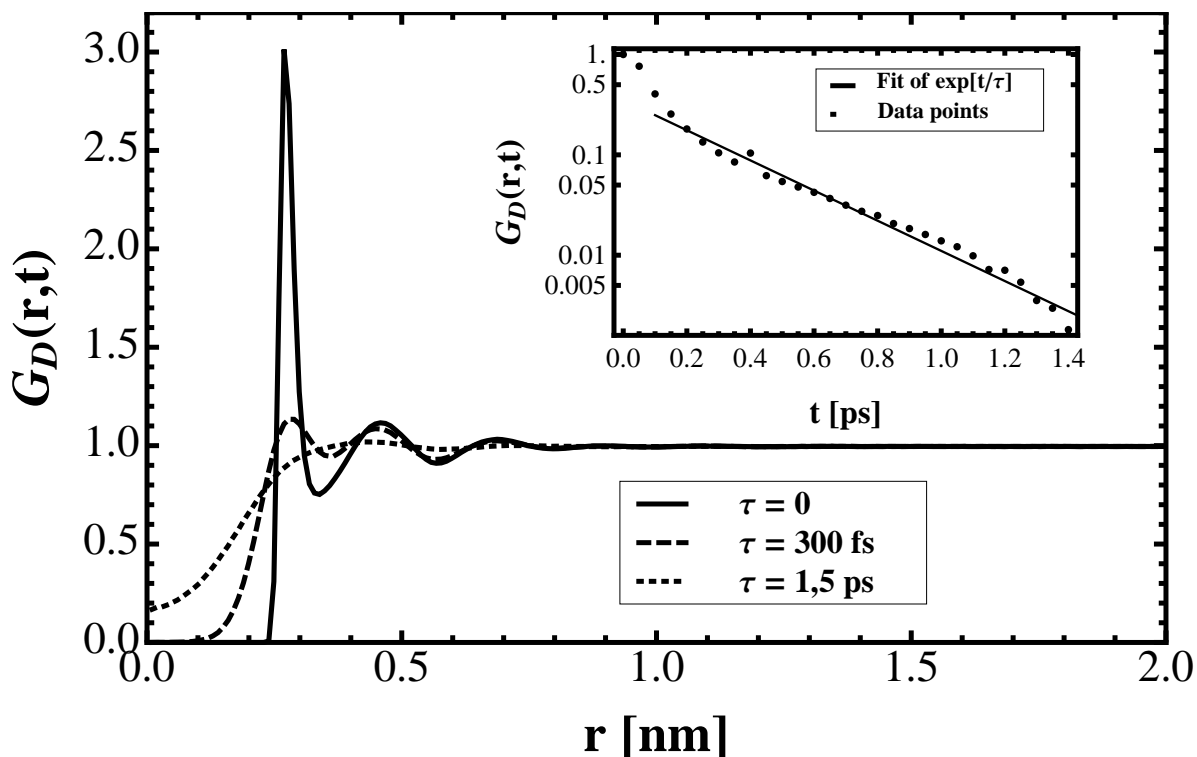
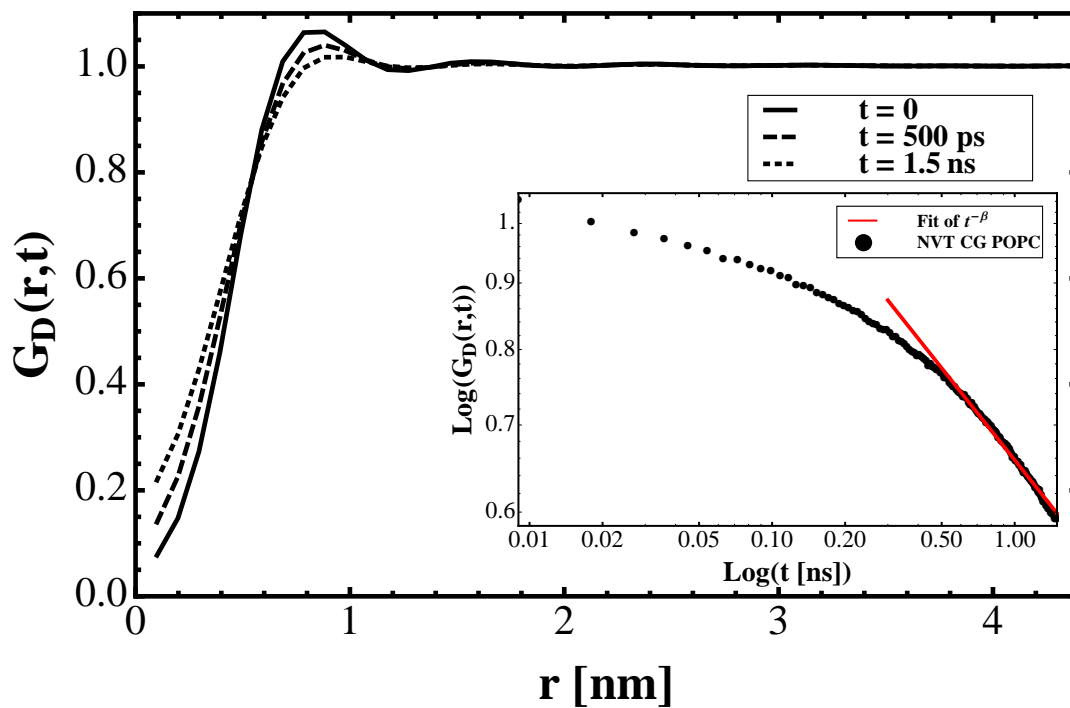


Figure 4.19: Pair correlation function for the centre of mass of SPC/E water molecules for three time slices : $t = 0$ (solid line), $t = 300$ fs (dashed line) and $t = 1.5$ ps (dotted line). The first shell of neighbours, in log plot shown on the inset, decays rapidly and exponentially.

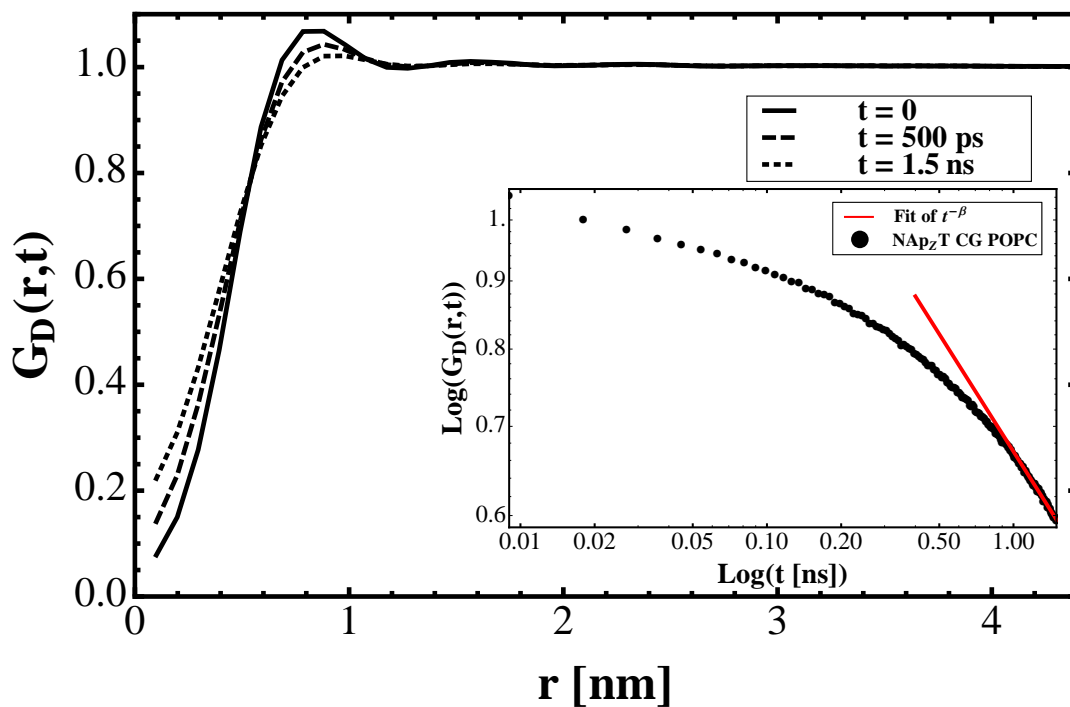
correlation function for a bulk water [Narten [1971]].

In order to further investigate the nature of motions in the all-atom POPC bilayer, the time decay of the first shell of neighbors was analysed, by taking into account only their long-time behavior. The insets in Fig. 4.18 show log-log plots of the $G_D(r, t)$ values for the first peak in function of time. The long-time part, chosen from 400 ps for the 15 ns and from 3ns for the 150 ns simulations, shows a power-law decay dependency. A corresponding function was fitted to the data points,

$$G_D(t) = At^{-\beta}. \quad (4.58)$$



(a)



(b)

Figure 4.20: The $G_D(r, t)$ of the MARTINI *NVT* (a) and *NAP_zT* (b) simulations for three time lags : $t = 0$ (solid line), $t = 500$ ps (dashed line) and $t = 1.5$ ns (dotted line). Similarly to the all-atom case, the long-time tails (the insets) decay as a power-law.

The fitted values of $\beta = 0.573$ and $\beta = 0.526$, for the OPLS-AA simulations of 15 ns and 150 ns, respectively, show clearly the power-law decay of the first peak in $G_D(r, t)$ (see Table 4.8). Since the first peak in $G_D(r, t)$ corresponds to the shell of nearest neighbors, its slow power-law decay for POPC molecules indicates that each molecule moves essentially for long time with its neighbors. For comparison, the corresponding analysis for water is shown in the inset of Fig. 4.19. Here one observes an exponential decay and thus a much less stable cage of nearest neighbors. The form of the decay is here more important than the time scale.

Table 4.8: Comparison between the fit parameters of Eq. (4.58) to the long-time tail of computed $G_D(r, t)$ for the OPLS-AA and MARTINI simulations.

	OPLS-AA		MARTINI	
	15ns	150ns	NVT	NAp_zT
β	0.573	0.307	0.235	0.244
A	0.474	1.125	0.658	0.663

A similar analysis was performed for the MARTINI NVT and NAp_zT simulations (Fig. 4.20). The calculated $G_D(r, t)$ functions reach the mean density already after 1.5 ns (dotted line). This can be expected by looking at the velocity autocorrelation functions for the coarse-grained simulations (Fig. 4.6). In comparison to the all-atom VACFs, the observed minimum of the C_{vv} is less pronounced, which corresponds to a weaker cage effect and which is consistent with a faster decay of the cage of the nearest neighbors. The analyses of the time decay of the first peak of the $G_D(r, t)$ (insets in Fig. 4.20), show again a power-law decay with $\beta = 0.235$ and $\beta = 0.293$ for the NVT and NAp_zT simulations,

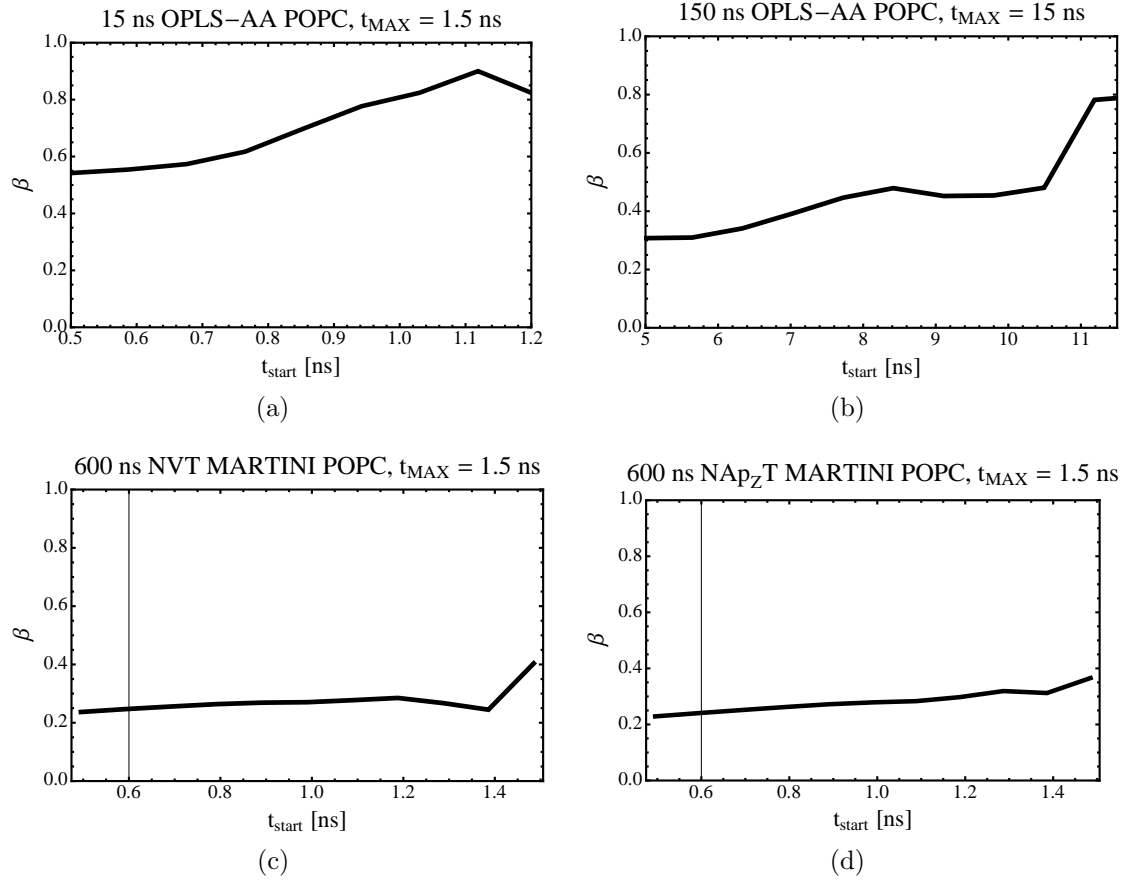


Figure 4.21: Figures show the β parameter dependence on the time-lag, defining the beginning of the $G_D(r, t)$ long-time tail for the simulations : (a) 15ns OPLS-AA, (b) 150 ns OPLS-AA, (c) 600 ns *NVT* MARTINI and (d) 600 ns *NAp_zT* MARTINI. The maximal time-lag for which the $G_D(r, t)$ functions were computed is denoted by t_{MAX} .

respectively. The β parameters are, however, nearly twice smaller than for the all-atom simulations and similar for both thermodynamic ensembles. The choice of the time range for the fits of Expression (4.58) is, of course, debatable. Figure 4.21 shows the dependence of the β -parameter on the initial time t_{start} for the fit interval. The fitted values are relatively stable for t_{start} up to 70 % and to 90 % of the maximal analysed time-lags for the OPLS-AA and MARTINI simulations, respectively.

4.2.3 Conclusions

In this chapter the analysis of the local structure dynamical structure around each lipid molecule in a POPC membrane was analyzed by analyzing the behavior of the lateral time-dependent pair correlation functions. They reveal a persisting cage of the first shell of neighboring lipids (for over 15 ns in case of the 150 ns OPLS-AA simulation), which are consistent with the observed negative long-time tails of the calculated VACFs. The analyses of the long-time tails of the first peaks of the $G_D(r, t)$, exhibit a power-law decay, with $\beta \approx 0.55$ and $\beta \approx 0.25$ for the all-atom OPLS and the coarse-grained MARTINI simulations, respectively. These results contrast strongly with findings for the bulk SPC/E water, for which the first shell of neighbors vanishes rapidly (already after 1.5 ps) and, moreover, exponentially.

The existence of the cage effect in POPC lipid membrane for long correlation times is in good agreement with molecular dynamics simulations findings of concerted movements in lipid bilayers, forming so-called "collective flow patterns" [Falck *et al.* [2008]].

The connection between the α -parameter describing the long-time behavior of the MSD, Eq. (1.4) and the β -parameter describing the slow decay in the first peak of $G_D(r, t)$ is not yet established.

Chapter 5

Conclusions

The main goal of this thesis was to characterize the nature of the lateral movements of lipids within a model membrane. For this purpose a series of molecular dynamics simulations of a 1-palmitoyl-2-oleoylphosphatidylcholine (POPC) lipid bilayer was conducted with the all-atom (OPLS) and the coarse-grained (MARTINI) force fields. An all-atom energetically equilibrated POPC membrane of 274 lipids in total was simulated for 15 ns and 150 ns in full hydration. The equilibration process had several intermediate steps, which account for the total simulation time of 230 ns, and the 150 ns simulation was an extension to the 15 ns one. The systems were considered to be in equilibrium when the fluctuations of the total energy and the average area per lipid were stable, with the value of the latter being close to the experimental ones. In order to have access to longer time scales and larger system sizes, simulations of 600 ns for a system of 2033 lipid molecules were conducted with the MARTINI force field, using the NVT and the NAp_zT ensemble. In the latter ensemble the pressure was adjusted only in the direction perpendicular to the bilayer. The production runs for both ensembles were performed after energy equilibration simulations of 1.2 μs . The MARTINI force-field calculations were also used to test the ability of coarse-grained models to reproduce dynamical properties of all-atom simulations.

The lateral diffusion of the lipid molecules was analyzed using different physical quantities and numerical methods. For all simulations, the time evolution of the computed molecular mean square displacements (MSDs) showed clear deviations from the asymptotic linear form which characterizes normal diffusion. The fits of the relation for the MSD gave average α parameters of ≈ 0.69 and ≈ 0.55 for the OPLS-AA and MARTINI simulations, respectively. The observed diffusion of POPC lipids was 6-8 times faster for the MARTINI simulations than for the OPLS-AA, which is also coherent with publications showing that in general the diffusion constants obtained from the MARTINI simulations are several times higher than the experimental values. The MSD results are consistent with the analyses of the VACF power spectra, which were calculated with two different methods: (a) by a windowed discrete Fourier transform of the VACF, and (b) by fitting an autoregressive model to the underlying velocity time series. For both OPLS-AA and MARTINI, the corresponding α -parameters were, however, slightly smaller than those obtained from the analyses of the MSDs. Similarly to the MSD analysis, the diffusion of the coarse-grained lipids was faster than the diffusion of the all-atom ones. The so-called cage effect, which manifests itself by negative algebraic long-time tails in the VACFs, was further analyzed by examining the time-dependent local structure around each lipid molecule by means of the time-dependent pair correlation function. The first peak of the latter exhibits a slow power-law decay, indicating that the local cage formed by the shell of nearest neighbors decays very slowly. This is a direct physical manifestation of the cage effect, which is suggested by the negative long-time tails of the VACF. The persistence of the local structure is in agreement with flow-like dynamical patterns in membranes, which have been observed recently by other authors [Falck *et al.* [2008]]. The comparison of the simulations with the all-atom OPLS and the coarse-grained MARTINI force field showed clearly that both exhibit subdiffusion, with similar α -parameters, but the latter is several times faster. In agreement with these findings, the molecular VACFs exhibit a more shallow minimum and the cage of nearest neighbors of the lipid molecules decays

faster. These observations can be attributed to the fact that the coarse-grained representation of the lipid molecules in the MARTINI force field leads to less interactions with the neighbors and thus to less entanglement.

Chapter 6

Publications

Hinsen, K., Pellegrini, E., Stachura, S., Kneller, G. R. (2012). nMoldyn 3: Using task farming for a parallel spectroscopy-oriented analysis of molecular dynamics simulations. *Journal of Computational Chemistry*, 33(25), 2043–2048. doi:10.1002/jcc.23035

Stachura, S., Kneller, G. R. (2013). Anomalous lateral diffusion in lipid bilayers observed by molecular dynamics simulations with atomistic and coarse-grained force fields. *Molecular Simulation*, 40(1–3), 245–250. doi:10.1080/08927022.2013.840902

Stachura, S., Kneller, G. R. A simple model for the velocity autocorrelation function of lipids in a model membrane *In preparation*.

Stachura, S., Kneller, G. R. The impact of spatio-temporal density fluctuations on subdiffusive molecular motions in lipid bilayers. *In preparation*.

References

- Alberts, Bruce, Bray, Dennis, Johnson, Alexander, Lewis, Julian, Raff, Martin, Roberts, Keith, & Walter, Peter. 2005. *Essential cell biology*. Second polish edition edn. PWN SA. [v](#), [1](#)
- Alder, B J, & Wainwright, T E. 1957. Phase Transition for a Hard Sphere System. *The Journal of Chemical Physics*, **27**(5), 1208. [xviii](#), [17](#)
- Alder, B J, & Wainwright, T E. 1959. Studies in Molecular Dynamics. I. General Method. *The Journal of Chemical Physics*, **31**(2), 459. [xviii](#), [17](#)
- Allen, M P, & Tildesley, D J. 1991. *Computer Simulation of Liquids*. Oxford: Clarendon Press. [14](#)
- Andersen, Hans C. 1980. Molecular dynamics simulations at constant pressure and/or temperature. *The Journal of Chemical Physics*, **72**(4), 2384. [24](#)
- Armstrong, C L, Trapp, M, Peters, J, Seydel, T, & Rheinstädter, M C. 2011. Short range ballistic motion in fluid lipid bilayers studied by quasi-elastic neutron scattering. *Soft Matter*, **7**(18), 8358–8362. [vi](#), [10](#)
- Arnold, Alexandre, Paris, Michaël, & Auger, Michèle. 2004. Anomalous Diffusion in a Gel-Fluid Lipid Environment: A Combined Solid-State NMR and Obstructed Random-Walk Perspective. *Biophysical Journal*, **87**(4), 2456–2469. [vii](#), [15](#)

REFERENCES

- Arnold, K, Pratsch, L, & Gawrisch, K. 1983. Effect of poly(ethylene glycol) on phospholipid hydration and polarity of the external phase. *Biochimica et Biophysica Acta*, **728**(1), 121–128. [49](#)
- Ballenegger, V. 2014. Communication: On the origin of the surface term in the Ewald formula. *The Journal of Chemical Physics*, **140**(16), 161102. [24](#)
- Bée, M. 1988. *Quasielastic Neutron Scattering: Principles and Applications in Solid State Chemistry*. Biology and Materials Science. Bristol: Adam Hilger. [72](#)
- Berendsen, HJC, & Postma, JPM. 1984. Molecular dynamics with coupling to an external bath . *The Journal of Chemical Physics*. **ix**, [25](#)
- Berendsen, HJC, Grigera, J R, & Straatsma, T P. 1987. The missing term in effective pair potentials. *Journal of Physical Chemistry*, **91**(24), 6269–6271. [27](#)
- Berg, Jeremy M, Tymoczko, John L, & Stryer, Lubert. 2005. *Biochemistry*. Fifth polish edition edn. Warsaw: PWN SA. [v](#), [1](#), [3](#), [6](#), [7](#)
- Berger, O, Edholm, O, & Jähnig, F. 1997. Molecular dynamics simulations of a fluid bilayer of dipalmitoylphosphatidylcholine at full hydration, constant pressure, and constant temperature. *Biophysj*, **72**(5), 2002–2013. [31](#)
- Berne, B.J., & Pecora, R. 2000. *Dynamic Light Scattering*. Dover Publications. [72](#)
- Binder, H, Kohlstrunk, B, & Heerklotz, H H. 1999. Hydration and lyotropic melting of amphiphilic molecules: a thermodynamic study using humidity titration calorimetry. *Journal of colloid and interface science*, **220**(2), 235–249. [50](#)
- Blair, G W. 1943. A New Criterion for Expressing the Intensity of Firmness' of Soft Bodies. *Nature*, **152**, 412. [12](#)

REFERENCES

- Boon, Jean Pierre, & Yip, Sidney. 1991. *Molecular Hydrodynamics*. New York: Dover Publications. [14](#), [53](#), [59](#)
- Brigham, E O. 1974. *Fast Fourier Transform*. Prentice Hall. [60](#)
- Brockerhoff, H, & Hoyle, R J. 1963. On the structure of the depot fats of marine fish and mammals. *Archives of biochemistry and biophysics*, **102**(Sept.), 452–455. [5](#)
- Brockerhoff, H, Hoyle, R J, & Wolmark, N. 1966. Positional distribution of fatty acids in triglycerides of animal depot fats. *Biochimica et Biophysica Acta*, **116**(1), 67–72. [5](#)
- Bronstein, I, Israel, Y, Kepten, E, Mai, S, Shav-Tal, Y, Barkai, E, & Garini, Y. 2009. Transient anomalous diffusion of telomeres in the nucleus of mammalian cells. *Physical Review Letters*, **103**(1), 018102–018102. [7](#), [8](#)
- Busch, Sebastian, Smuda, Christoph, Pardo, Luis Carlos, & Unruh, Tobias. 2010. Molecular Mechanism of Long-Range Diffusion in Phospholipid Membranes Studied by Quasielastic Neutron Scattering. *Journal of the American Chemical Society*, **132**(10), 3232–3233. [11](#)
- Christie, W W. 1985. Rapid separation and quantification of lipid classes by high performance liquid chromatography and mass (light-scattering) detection. *The Journal of Lipid Research*, **26**(4), 507–512. [3](#)
- Christie, W W, & Moore, J H. 1970. A comparison of the structures of triglycerides from various pig tissues. *Biochimica et Biophysica Acta*, **210**(1), 46–56. [5](#)
- Colbeau, A, Nachbaur, J, & Vignais, P M. 1971. Enzymac characterization and lipid composition of rat liver subcellular membranes. *Biochimica et Biophysica Acta (BBA) - Biomembranes*, **249**(2), 462–492. [4](#)

REFERENCES

- Darden, Tom, York, Darrin, & Pedersen, Lee. 1993. Particle mesh Ewald: An NlogN method for Ewald sums in large systems. *The Journal of Chemical Physics*, **98**(12), 10089. [24](#)
- Deserno, Markus, & Holm, Christian. 1998. How to mesh up Ewald sums. I. A theoretical and numerical comparison of various particle mesh routines. *The Journal of Chemical Physics*, **109**(18), 7678. [24](#)
- Dix, James A, & Verkman, A S. 2008. Crowding Effects on Diffusion in Solutions and Cells. *Annual Review of Biophysics*, **37**(1), 247–263. [10](#)
- Einstein, Albert. 1905. Über die von der molekularkinetischen Theorie der Wärme geforderte Bewegung von in ruhenden Flüssigkeit suspendierten Teilchen. *Annalen der Physik*, **322**(8), 549–560. [7](#), [12](#)
- Elf, Johan J, Li, Gene-Wei GW, & Xie, X Sunney XS. 2007. Probing transcription factor dynamics at the single-molecule level in a living cell. *Science*, **316**(5828), 1191–1194. [9](#)
- Ewald, Paul P. 1921. Die Berechnung optischer und elektrostatischer Gitterpotentiale. *Annalen der Physik*, **369**(3), 253–287. [24](#)
- Falck, Emma, Róg, Tomasz, Karttunen, Mikko, & Vattulainen, Ilpo. 2008. Lateral Diffusion in Lipid Membranes through Collective Flows. *Journal of the American Chemical Society*, **130**(1), 44–45. [xviii](#), [15](#), [16](#), [84](#), [86](#)
- Fick, Adolf. 1855. Über Diffusion. *Annalen der Physik*, **170**(1), 59–86. [11](#)
- Fitter, J, & Lechner, RE. 1999. Interactions of Hydration Water and Biological Membranes Studied by Neutron Scattering - The Journal of Physical Chemistry B (ACS Publications). *The Journal of Physical . . .* [49](#), [50](#)

REFERENCES

- Flenner, Elijah, Das, Jhuma, Rheinstädter, Maikel, & Kosztin, Ioan. 2009. Subdiffusion and lateral diffusion coefficient of lipid atoms and molecules in phospholipid bilayers. *Physical Review E*, **79**(1), 011907. [vii](#), [16](#), [49](#)
- Frenkel, Daan, & Smit, Berend. 2002. *Understanding Molecular Simulations*. San Diego, London: Academic Press, A Division of Harcourt, Inc. [21](#), [22](#), [23](#)
- Freundlich, Herbert, & Kruger, Deodata. 1935. Anomalous diffusion in true solution. *Transactions of the Faraday Society*, **31**, 906. [12](#)
- Gawrisch, Klaus, Gaede, Holly C, Mihailescu, Mihaela, & White, Stephen H. 2007. Hydration of POPC bilayers studied by 1H-PFG-MAS-NOESY and neutron diffraction. *European Biophysics Journal*, **36**(4-5), 281–291. [49](#), [50](#), [52](#)
- Goose, Joseph E, & Sansom, Mark S P. 2013. Reduced Lateral Mobility of Lipids and Proteins in Crowded Membranes. *PLOS Computational Biology*, **9**(4), e1003033. [vii](#), [16](#)
- Gurr, M I, Prottey, C, & Hawthorne, J N. 1965. The phospholipids of liver-cell fractions: II. incorporation of [32p] orthophosphate in vivo in normal and regenerating rat liver. *Biochimica et Biophysica Acta (BBA)-Lipids and Lipid Metabolism*, **106**(2), 357–370. [4](#)
- Harris, Fredric J. 1978. On the use of windows for harmonic analysis with the discrete Fourier transform. *Proceedings of the IEEE*, **66**(1), 51–83. [61](#)
- Herzog, H O, & Kruger, D. 1929. Nitrocellulose diffusion experiments. *Journal of Physical Chemistry*, **33**(2), 179–189. [12](#)
- Hess, Berk, & van der Vegt, Nico F A. 2006. Hydration Thermodynamic Properties of Amino Acid Analogues: A Systematic Comparison of Biomolecular Force Fields and Water Models. *The Journal of Physical Chemistry B*, **110**(35), 17616–17626. [28](#)

REFERENCES

- Hess, Berk, Bekker, Henk, Berendsen, Herman JC, & Fraaije, Johannes GEM. 1997. LINCS: a linear constraint solver for molecular simulations. *Journal of Computational Chemistry*, **18**(12), 1463–1472. [30](#)
- Hess, Berk, Kutzner, Carsten, van der Spoel, David, & Lindahl, Erik. 2008. GROMACS 4: Algorithms for Highly Efficient, Load-Balanced, and Scalable Molecular Simulation. *Journal of Chemical Theory and Computation*, **4**(3), 435–447. [27](#), [30](#), [38](#)
- Hinsen, Konrad, Pellegrini, Eric, Stachura, Sławomir, & Kneller, Gerald R. 2012. nMol-dyn 3: Using task farming for a parallel spectroscopy-oriented analysis of molecular dynamics simulations. *Journal of Computational Chemistry*, **33**(25), 2043–2048. [30](#), [40](#)
- Hoover, William G. 1985. Canonical dynamics: Equilibrium phase-space distributions. *Phys.Rev.*, **A31**, 1695–1697. [viii](#), [24](#)
- Humphrey, W, Dalke, A, & Schulten, K. 1996. VMD: visual molecular dynamics. *Journal of Molecular Graphics*, **14**(1), 33–38. [27](#)
- Hyslop, Paul A, Morel, Benoit, & Sauerheber, Richard D. 1990. Organization and interaction of cholesterol and phosphatidylcholine in model bilayer membranes. *Biochemistry*, **29**(4), 1025–1038. [32](#)
- Jeon, Jae-Hyung, Monne, Hector, Javanainen, Matti, & Metzler, Ralf. 2012. Anomalous Diffusion of Phospholipids and Cholesterols in a Lipid Bilayer and its Origins. *Physical Review Letters*, **109**(18), 188103. [vii](#), [10](#), [16](#)
- Jorgensen, William L, & Tirado-Rives, Julian. 1988. The OPLS [optimized potentials for liquid simulations] potential functions for proteins, energy minimizations for crystals of cyclic peptides and crambin. *Journal of the American Chemical Society*, **110**(6), 1657–1666. [vii](#), [26](#)

- Jorgensen, William L, Maxwell, David S, & Tirado-Rives, Julian. 1996. Development and testing of the OPLS all-atom force field on conformational energetics and properties of organic liquids. *Journal of the American Chemical Society*, **118**(45), 11225–11236. [vii](#), [26](#)
- Kneller, G R, & Hinsin, K. 2001. Computing memory functions from molecular dynamics simulations. *The Journal of Chemical Physics*, **115**(24), 11097. [67](#)
- Kneller, G R, Keiner, Volker, Kneller, Meinhard, & Schiller, Mathias. 1995. nMOLDYN - a program package for a neutron scattering oriented analysis of molecular dynamics simulations. *Computer Physics Communications*, **91**, 191–214. [30](#), [40](#), [41](#), [55](#)
- Kneller, Gerald R. 2011. Generalized Kubo relations and conditions for anomalous diffusion: physical insights from a mathematical theorem. *The Journal of Chemical Physics*, **134**(22), 224106–224106. [vii](#), [xi](#), [xviii](#), [13](#), [14](#), [44](#), [53](#), [54](#)
- Kneller, Gerald R, Baczynski, Krzysztof, & Pasenkiewicz-Gierula, Marta. 2011. Communication: Consistent picture of lateral subdiffusion in lipid bilayers: Molecular dynamics simulation and exact results. *The Journal of Chemical Physics*, **135**(14), 141105. [vii](#), [15](#), [43](#), [54](#), [58](#)
- Köchy, Thomas, & Bayerl, Thomas M. 1993. Lateral diffusion coefficients of phospholipids in spherical bilayers on a solid support measured by ^2H -nuclear-magnetic-resonance relaxation. *Physical Review E*, **47**(3), 2109. [44](#), [45](#)
- Kony, D, Damm, W, Stoll, S, & Van Gunsteren, W F. 2002. An improved OPLS-AA force field for carbohydrates. *Journal of Computational Chemistry*, **23**(15), 1416–1429. [26](#)
- Kučerka, Norbert, Nieh, Mu-Ping, & Katsaras, John. 2011. Fluid phase lipid areas and bilayer thicknesses of commonly used phosphatidylcholines as a function of temperature. *Biochimica et Biophysica Acta*, **1808**(11), 2761–2771. [36](#)

REFERENCES

- Lewis, Ruthven N A H, Sykes, Brian D, & McElhaney, Ronald N. 1988. Thermotropic Phase Behavior of Model Membranes Composed. *Biochemistry*, **27**(July), 880–887. [30](#), [44](#)
- Lindblom, Göran, Johansson, Lennart BA, & Arvidson, Gosta. 1981. Effect of cholesterol in membranes. Pulsed nuclear magnetic resonance measurements of lipid lateral diffusion. *Biochemistry*, **20**(8), 2204–2207. [44](#)
- Litman, B J, Lewis, E N, & Levin, I W. 1991. Packing characteristics of highly unsaturated bilayer lipids: Raman spectroscopic studies of multilamellar phosphatidylcholine dispersions. *Biochemistry*, **30**(2), 313–319. [30](#), [44](#)
- Loeffler, H H, & Winn, M D. 2009. Large Biomolecular Simulation on HPC Platforms 1. *Science and Technology Facilities Council, Technical Report*, Sept., 1–15. [29](#)
- Long, F A, Bagley, E, & Wilkens, J. 1953. Anomalous Diffusion of Acetone into Cellulose Acetate. *The Journal of Chemical Physics*, **21**(8), 1412. [12](#)
- Lovesey, S. 1984. *Theory of Neutron Scattering from Condensed Matter*. Vol. I. Oxford: Clarendon Press. [72](#)
- Mark, Pekka, & Nilsson, Lennart. 2001. Structure and Dynamics of the TIP3P, SPC, and SPC/E Water Models at 298 K. *The journal of physical chemistry. A*, **105**(43), 9954–9960. [49](#)
- Marrink, Siewert J, de Vries, Alex H, & Mark, Alan E. 2004. Coarse Grained Model for Semiquantitative Lipid Simulations. *The Journal of Physical Chemistry B*, **108**(2), 750–760. [vii](#), [26](#), [28](#), [36](#), [48](#)
- Marrink, Siewert J, Risselada, H Jelger, Yefimov, Serge, Tieleman, D Peter, & de Vries, Alex H. 2007. The MARTINI Force Field: Coarse Grained Model for Biomolecular

- Simulations. *The Journal of Physical Chemistry B*, **111**(27), 7812–7824. [vii](#), [26](#), [28](#), [36](#), [48](#), [53](#)
- McCammon, J A, Gelin, B R, & Karplus, M. 1977. Dynamics of folded proteins. *Nature*, **267**(5612), 585–590. [18](#)
- McDonald, Nora A, & Jorgensen, William L. 1998. Development of an All-Atom Force Field for Heterocycles. Properties of Liquid Pyrrole, Furan, Diazoles, and Oxazoles. *The Journal of Physical Chemistry B*, **102**(41), 8049–8059. [26](#)
- McQuarrie, Donald A. 2000. *Statistical Mechanics*. Mill Valey, California: University Science Books. [40](#)
- Metzler, Ralf, & Klafter, Joseph. 2000. Subdiffusive transport close to thermal equilibrium: From the Langevin equation to fractional diffusion . *Physical Review E*, **61**(May), 1–4. [14](#)
- Mills, R. 1973. Self-diffusion in normal and heavy water in the range 1-45 C. *Journal of Physical Chemistry*, **77**(5), 685–688. [49](#), [52](#)
- Mombelli, Enrico, Morris, Roger, Taylor, William, & Fraternali, Franca. 2003. Hydrogen-Bonding Propensities of Sphingomyelin in Solution and in a Bilayer Assembly: A Molecular Dynamics Study. *Biophysj*, **84**(3), 1507–1517. [50](#)
- Montroll, Elliott W, & Scher, Harvey. 1973. Random walks on lattices. IV. Continuous-time walks and influence of absorbing boundaries. *Journal of Statistical Physics*, **9**(2), 101–135. [13](#)
- Montroll, Elliott W, & Weiss, George H. 1965. Random Walks on Lattices. II. *Journal of Mathematical Physics*, **6**(2), 167. [13](#)

REFERENCES

- Murzyn, Krzysztof, Róg, Tomasz, Jezierski, Grzegorz, Takaoka, Yuji, & Pasenkiewicz-Gierula, Marta. 2001. Effects of Phospholipid Unsaturation on the Membrane/Water Interface: A Molecular Simulation Study. *Biophysj*, **81**(1), 170–183. [27](#), [30](#)
- Nagle, J F. 1993. Area/lipid of bilayers from NMR. *Biophysj*, **64**(5), 6–6. [27](#)
- Nagle, J F, Zhang, R, Tristram-Nagle, S, Sun, W, Petrache, H I, & Suter, R M. 1996. X-ray structure determination of fully hydrated L alpha phase dipalmitoylphosphatidylcholine bilayers. *Biophysj*, **70**(3), 1419–1431. [27](#)
- Narten, A H. 1971. Liquid Water: Molecular Correlation Functions from X-Ray Diffraction. *The Journal of Chemical Physics*, **55**(5), 2263. [80](#)
- Niemelä, Perttu S, Miettinen, Markus S, Monticelli, Luca, Hammaren, Henrik, Bjelkmar, Pär, Murtola, Teemu, Lindahl, Erik, & Vattulainen, Ilpo. 2010. Membrane Proteins Diffuse as Dynamic Complexes with Lipids. *Journal of the American Chemical Society*, **132**(22), 7574–7575. [vii](#), [49](#)
- Nosé, Shuichi. 1984. A unified formulation of the constant temperature molecular dynamics methods. *The Journal of Chemical Physics*, **81**(1), 511. [viii](#), [24](#)
- Oldham, Keith B, & Spanier, Jerome. 2006. *The Fractional Calculus*. New York: Dover Publications. [14](#)
- Owen, Dylan M, Williamson, David, Rentero, Carles, & Gaus, Katharina. 2009. Quantitative Microscopy: Protein Dynamics and Membrane Organisation. *Traffic*, **10**(8), 962–971. [7](#)
- Papoulis, A. 1984. *Signal Analysis*. New York: McGraw Hill. [65](#), [66](#)
- Papoulis, A. 1991. *Probability, Random Variables, and Stochastic Processes*. 3rd edn. New York: McGraw Hill. [65](#), [66](#)

REFERENCES

- Parrinello, M. 1981. Polymorphic transitions in single crystals: A new molecular dynamics method. *Journal of Applied Physics*, **52**(12), 7182. [viii](#), [25](#)
- Pasenkiewicz-Gierula, M, Takaoka, Y, Miyagawa, H, Kitamura, K, & Kusumi, A. 1999. Charge pairing of headgroups in phosphatidylcholine membranes: A molecular dynamics simulation study. *Biophysj*, **76**(3), 1228–1240. [26](#)
- Pasenkiewicz-Gierula, Marta, Takaoka, Yuji, Miyagawa, Hiroo, Kitamura, Kunihiro, & Kusumi, Akihiro. 1997. Hydrogen bonding of water to phosphatidylcholine in the membrane as studied by a molecular dynamics simulation: location, geometry, and lipid-lipid bridging via hydrogen-bonded water. *The journal of physical chemistry. A*, **101**(20), 3677–3691. [50](#)
- Pearson, Robert H, & Pascher, Irmin. 1979. The molecular structure of lecithin dihydrate. *Nature*, **281**(Oct.), 499–501. [49](#), [50](#)
- Perrin, Jean. 1909. *Mouvement brownien et realite moleculaire*. 18 serie edn. Vol. 18. Paris: Annales de Chimie et de Physique. [xviii](#), [12](#)
- Rahman, A. 1963. Intermediate Scattering Function in Slow Neutron Scattering. *Physical Review Letters*, May, 1–3. [vii](#)
- Rahman, A. 1964. Correlations in the motion of atoms in liquid argon. *Physical Review*, **136**(2A), A405. [18](#)
- Rahman, A., & Stillinger, Frank H. Jr. 1971. Molecular dynamics study of liquid water. *The Journal of Chemical Physics*, **55**(Oct.), 3336–3359. [78](#)
- Risselada, H Jelger, & Marrink, Siewert J. 2008. The molecular face of lipid rafts in model membranes. *Proceedings of the National Academy of Sciences*, **105**(45), 17367–17372. [7](#)

- Ritchie, Ken, Shan, Xiao-Yuan, Kondo, Junko, Iwasawa, Kokoro, Fujiwara, Takahiro, & Kusumi, Akihiro. 2005. Detection of Non-Brownian Diffusion in the Cell Membrane in Single Molecule Tracking. *Biophysj*, **88**(3), 2266–2277. [15](#)
- Róg, Tomasz, Murzyn, Krzysztof, & Pasenkiewicz-Gierula, Marta. 2002. The dynamics of water at the phospholipid bilayer surface: a molecular dynamics simulation study. *Chemical Physics Letters*, **352**(5), 323–327. [26](#)
- Róg, Tomasz, Murzyn, Krzysztof, Gurbiel, Ryszard, Takaoka, Yuji, Kusumi, Akihiro, & Pasenkiewicz-Gierula, Marta. 2003. Effects of phospholipid unsaturation on the bilayer nonpolar region: a molecular simulation study. *The Journal of Lipid Research*, **45**(2), 326–336. [30](#)
- Róg, Tomasz, Murzyn, Krzysztof, Milhaud, Jeannine, Karttunen, Mikko, & Pasenkiewicz-Gierula, Marta. 2009. Water Isotope Effect on the Phosphatidylcholine Bilayer Properties: A Molecular Dynamics Simulation Study. *The Journal of Physical Chemistry B*, **113**(8), 2378–2387. [50](#)
- Schwille, P, Korlach, J, & Webb, W W. 1999a. Fluorescence correlation spectroscopy with single-molecule sensitivity on cell and model membranes. *Cytometry*, **36**(3), 176–182. [43](#), [44](#)
- Schwille, Petra, Haupts, Ulrich, Maiti, Sudipta, & Webb, Watt W. 1999b. Molecular Dynamics in Living Cells Observed by Fluorescence Correlation Spectroscopy with One- and Two-Photon Excitation. *Biophysj*, **77**(4), 2251–2265. [vi](#), [x](#), [7](#), [10](#)
- Sciortino, F, Gallo, P, Tartaglia, P, & Chen, S. 1996. Supercooled water and the kinetic glass transition. *Physical Review E*, **54**(6), 6331–6343. [78](#)
- Shinoda, Wataru, & Okazaki, Susumu. 2001. Molecular dynamics study of the dipalmitoyl phosphatidylcholine bilayer in the liquid crystal phase: An effect of the potential force fields on the membrane structure. *Journal of Molecular Liquids*, Apr., 95–103. [26](#)

- Shlesinger, Michael F. 1974. Asymptotic solutions of continuous-time random walks. *Journal of Statistical Physics*, **10**(5), 421–434. [13](#)
- Silva, Liana C, de Almeida, Rodrigo F M, Castro, Bruno M, Fedorov, Alexander, & Prieto, Manuel. 2007. Ceramide-Domain Formation and Collapse in Lipid Rafts: Membrane Reorganization by an Apoptotic Lipid. *Biophysj*, **92**(2), 502–516. [7](#)
- Smaby, J M JM, Momsen, M M MM, Brockman, H L HL, & Brown, R E RE. 1997. Phosphatidylcholine acyl unsaturation modulates the decrease in interfacial elasticity induced by cholesterol. *Biophysj*, **73**(3), 14–14. [32](#)
- Stachura, Slawomir, & Kneller, Gerald R. 2013. Anomalous lateral diffusion in lipid bilayers observed by molecular dynamics simulations with atomistic and coarse-grained force fields . *Molecular Simulation*, **40**(1–3), 245–250. [vii](#), [viii](#), [28](#), [29](#), [30](#), [55](#)
- Steinbauer, Bernhard, Mehnert, Thomas, & Beyer, Klaus. 2003. Hydration and Lateral Organization in Phospholipid Bilayers Containing Sphingomyelin: A 2H-NMR Study. *Biophysj*, **85**(2), 1013–1024. [50](#)
- Stillinger, Frank H. 1974. Improved simulation of liquid water by molecular dynamics. *The Journal of Chemical Physics*, **60**(4), 1545. [18](#)
- Takaoka, Yuji, Pasenkiewicz-Gierula, Marta, Miyagawa, Hiroh, Kitamura, Kunihiro, Tamura, Yoshiyasu, & Kusumi, Akihiro. 2000. Molecular Dynamics Generation of Nonarbitrary Membrane Models Reveals Lipid Orientational Correlations. *Biophysj*, **79**(6), 3118–3138. [26](#)
- Takeuchi, Hiroshi. 2012. Structural Features of Small Benzene Clusters (C(6)H(6))(n) (n =j 30) as Investigated with the All-Atom OPLS Potential. *The journal of physical chemistry. A*, Sept., -. [26](#)

REFERENCES

- Tristram-Nagle, S, Petrache, H I, & Nagle, J F. 1998. Structure and Interactions of Fully Hydrated Dioleoylphosphatidylcholine Bilayers. *Biophysj*, **75**(2), 9–9. [27](#)
- Van Hove, L. 1954. Correlations in space and time and Born approximation scattering in systems of interacting particles. *Physical Review*, **95**(1), 249. [vii](#), [72](#)
- Walker, G. 1931. On Periodicity in Series of Related Terms. *Proceedings of the Royal Society A: Mathematical, Physical and Engineering Sciences*, **131**(818), 518–532. [67](#)
- Watkins, Edward K, & Jorgensen, William L. 2001. Perfluoroalkanes: Conformational Analysis and Liquid-State Properties from ab Initio and Monte Carlo Calculations. *The journal of physical chemistry. A*, **105**(16), 4118–4125. [26](#)
- Weber, Stephanie C SC, Spakowitz, Andrew J AJ, & Theriot, Julie A JA. 2010. Bacterial chromosomal loci move subdiffusively through a viscoelastic cytoplasm. *Audio, Transactions of the IRE Professional Group on*, **104**(23), 238102–238102. [8](#)
- Weigel, A V, Simon, B, Tamkun, M M, & Krapf, D. 2011. Ergodic and nonergodic processes coexist in the plasma membrane as observed by single-molecule tracking. *Proceedings of the National Academy of Sciences*, **108**(16), 6438–6443. [11](#)
- Weiss, Matthias, hashimoto, Hitoshi, & Nilsson, Tommy. 2003. Anomalous Protein Diffusion in Living Cells as Seen by Fluorescence Correlation Spectroscopy. *Biophysj*, **84**(6), 4043–4052. [11](#)
- Wuthier, R E. 1966. Two-dimensional chromatography on silica gel-loaded paper for the microanalysis of polar lipids. *The Journal of Lipid Research*, **7**(4), 544–550. [4](#)
- Wyss, Walter. 1986. The fractional diffusion equation. *Journal of Mathematical Physics*, **27**(11), 2782. [14](#)
- Yule, G U. 1927. On a Method of Investigating Periodicities in Disturbed Series, with Special Reference to Wolfer’s Sunspot Numbers. *Philosophical Transactions of the Royal*

REFERENCES

Society A: Mathematical, Physical and Engineering Sciences, **226**(636-646), 267–298.

67